NASA CR-159908

LOCKHEED
MISSILES & SPACE COMPANY, INC. • SUNNYVALE, CALIFORNIA
A SUBSIDIARY OF LOCKHEED AIRCRAFT CORPORATION

LMSC/D562493

CORRELATION TRACKING STUDY FOR METER-CLASS SOLAR TELESCOPE ON SPACE SHUTTLE

R. C. Smithson
T. D. Tarbell

Lockheed Palo Alto Research Laboratory
3251 Hanover Street
Palo Alto, CA 94304

June 1977

Final Report for Contract NAS5-23529

Prepared for

Goddard Space Flight Center
Greenbelt, Maryland 20771

TECHNICAL REPORT STANDARD TITLE PAGE

1. Report No.	2. Government Accession No	3 Recipient's Catalog No.

4. Title and Subtitle	5 Report Date
CORRELATION TRACKING STUDY FOR METER-CLASS SOLAR TELESCOPE ON SPACE SHUTTLE	June 24, 1977
	6. Performing Organization Code

7. Author(s)	8. Performing Organization Report No
Robert C. Smithson, Theodore D. Tarbell	LMSC/D562493

9. Performing Organization Name and Address	10. Work Unit No.
Lockheed Palo Alto Research Laboratory 3251 Hanover Street Palo Alto, Ca. 94304	11. Contract or Grant No. NAS5-23529
	13. Type of Report and Period Covered Final Report
12. Sponsoring Agency Name and Address Dr. Werner Neupert Goddard Space Flight Center Greenbelt, Md. 20771	14. Sponsoring Agency Code

15. Supplementary Notes

16. Abstract

This report describes the results of a study of the theory and expected performance level of correlation trackers used to control the pointing of a solar telescope in space using white light granulation as a target. Three specific trackers were modeled and their performance levels predicted for telescopes of various apertures. The study was conducted by investigating the performance of the computer model trackers on computer enhanced granulation photographs. Parametric equations for predicting tracker performance are presented.

17. Key Words (Selected by Author(s))	18 Distribution Statement
Trackers, correlation trackers, sun, solar granulation, Spacelab Optical Telescope	

19. Security Classif. (of this report)	20. Security Classif. (of this page)	21. No. of Pages	22. Price*
Unclassified	Unclassified	92	

*For sale by the Clearinghouse for Federal Scientific and Technical Information, Springfield, Virginia 22151.

PREFACE

The objective of this study was to provide a theoretical basis for evaluating correlation trackers to be used with meter class solar telescopes on the space shuttle, and to provide a specific evaluation of the expected performance of two trackers - a tracker developed by the Bendix Corporation for Marshall Space Flight Center, and a representative tracker using CCD arrays.

The method used was to digitize several high quality granulation pictures from Sacramento Peak Observatory, and run computer simulations of the tracker studied using the granulation data. Performance of the trackers in tracking accuracy and in providing telescope focus information was evaluated. In addition to specific evaluation of the Marshall and CCD trackers, parametric equations were derived from which the performance of any tracker using the same algorithms can be estimated.

Our principal conclusions are that a modified version of the Marshall tracker is suitable for tracking solar granulation to the required accuracy, but not for providing focus information. The CCD tracker is suitable for both tasks. Finally, the correlation tracker must be supplemented by a limb tracker for most applications.

We recommend that development of a CCD tracker specifically designed for solar granulation tracking begin, and that development of the Marshall tracker continue. The correlation tracker will be an extremely useful addition to solar telescopes in space, and has utility in ground-based observations as well. We also recommend that further study be conducted in the time behavior of solar granulation, in order to better define the utility of correlation trackers used without an auxiliary limb tracker.

Table of Contents

LIST OF FIGURES

LIST OF FIGURES (Cont.)

LIST OF FIGURES (Cont.)

1. Introduction

The purpose of this study is two fold. First, to develope the general theory of correlation trackers used with solar granulation targets, and second to investigate the performance of two specific trackers. The two trackers investigated are a tracker developed by the Bendix Corporation for Marshall Space Flight Center, and a representative tracker using CCD image detectors. The study concerns trackers as used with meter class telescopes in space, specifically with apertures ranging from 65 cm to 125 cm. The aspects of tracker operation studied are short-term tracking accuracy when the granulation pattern can be considered as fixed, effects of changing granulation patterns on tracking accuracy, and methods of monitoring telescope focus quality by means of the correlation tracker.

The first phase of the study was spent in digitizing several excellent granulation pictures with the PDS microdensitometer at Lockheed. These pictures were taken at Sacramento Peak using the 75 cm vacuum telescope. Pictures taken by Lockheed and others were studied, although most of the data was taken from a picture supplied by Dr. Dunn of Sacramento Peak. The microdensitometer traces were smoothed to remove film grain noise. Enhanced data designed to simulate space telescope seeing was prepared by converting the traces to square waves, and then smearing the traces with the point spread function of telescopes of specific apertures. This data base was used for calculating the performance of trackers in the fixed granulation pattern case.

We had hoped to use a granulation movie supplied by Dr. Dunn to provide information on performance of the trackers with time-varying granulation patterns. However, seeing effects proved impossible to remove, so this direct approach was abandoned. Instead, a theoretical approach using stratoscope data was used, which we believe provides a valid model of tracker performance.

This study attempted no actual tracker design work other than investigation of various scan pattern geometrics and analysis algorithms. No hardware was considered other than as necessary to obtain image detector performance parameters.

Final conclusions include the following:

- o The Marshall tracker, preferably with some modifications to scan geometry and processing algorithms will provide good performance in short-term tracking.
- o CCD trackers will provide even better performance in short-term tracking.
- o Any tracker observing only a few granules will shift badly with respect to the limb as the granules move. The present Marshall tracker which observes only one granule is particularly bad in this regard.
- o The CCD tracker provides excellent focus monitoring potential. The Marshall tracker is marginal.
- o Since any correlation tracker observing a small part of the sun will follow solar rotation, a means of compensation must be provided if stability with respect to the limb is to be achieved. This requires a separate limb tracker.

Perhaps the most powerful use of correlation trackers will be to keep two separate instruments co-aligned, or to operate inside the control loop of a separate limb tracker to reduce the image displacements from thruster firings or man push-offs. As a sole tracker the correlation tracker is, in general, insufficient.

We have prepared parametric representations of tracker performance which allow the easy evaluation of the performance level of any tracker using the processing methods studied. These were prepared by modeling trackers with various parameters and allowing them to "track" our digitized granulation data. The Marshall tracker was evaluated in the same way. The model for this tracker is accurate, except that its 66 image elements are assumed to lie in a line instead of a circle. This was done for processing convenience. We show in section 2.5 that this has a negligable effect on tracker performance.

Several unanswered questions still exist about tracker performance in the time-varying granulation case. We do not know if motions of neighboring granules are correlated. Also, the exact appearance of granulation at high resolution is unknown, although the high frequency content of our enhanced data agrees well with results from speckle interferometry. These limitations and proposed future studies are discussed at length in the final chapter of this report.

2. Basic Principles and Design of Correlation Trackers

2.1. Preliminary Considerations

Before the performance characteristics of correlation trackers can be discussed, we must first define several basic terms and concepts. First, a "tracker" is a device which senses the position of a target object within the field of view of a telescope, and automatically adjusts the pointing of that telescope to keep the image of the target object stationary in the telescope image plane. A tracker cannot be used to bring an object initially outside the field of view of the telescope within the field of view, therefore it must be supplimented by a "target acquisition system" in order to bring the target within the field of view of the telescope. This may be accomplished by manually aiming the telescope at the desired target, by using an automatic acquisition system using a second tracker coupled to a wider field finder telescope, or by raster scanning the telescope across the sky until the target is located. Most real acquisition systems combine several of these methods - for example scanning the sky in a search pattern until a target appears in a finder telescope, locking on to the target with the finder or "coarse" tracker, then finally tracking the target with the main telescope once it has been brought within the field of view.

It should be obvious that, in order to completely automate this acquisition and track sequence, something must be known about the expected characteristics of the target, so that the tracker can identify and track the target. In general, the more that is known about the target, the simpler and more affective the trackers can be. If enough is known a-priori about the target that it can be differentiated from any other object at which the telescope is likely to point, then in principle target acquisition can be completely automatic. In the case of the sun, which we know to be very bright, we could simply build the acquisition system so that it locked on to any object which produced a photon flux greater than some threshold picked to eliminate all dimmer objects. Moreover, once the sun is aequired, we can take advantage of the fact that the sun is a nearly perfect bright disc against a dark background to construct a limb tracker which operates by simply keeping two points on the sharply defined edge of the sun stationary in the field of view.

PRECEDING PAGE BLANK NOT FILMED

In many cases, however, not enough is know about the target's appearance to allow such a simple system to work. Indeed, all that may be known about the target is that its appearance will not vary too rapidly with time after it first appears in the telescope field of view. This is the situation in which a correlation tracker is designed to work. In solar observations from space we are forced to use a correlation trackers when the field of view of the telescope is not large enough to allow constant viewing of the solar limb, which is, of course, the only solar feature with an appearance that can be accurately predicted in advance. The best that can be hoped for on a random patch of the solar disc is a sunspot of some arbitrary shape, but relatively stable with time. Most of the time, however, we must be content with tracking features found in a granulation pattern characteristic of the quiet sun. These patterns change relatively rapidly with time (Correlations drop by 1/e in about 6 minutes.), but are stable enough for most purposes. The only things we know a-priori about the pattern we must track are statistical in nature - we know the RMS intensity fluctuation of the granulation pattern, the average brightness of the solar disc, and the average spatial dimensions of the individual granules making up the pattern. These items are useful for selecting an image detector for use with the correlation tracker, but not for any specific information about the pattern to be tracked. The exact pattern to be tracked must be learned after the telescope is pointed at the target.

2.2 Operating Principles of Correlation Trackers.

A correlation tracker works by using the following steps --

- The tracker is steered onto the target by some independent means.
- An image of the properly positioned target is then stored by the tracker.
- Subsequent images of the target are compared to the stored image and the telescope pointed so that the live and stored images overlap as precisely as possible.
- If changes in the target appearance with time make it difficult to determine when the live and stored images are properly overlapped, a new reference image is stored and tracking continues.

The errors and limitations, as well as the strengths of correlation trackers are apparent from these operating principles. The principal advantage, of course, is that it is no longer necessary to know exactly what the target looks like when the tracker is designed, since the tracker has the capability of storing a reference image when it is actually pointed at the target. The corollary to this is that the tracker cannot store its reference image until it is properly pointed at the target, and thus is incapable of target acquisition although it will continue to track the target after initial acquisition has been accomplished by their means. It is possible, of course, to pre-load the image memory with a reference image for use in acquisition, but if enough is known about the target to permit this a correlation tracker is probably not required.

Tracking errors arise from several sourses.

- o Random noise in the tracker image sensor or signal processing electronics - including imput photon shot noise.
- o Systematic errors - a particular correlation algorithm may show two identical images as precisely overlapped when in fact they are misregistered.
- o Errors due to changes in target appearance with time - it is no longer possible to find a perfect overlap between the stored and live images.

It follows from the fact that the tracker contains several sourses of error that the live and stored images are not likely to be precisely registered when the update of the stored image occurs. Thus, the new reference image will have been stored at a slightly different position than the original one. As successive updates occur, the aimpoint of the tracker will drift. This drift will be random walk if the errors are caused by random detector noise or by isotropic changes in the target with time. The drift can, however, tend in a particular direction (for example toward a brighter area of the solar disc) if systematic errors are involved.

2.3. Basic Design of Correlation Trackers.

Major design considerations for correlation trackers are;

- o Selection of the image pattern to be stored to provide the best compromise between tracking accuracy and memory size.

- o Selection of the best criterion for when the two images (stored and live) are most precisely overlapped.
- o Selection of an image detector to match available light and target contrast.

It should be kept in mind that all of the above are dependent on target characteristics, which are usually known only in a statistical sense in these applications where correlation trackers are used. A final design consideration is the selection of the optimum interval between updates to minimize aimpoint shift. In most cases this can be accomplished automatically by updating whenever the correlation between the stored and live images drops below some predetermined value.

Keeping these general design problems in mind, let us examine in detail the problem of designing a correlation tracker for use with a meter class telescope in space. First we will list several characteristics of the solar granulation target with which we will have to work.

- o Low contrast - a few tens of percent difference in intensity is the most that can be expected between the brightest and darkest features. Granules are typically about 2 arc seconds in dimension.
- o A tracking accuracy of .01 to .1 of the typical dimension of granules is required.
- o Except for sunspots, there is generally a lack of long-lived, well defined features.
- o Changes in the target pattern with a time scale on the order of minutes can be expected.
- o There will be no change in aspect angle or image scale with time.

These conditions are actually quite easy to accomodate. The chief cause for poor performance of correlation trackers is rapid changes in aspect angle or image scale with time (characteristic of many terrestrial applications). These generate large systematic errors and the need for rapid updating of the reference image, resulting in rapid shift of the aimpoint. In the solar case, the only need for updating is due to changes in the granulation pattern with time, and this problem is much less severe, requiring an update only once or twice per minute for optimum performance. (The selection of the optimum update interval will be described in detail below.)

The high tracking accuracy required composed to typical granule dimensions suggests that for tracking times longer than a small fraction of the granulation pattern correlation time (6 minutes), unacceptable errors will possibly occur due to the motions of individual granules. For accurate tracking with respect to the solar limb the tracker image will have to include many independent granules so that their motions will average out to an acceptably low value.

The selection of an image detector will be influenced by the low contrast of the granule pattern, the brightness of the image, the spatial resolution required, and the bandpass of the servo loop with which the tracker is to operate. The selection of this detector is described in detail in the following section.

2.4 Image Detectors

The two types of image detectors treated intensively in this study are the image dissector and the solid state detector array.

The solid state detector array makes use of integrated circuit technology to place on a single wafer of silicon an array of independent detectors. These detector arrays are available in various patterns and sizes. The individual detectors are usually read out sequentially by one of two methods. The readout technique used classifies the array as a "CCD" (charge coupled device) or a "CID" (charge injected device).

A third type of solid state detectors in common use is the "silicon diode array" or simply "diode array". The diode array method of forming the detectors in the silicon wafer is different from the other two, as is the readout technique.

All three detector types have the same basic spectral response and sensitivity - that of pure silicon. Good quantum efficiency is obtained from 0.4 to 1.1 μm, peaking at about 80% at 0.8 μm. These characteristics can, however, be altered by appropriate "doping" of the silicon. It is not within the scope of this study to discuss the characteristics of such detectors in full generality. Most solid state detectors are capable of signal-to-noise ratios (S/N) of about 300:1 to 1000:1 if enough light is available. Most detector elements hold between 10^5 and 10^7 electrons, so

their signal-to-noise ratio is limited by input photon shot noise to about 1000:1 to 3000:1. Intrinsic readout noise of 1000 electrons is easy to obtain with most types, and noise as low as 10 electrons has been reported for some CCD devices. Thus, solid state arrays operated near saturation are generally capable of performance close to the theoretical limit imposed by photon counting statistics. A typical value for S/N would be about 1000:1. Typically, individual detector elements can be read out at a speed of at least 2×10^{6} elements per second, so that an array consisting of 1000 elements could be read out in 5×10^{-4} seconds or less, sufficient for a servo bandpass of about 300 HZ. There is no reason why the array cannot be read out at a slower rate if insufficient photons are available, but as will be shown in a moment, this should not be necessary.

The image dissector is a popular detector for use with trackers, largely because its scan pattern can be varied at will, giving it a measure of flexibility not available with other image detectors such as solid state detectors or television tubes. The penalty paid is a substantial decrease in sensitivity and signal-to-noise ratio as compared with other detectors. The detector used with Marshall Tracker is an ITT model F4012 with an S-20 photocathode. The maximum photocathode current density permitted with this tube is $10 \mu A/cm^{2}$. The approximate signal-to- noise ratio of this detector at its maximum current density varies from 84:1 (guaranteed) to 168:1 (theoretical maximum) at the element dwell time used by the Marshall Tracker of 1.5×10^{-4} seconds. If the Marshall tracker is used with a different dwell time than 1.5×10^{-4} seconds, the above quoted signal-to-noise ratios are multiplied by a factor of $\sqrt{+_{dwell}/1.5 \times 10^{-4}}$ where $+_{dwell}$ is the new dwell time. For the present tracker we will take a typical value of S/N to be 100:1.

Let us now consider the photon flux available for use by the correlation trackers, in order to determine if any limitations are imposed by input photon shot noise. The smallest image element that need be considered has a linear dimension equal to half the Rayliegh resolution limit for the telescope. The use of smaller elements than this would only degrade the performance of the tracker, since no new information would be obtained.

A telescope of aperture D has an angular resolution α of $1.22 \lambda / D$ where λ is the wavelength of the light observed. The area covered by a

similar resolution element of half this diameter in the image plane is $0.292\ \lambda^2\ f^2/D^2$ where f is the effective focal length of the telescope. Now if F is the total photon flux in photons/cm ^{2}/sec striking the telescope aperture, the flux in the image plane will be equal to $1.14 \times 10^4\ D^2\ F/\ f^2$ and the total number of photons/sec falling into the half resolution element is given by $3.34 \times 10^3\ \lambda^2\ F$. If we take $\lambda = 5 \times 10^{-5}$ cm and consider the photon flux in the wavelength region from .4 μm to .6 μm, then $F = 9.55 \times 10^{16}$ photons/cm ^{2}/sec., and the photon flux per half resolution element from this wavelength region alone is 7.97×10^{11} photons/sec. Even if we assume that only 1% of these are counted by the image detector due to telescope optics losses and low quantium efficiencies (10% would be conservative for image dissectors and 50% for solid state arrays), we still have about 8×10^9 detected photons per second, which would saturate a CCD having a capacity of 10^6 electrons in 1.25×10^{-4} seconds. For a f/D = 50 system the flux at the image plane is 4.35×10^{17} photons/cm ^{2}/sec which if only 1% are counted gives an image dissector photocathode current density of 70 mA/cm ^{2} or 7000 times the ratial maximum for the F4012 image dissector. An attmuation of at least this amount will be required to prevent damage to the detector.

From these figures we can see that for any reasonable sample rate we can assume that either the image dissector or the solid state array will be operated at its maximum signal-to-noise ratio. Photon flux provides no limitations if a reasonable white-light image is available. If a narrow band blocking filter is used in front of the detector, the image dissector should not be affected down to a bandpass of about 1/2Å. The solid state detector, however, may begin to lose S/N at a bandpass of between 10 and 200Å depending on the transmission wavelength and efficiency of the blocking filter.

2.5. Scan Patterns

In general, it is not possible to perform a correlation test on the entire image accessible to the detector, resolved to the full power of the telescope. The reason is that there is usually so much data to be processed in this case that the tracker bandwidth is severely restricted by the processing time required. Also, the memory required to store such a large

number of data points may be excessively expensive both in dollars and power consumption, although both these factors are becoming less important as large-scale integration technology continues to advance.

Given that all of the points in the image cannot be recorded and analyzed, it becomes necessary to select some subset of image elements which gives adequate information for the required tracker accuracy, while at the same time keeping the total number of recorded elements small enough to allow sufficiently rapid processing of the data. Since only a few of the total number of available image elements are selected, it becomes important to select those portions of the image which contain the most information about image position. If the exact nature of the image is known beforehand this task is easy. Since an image detector measures light intensity as a function of position in the focal plane and since the tracker infers a change in image position by noting changes in intensity at certain of those positions in the focal plane, it is clear that we wish to monitor those parts of the image where the intensity is changing most rapidly as a function of position ($\frac{\partial I}{\partial X}$ is large). Also, there may be certain types of image motion, such as rotation about a known point, which can be easily detected and measured without extensive calculations if a particular scan pattern is used.

Most tracker scan patterns developed in the past have been designed to track objects such as aircraft or targets on the ground. A characteristic of these kinds of targets is a rapid change in aspect angle and target size with time. Since these conditions require rapid updating of the stored images, pure correlation trackers tend to drift excessively. If, however, the target has sufficiently high contrast with respect to the background, a proper selection of scan patterns will allow tracking on the target edges over a wide range of aspect angles and ranges. A popular pattern for this kind of application is the "rosette", shown in figure 2-1. As used with a solar tracker this pattern could be used to track sunspots or pores. A rosette pattern could also be used to track the solar disc itself as a limb guider.

It is not so apparent, however, that any advantage is gained when the rosette is used with a true correlation tracker. In that case the tracker

TYPICAL TRACKER SCAN PATTERNS

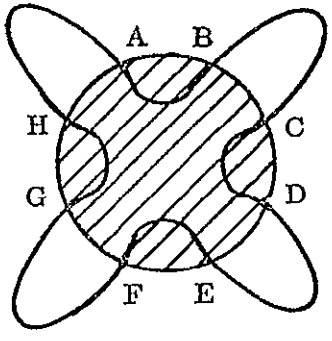

1

ROSETTE

TRACK TO KEEP AB = EF
AND CD = GH

THIS IS A WAY TO LIMB GUIDE WITH A CORRELATION TRACKER – WILL WORK WITH A WIDE RANGE OF TARGET DIAMETERS. IT IS USEFUL WHEN TRACKING SHARP-EDGED TARGETS AT VARYING RANGES AND MAGNIFICATIONS.

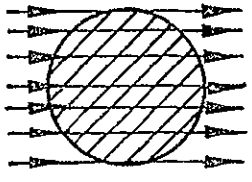

2

RASTER SCAN

STORES ENTIRE TARGET IMAGE AT THE RESOLUTION OF OPTICAL SYSTEM. A MAXIMUM POTENTIAL PRECISION AND ACQUISITION RANGE IS AVAILABLE, BUT BANDPASS MAY BE LOW DUE TO THE TIME REQUIRED TO PROCESS SOMUCH DATA.

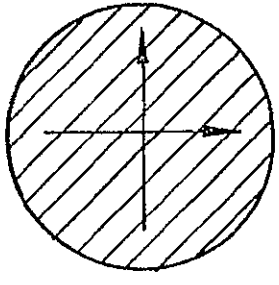

3

CROSS LINES

THE TECHNIQUE OF THE CCD TRACKER STUDIED, SACRIFICES ACQUISITION RANGE FOR SPEED AND SIMPLICITY.

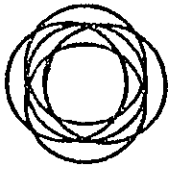

4

OFFSET CIRCLES

THE MARSHALL TRACKER TECHNIQUE – FAIRLY FAST AND SIMPLE – ALSO GIVES SOME IMMEDIATE FOCUS INFORMATION.

Figure 2-1

is positioned at random on the solar granulation pattern, and can no longer use the simplified edge tracking routine. The question now becomes whether a rosette is more likely to contain a large number of high $\frac{\partial I}{\partial X}$ elements than are equal number of elements in some other arrangement.

For correlation trackers used with time varying solar granulation patterns as targets, it is necessary to know the area over which the motions of the granules are correlated. A tracker which uses a scan pattern extending over only one such area will be subject to large errors due to local motions of the granules with respect to the solar limit. Strictly speaking, this is a problem of image scale rather than scan pattern, but a pattern which covers a large spatial extent for the number of elements (eg - widely scattered points) would tend to be more immune to this problem than a compact pattern (eg - a circle) containing the same number and size of elements.

For use with a target consisting of random solar granulation patterns the only important parameters are the number of image elements, the number of independent granules sampled, and to a lessor extent the size of the image elements in arc seconds. The shape of the scan pattern is important only insofar as it affects the number of individual granules sampled.

Consider a granulation pattern with intensity $I(X, Y)$, and further consider the value of $\frac{\partial I}{\partial X}$ at each point in that pattern. Assume that an image detector samples that pattern at N positions (x_i, y_i) $i = 1, 2, \ldots, N$. Let $\tilde{D}_v$ be the expectation value of $\left(\frac{\partial I}{\partial X}\right)^2$ over the entire image. Let $< D_p^2 >$ be the expectation value of $\frac{1}{N} \sum_{i=1}^{N} \left(\frac{\partial I}{\partial X}\Big|_{x_i}\right)^2$ if a scan pattern P is superimposed at random on the granulation image. The larger the value of $< D_p^2 >$, the better the scan pattern. Note, however that since $< D_p^2 >$ is the most probable value over many random superpositions and not a value determinable from a single superposition, that

$$< D_p^2 > = \frac{1}{N} \sum_{i=1}^{N} < \frac{\partial I}{\partial X}\Big|_{x_i} >^2 = \tilde{D}_x. \qquad (2\text{-}1)$$

Thus, regardless of the pattern of elements chosen, the probable effectiveness of that pattern in providing maximum sensitivity in converting image motions

to intensity variations is the same, regardless of the number of elements sampled or their geometric relationship. This result applies to any scene where the tracker scan pattern is placed at random on the scene without any attempt to locate it in a particularly advantageous spot.

The above result does not mean that the number of elements and scan patterns have no relationship to tracker performance. A tracker with a large number of elements will always be more precise than one with a smaller number. This is true simply because each element acts as an independent tracker. Since the light level at each element is measured only to the precision permitted by system noise, and since the position error signal from an N element tracker is the average of all N elements, the probable improvement in tracker signal-to-noise is a factor of $\sqrt{N}$.

The scan pattern also has a definite effect on tracker performance. The most probable accuracy in tracking on a particular stored piece of granulation image is independent of scan pattern, but the degree by which individual stored images give accuracies departing from the most probable depends on the "compactness" of the patterns. That is, if

$$A = \frac{1}{N} \sum_{i=1}^{N} \left(\frac{\partial I}{\partial X} \Big|_{xi} \right)^2 \qquad (2\text{-}2)$$

then

$$\sigma_A^2 = \langle A^2 \rangle - \langle A \rangle^2 \qquad (2\text{-}3)$$

is pattern dependent.

This result be seen intuitively by considering the extreme case where all N elements overlap, consisting of N independent evaluations of I at a particular point. Then if that point happened to fall on a part of the image where $\frac{\partial I}{\partial X} \approx 0$, the tracker would be very poor. If, on the other hand $\frac{\partial I}{\partial X}$ at that point happened to be large, the performance would be excellent. A wide variation in performance would be expected from stored image to stored image. On the other hand, if the N elements were widely separated compared to the image structure scale, the probability that the average value of $\left(\frac{\partial I}{\partial X} \right)^2$ for all the points would vary much from that for the image as a whole would be small. Reasonably consistent performance would be expected. The result is that a large σ_A^2 is expected for patterns small compared to the

image structure, and a small σ_A^2 for patterns large compared to image structure. This effect has been investigated empirically for solar granulation as a part of this study. The magnitude of the effect depends on the characteristics of the granulation pattern and the size of the image elements in arc seconds.

We must also consider the effects of different scan patterns as they relate to acquisition range - the distance by which the tracker can be displaced off target without losing its lock on the target. The largest acquisition range is available, of course, with a complete raster scan. In this case, the lock can, in principle, be re-established after a displacement anywhere within the field of view of the tracker. Crossed lines have a relatively long acquisition range in the directions along the two lines, provided that the motion does not scan along both lines simultaneously. Displacement of more than the order of a granule diameter from both lines simultaneously will result in a loss of lock. This is because no information is recorded concerning the character of the image off the two scan lines. The offset circle pattern has the smallest potential acquisition range of the trackers considered in this study - equal to about one granule diameter in any direction.

None of the proposed trackers have the ability to sense image rotation as such. This is not required since the rotational pointing accuracy of the IPS is currently specified as ± 10 $\pi$to 3σ accuracy. This gives a maximum linear displacement of .1 π if the roll is about one limb of the sun while the correlation tracker is monitoring the opposite limb 1920 π away. In this case the motion in the field of view of the tracker would appear as primarily displacement and could be corrected as such. The differential displacement due to rotation across the $\overset{\frown}{60''}$ field of view of the tracker would be a maximum of .006 π and thus is negligable.

Finally, a few remarks concerning tracker versatility are in order. The above consideration concerning scan patterns apply only when the pattern is selected before hand and placed on the image at random. The image dissector used in the Marshall tracker has the advantage that the size, shape and position of the scan pattern can be easily varied. An operator monitoring a television with a representation of the pattern superimposed on the television picture could manually alter the pattern size, position,

and shape to track a particular feature. This capability is not present in the current Marshall tracker, but could be easily implemented.

In summary, the relevant parameters in scan pattern selection are element size, number, and degree of compactness of the pattern. The geometric shape of the pattern is relevant only as it affects the compactness. We have modeled all trackers with linear arrangements of elements and considered only the compactness effects of the circular scan pattern of the Marshall tracker. The detailed effects of this approximation, as well as effects of changing image scale, number of elements, and element size is discussed in detail in chapter 3.

2.6. Analysis Algorithms

Once an appropriate scan pattern has been selected, and a reference image recorded, a method must be developed which compares the stored and live images and derives from them the required information - how far and in what direction the telescope pointing has drifted since the reference image was stored. The selection of the proper algorithm to provide the pointing information given the raw image data is potentially the most complex design problem of all. In practice, however, a few algorithms are commonly used, and give satisfactory results.

In addition to the basic algorithm for deriving the pointing information from the image data, it is possible to pre-process the image before providing it to the pointing algorithm - for example by Fourier transforming it, filtering to provide only high spatial frequency data, and re-transforming to image space. Potentially the number of pre-processing schemes is infinite, but again, only a few are in common use. Except for smoothing to remove grain noise and enhancement routines to simulate space telescope performance, we have done no pre-processing in this study. In our model of the Marshall tracker, however, we did separate our data into 8 discrete levels in the same way as the actual tracker, which does constitute pre-processing of the image.

The pointing algorithm used by the Marshall tracker is one of the most common. It consists of forming the correlation function

$$C(\delta) = \sum_{i=1}^{N} I_s (X_i + \delta, y_i)\, I_1 (x_i, y_,) \qquad (2\text{-}4)$$

where the summation is over the N elements of the detector, I_s represents the stored image, and I_l the live image. In the absence of image motion, $C(\delta)$ will be a maximum when $\delta = 0$, provided I_s and I_l are substantially the same - that is - provided the granulation pattern has not changed very much since the time I_s was stored. If the telescope aimpoint changes between the time I_s was stored and the time the correlation is made with the live image I_l, then the maximum value of $C(\delta)$ will occur at some value of $\delta \neq 0$. The sign and magnitude of δ for which $C(\delta)$ is largest determines the direction and magnitude of the image shift.

Unfortunately, this simple correlation function is subject to a number of systematic errors. The maximum of $C(\delta)$ may occur at a position where I_s and I_l are not exactly overlapped, even if I_s and I_l are identical. To see how this can occur, consider the 1-dimensional integral representation of the correlation function:

$$C(\delta) = \int_{-2a}^{2a} I(x)\, I(x + \delta)\, dx \qquad (2\text{-}5)$$

Figure 2-2 shows the results of using this function on various distributions $I_l = I_x = I$. In case I the maximum of $C(\delta)$ occurs at $S = 0$. In case II, a net slope in the intensity function extending beyond the sampled area gives a maximum at $\delta = a$. A tracker using this algorithm would believe that I_s and I_l were in registration at $\delta = a$, when in fact they are not. Case III shows a typical granulation trace and the resultant correlation peak. If there is a net slope from left to right the peak will be slightly offset from $\delta = 0$ as shown. These systematic errors depend on the nature of the granulation pattern, and are discussed at length in chapter 3.

An algorithm which exhibits no systematic errors of this type is the mean square residual function:

$$C(\delta) = \sum_{i=1}^{N} [I_s(x_i + \delta, y_i) - I_l(x_i, y_i)]^2 \qquad (2\text{-}6)$$

we have evaluated the performance of the Marshall tracker and the CCD tracker using this algorithm.

Given that some method is used to generate as correlation peak of the type shown in figure 2-2, some means of identifying the peak is necessary.

SYSTEMATIC ERRORS IN THE BASIC CORRELATION FUNCTION

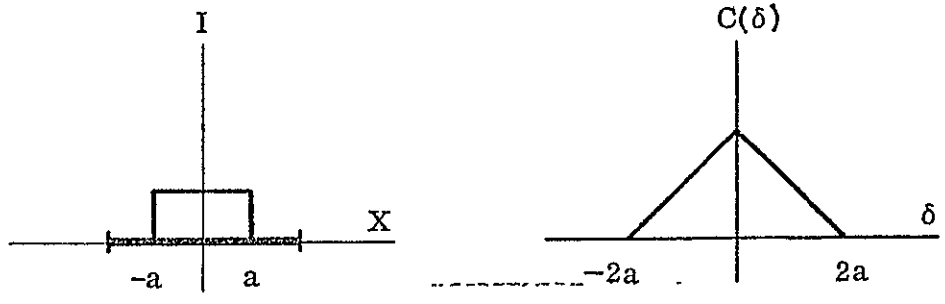

I

$$C(\delta) \propto \int_{-2a}^{2a} I(x)\, I(x+\delta)\, dx$$

IN CASE I, A SINGLE FEATURE ENTIRELY WITHIN THE SAMPLE AREA GIVES AN AUTOCORRELATION PEAK AT $\delta = 0$ AS IT SHOULD.

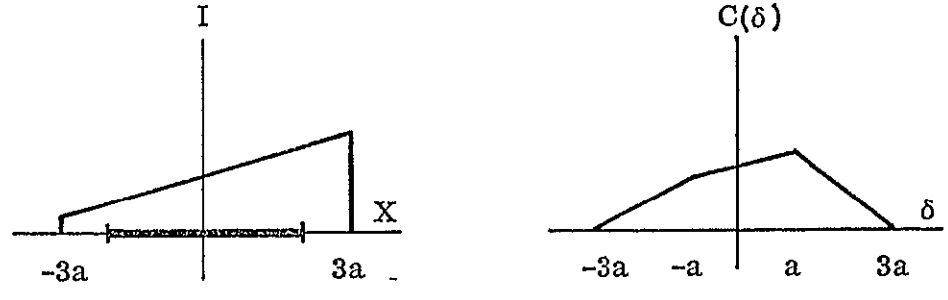

II

IN CASE II, A FUNCTION WITH A SLOPE EXTENDING OUTSIDE THE SAMPLE AREA GIVES AN AUTOCORRLEATION PEAK AT $\delta = a$, NOT THE REGISTERED POSITION.

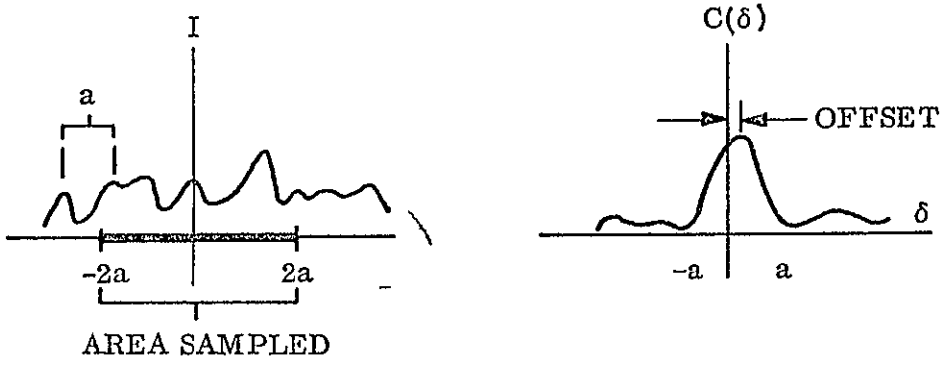

III

IN CASE III, A TYPICAL SOLAR GRANULATION TRACE GIVES AN AUTOCORRELATION PEAK AT A SLIGHTLY OFFSET POSITION. THE LARGER THE AREA SAMPLED, THE SMALLER THE ERROR.

Figure 2-2

The simplest is to simply find the value of δ where $C(\delta)$ is largest. The disadvantage of this approach is that in a flat peak, system noise may cause large position measurement errors. Another method is to locate two points on either side of the peak where $C(\delta)$ is the same, and assume the peak to be half-way in between. This technique is less noise sensitive, since the slope of the peak is greater on the sides, and an error in the value of $C(\delta)$ causes a smaller error in δ itself, but the method is subject to errors caused by asymmetrical peaks. These techniques are illustrated in Figure 2-3. The Marshall tracker uses the 2nd method. We have analyzed the performance of both trackers using both techniques.

2.7. Effects of the Tracker Servo Loop

In this study we have concentrated on the expected accuracy of the correlation tracker itself, without reference to the servo loop with which it is operated. It is necessary, however, to briefly consider the performance of the trackers as components of servo systems.

The sources of error in a correlation tracker fall into three classes - random noise, systematic errors as discussed in section 2.6, and errors due to changes in the granulation pattern with time. The first of these, random noise, is influenced by the bandwidth of the servo loop with which the tracker is operated.

Consider the Marshall tracker as an example. It makes one correlation measurement in about .01 seconds, with a certain random noise component due to amplifier noise, input photon shot noise, and other random noise sources. If it is used with a servo with a bandpass of 10HZ, it has the opportunity to make several independent measurements in the servo response time. Thus, the error contribution from this noise component will be somewhat reduced by an averaging process.

The general rule is that the random noise error will be reduced by an amount $\sqrt{\frac{2f_s}{f_r}}$ where f_s is the servo 3db bandwidth and f_r is the sampling rate in Hertz.

The maximum bandwidth for which sampling servo system will easily operate is $f_v/2\pi$, so under these conditions we expect the random noise contribution to be reduced by a factor of $\sqrt{\frac{2}{2\pi}}$ or 0.56. The present configuration of

PEAK LOCATION

I

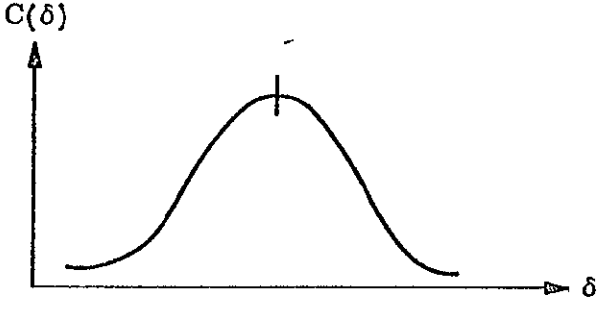

PEAK VALUE – SIMPLY LOCATE THE VALUE OF δ WHERE $C(\delta)$ IS MAXIMUM. NOISE-SENSITIVE ON A FLAT PEAK.

II

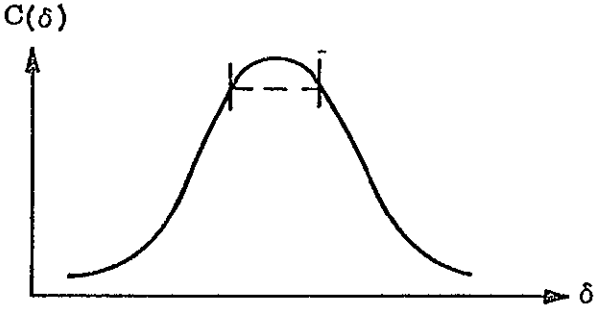

TWO-POINT BALANCE – LOCATE TWO POINTS ON OPPOSITE SIDES OF THE PEAK SUCH THAT $C(\delta)$ IS THE SAME FOR BOTH. THE PEAK IS ASSUMED TO BE HALF WAY BETWEEN. SUSCEPTIBLE TO PEAK ASYMMETRY.

Figure 2-3

the Marshall tracker has a servo bandpass of 10 HZ, so a reduction in random noise by a factor of 0.45 would be expected.

Unfortunately, this noise component is not usually dominant, but servo bandpass must be considered for precise calculations. The relationship of this noise source to others is discussed exhaustively in chapter 3. The results given for the random noise and total tracking errors contain no allowance for tracker bandwidth. This allowance must be made as provided above when the bandwidth is known. If an optimum servo system is assumed the random noise figures should be reduced by a factor of 0.56 from those given in this study.

2.8. Focus Information

The two techniques of deriving focus information from a correlation tracker are shown in figure 2-4. The first is simply to measure the sharpness of the correlation peak by taking the values of $C(\delta)$ at the center of the peak and at two points displaced an equal and fixed distance on either side. The difference between the peak value and the average of the two side values gives a measure of the peak sharpness and thus the quality of the focus. The greater the difference the sharper the peak and the better the focus. This method is easily implemented from data available from the Marshall tracker. Unfortunately it is too inaccurate to use. Also, the best possible sharpness of the peak is scene dependent, thus this method gives only a realtive measure of focus, not an absolute one.

The second method is to take the Fourier power transform of a line of video from the tracker and measure the power at high spatial frequencies. The more high frequency power the better the focus. This method is also scene dependent, but it is much more sensitive. Used with the Marshall tracker it is marginal, but with the CCD tracker it gives excellent results. It requires, of course that the tracker scan a continuous line of elements to provide the proper signal for processing. Isolated elements cannot be used in this application.

Results and theory of focus information derivation are discussed in detail in chapter 4.

FOCUS INFORMATION

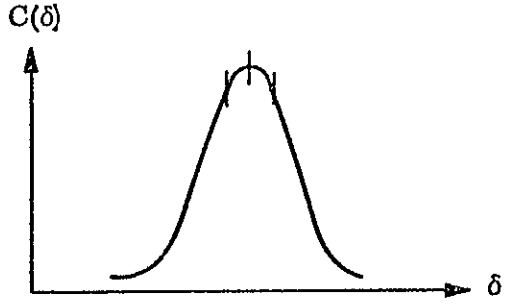

CORRELATION PEAK SHARPNESS –
AVAILABLE FROM PRESENT MARSHALL TRACKER

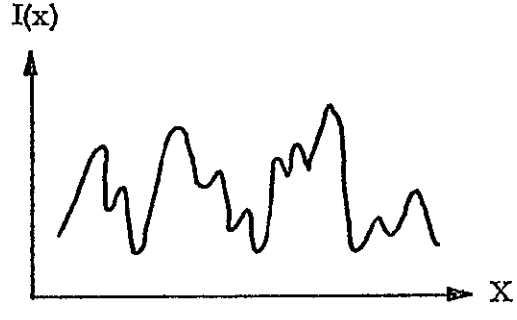

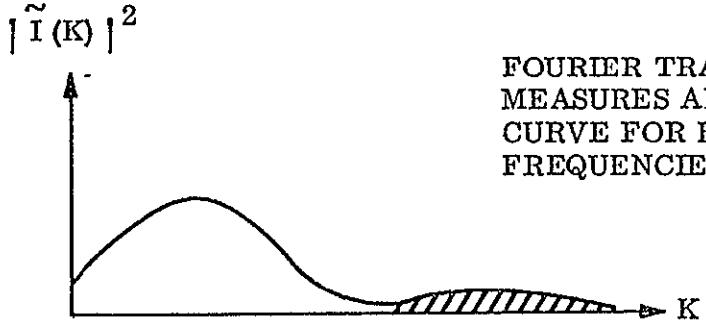

FOURIER TRANSFORM –
MEASURES AREA UNDER
CURVE FOR HIGH SPATIAL
FREQUENCIES

Figure 2-4

2.9. The Marshall Tracker

Figure 2-5 shows the operating principles of the Marshall tracker. This tracker uses an ITT /4012 image dissector with a .001" diameter aperture and an S-20 photocathode. The scan pattern is a circle containing 66 elements which are digitized into either 8 or 2 levels for analysis by a digital processor. It's simple rate is 98.485 HZ and its servo bandwidth is 10 HZ, although there is no fundamental reason why the sample rate and servo bandwidth cannot be increased by at least an order of magnitude if required. It's present demonstrated tracking rate is 7 $\overset{\frown}{''}$ per second, and this could easily be increased to 100 $\overset{\frown}{''}$ per second with very little trouble. There are plenty of photons to do this (see section 2.4).

The major drawback of the image dissector is a limited signal-to-noise ratio. The major strength is its flexibility in providing easily changed scan patterns. The present design does not take advantage of this flexibility but as we have seen in section 2.5, so long as it is used as a randomly positioned tracker this is unimportant. This type of detector would, however, lend itself to a manually adjustable sunspot tracker.

The most important result of the limited signal-to-noise ratio of the image dissector is relatively poor performance as a focus monitor. The most serious drawback of the present tracker design is the size of the areas scanned - a circle 1 $\overset{\frown}{''}$ in diameter. This makes the tracker extremely susceptible to motions of individual granule. By simply changing the image scale so that the tracker covers a larger area this can be remedied, and tracking performance much improved. Performance can also be improved by using the least squares residuals algorithm instead of a simple correlation function.

2.10. The CCD Tracker

The typical CCD tracker we chose to study was a tracker using a pair of crossed linear detector element arrays each containing 512 diodes. Arrays such as this are available from every major manufacturer of these devices. We assumed that each detector element had a S/N ratio of 1000:1, and that it was digitized with 10 bit accuracy (1024 levels). The tracker was assumed to operate by storing a single scan of the two lines in a 1024 X 10 bit memory to serve as the reference image. The equivalent of the Marshal tracker

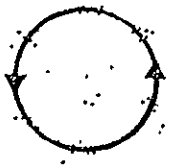

1. STORES 66 ELEMENTS AROUND A CIRCLE
   $I_c(i)$ $i = 1, 66$

2. STEPS IMAGE DISSECTOR SCAN UP AND STORES ANOTHER 66 ELEMENTS
   $I_u(i)$ $i = 1, 66$

3. STEPS DOWN, LEFT AND RIGHT, AND STORES 66 ELEMENTS FOR EACH POSITION OF THE CIRCLE – 5 POSITIONS IN ALL:
   $I_c, I_u, I_d, I_\ell, I_r$

4. MOVES IMAGE DISSECTOR SCAN BACK TO CENTER AND CONTINUES TO READ INTENSITY AT ALL 66 ELEMENTS AROUND THE CIRCLE
   $I(t, i)$

5. $$C_u(t) = \sum_{i=1}^{66} I_u(i)\, I(t, i)$$
   $$C_d(t) = \sum_{i=1}^{66} I_d(i)\, I(t, i)$$
   $$\Delta y(t) = K(C_u(t) - C_d(t))$$
   SIMILARY FOR $\Delta x(t)$

6. QUANTIZES INTENSITIES INTO EITHER 8 OR 2 LEVELS. UPDATES WHEN $C_c(t) \leq 0.8$

Figure 2-5

$C_u(\tau)$ would be formed by

$$C_u(t) = \sum_{i=1}^{511} I_s(i)\, I_1(t, i+1) \qquad (2\text{-}7)$$

where I_s is the stored image and I_1 the live image at time t. i denotes the i'th diode in the vertical line counting from the bottom. We have examined this tracker using both the least squares residuals and simple correlation function algorithms, and have examined both the peak value and two point balance methods of peak location. We have also tested the performance of the tracker when the number and size of the image elements are varied.

The tracker gives excellent results both as a tracker and for focus information. The chief drawback is the CCD's rigid scan geometry. It is not well suited for manual pattern control. In general, the performance level is much better than the Marshall tracker, largely due to the greater number of elements and better signal-to-noise ratio.

We have made no attempt in this study to produce a physical design of this tracker, although this could easily be done with some additional effort.

3. Detailed Tracker Simulation

3.1. Introduction

An extensive set of computer simulations of tracker performance has been done to evaluate the noise, systematic, and time-dependent errors of three different tracker concepts. In so far as possible, the goal has been to perform the same operations on digitized granulation scenes as the tracker would in real time. The major problem is the lack of relevant observations on the temporal behaviour of small-scale features in the solar granulation (as distinct from correlations or large-scale average behaviour). Even so, tracker performance on fixed scenes has been studied in great detail, and a physically plausible model for the growth of tracker errors in time has been developed. In this way, upper and lower limits to tracker errors have been evaluated as functions of tracker design, and the ranges implied by these limits indicate the uncertainties present.

For computer simulation, a tracker is defined by the following properties:

- Tracking Algorithm: the method of inferring image displacement from the real-time measured intensities; three were studied, corresponding to the Marshall Tracker (MT), a modified Marshall Tracker (MMT), and the least-squares algorithm of a CCD Tracker;
- SN: signal-to-noise ratio of the detector and associated electronics, before any quantization;
- N_{el}: number of detector elements;
- d: detector element size in arcseconds, which is used as a scale factor in image space; that is, when d is varied, the geometric arrangement of detector elements in the focal plane is constant, but the effective focal length and thus the image size changes;
- τ_u: average update time, the time interval between scene storages in memory.

Note that the geometric pattern of detector elements is not varied: linear arrays were always used for their great computational advantages. As discussed above, tracker geometry has little effect on the errors calculated here. The transfer function of the tracker servo-mechanism has also not been specified, although it will affect the noise errors (see Section 2.7). This was done because: (a) intelligent servo design requires detailed knowledge of the spectrum of image displacements which the tracker is to suppress;

(b) comparison of different trackers on their own merits as error sensors was possible.

The first step in analyzing a Tracker was to measure its noise and systematic errors when tracking on a fixed (time-independent) scene. Since the solar granulation is a random process, errors were computed for each of 100 independent scenes (Section 3.2) and ensemble averages were found. Several data sets with varying degrees of image enhancement were used to study the effects of telescope resolution and seeing conditions. For each scene, tracker detector outputs were computed as a function of image displacement; then the tracker algorithm allowed calculation of noise error (standard deviation) and systematic error (constant for a given scene). Repetition of these steps provided the two figures of merit for fixed scene tracking: mean noise error σ_n and root-mean-square systematic error σ_s. If the correlation tracker is intended to keep two different instruments (spectrographs, for example) aimed at the same point in identical scenes, then σ_n and σ_s are the only relevant errors.

More generally, though, the accumulation of tracking error in time is desired. The model presented in section 3.3 permits evaluation of errors as functions of time or update time, given the algorithm, σ_n, σ_s and some additional information on the tracker field-of-view. If the tracker is used to follow a long-lived feature (a dark pore or bright granule, for example), then only noise and systematic errors must be considered. However, for tracking in absolute coordinates with respect to the solar limb, then the more difficult problem of drift due to transverse motion of granules in the tracker FOV must be attacked. A reasonable model, providing upper and lower limits to this drift rate, is presented.

Specific results for three prototype trackers are presented in Sections 3.4 - 3.6. In each case, the errors of any tracker using the same algorithm can easily be calculated from the formulae and graphs provided. Section 3.7 gives a fully-worked example of such calculations, and the last section contains a brief summary of correlation tracker performance.

3.2 Data for Tracker Simulation

The one-dimensional scenes used in deriving tracker errors were digitized from a white light granulation picture, taken in excellent seeing at the 30

inch (76 cm) vacuum telescope at Sacramento Peak Observatory by Dr. R. B. Dunn. Several other granulation pictures were digitized and gave results similar to the SPO frame, but they were rejected for extensive calculations because of poorer resolution. One hundred lines were digitized, separated by intervals of 1.5 ", using a 0.091 " square slit on the Lockheed PDS 1010G Microdensitometer. Each line consisted of 10,000 points at 0.0076 " intervals. After mild smoothing to reduce grain noise, optical densities were converted to arbitrary intensity units using $\gamma = 4$ (results are insensitive to the precise value).

Figure 3-1 shows a sample scene. The auto-correlation functions derived from this scene by the model Marshall Tracker (MT) and CCD Tracker are shown in Figure 3-2. The CCD Tracker's FOV lies between the dotted lines on Figure 3-1, whereas the MT is one-third as long; these trackers are discussed in more detail in Sections 3.4 and 3.6. Mean-squared residual functions for the same trackers and data are shown in Figure 3-3.

The excellent spatial resolution of these observations is shown by the fact that the correlation peaks in Figure 3-2 are 20% narrower than those published in Reference 1, obtained with the Stratoscope balloon-born telescope. Since tracker performance virtually always improves when fine details (high spatial frequencies) are added to the scene, it is important to estimate how much detail has been lost because of finite telescope resolution and atmospheric seeing. Although the SPO data is nearly diffraction limited (Rayleigh limit = 0.17 "), some degradation from seeing is present, and so Tracker errors derived from ground-based data are worst cases for the performance with a 65 cm or 125 cm aperture space telescope.

To provide lower limits to the expected errors, the ground-based data was "enhanced" by quantizing it to a two-level square wave, representing bright granules and dark lanes with perfectly sharp edges. This was merely a convenient way of generating random scenes with approximately the correct amount of high frequency detail. Figure 3-4 shows the spatial power spectrum of this enhanced data along with the recent measurements by speckle interferometry of the same one-dimensional power spectrum by Kinahan (Ref. 2; consistent results also in Ref. 3). After quantizing, the scenes were folded with the point-spread function of a 65 cm or 125 cm telescope before use in tracker simulations; the following one-dimensional PSF was used:

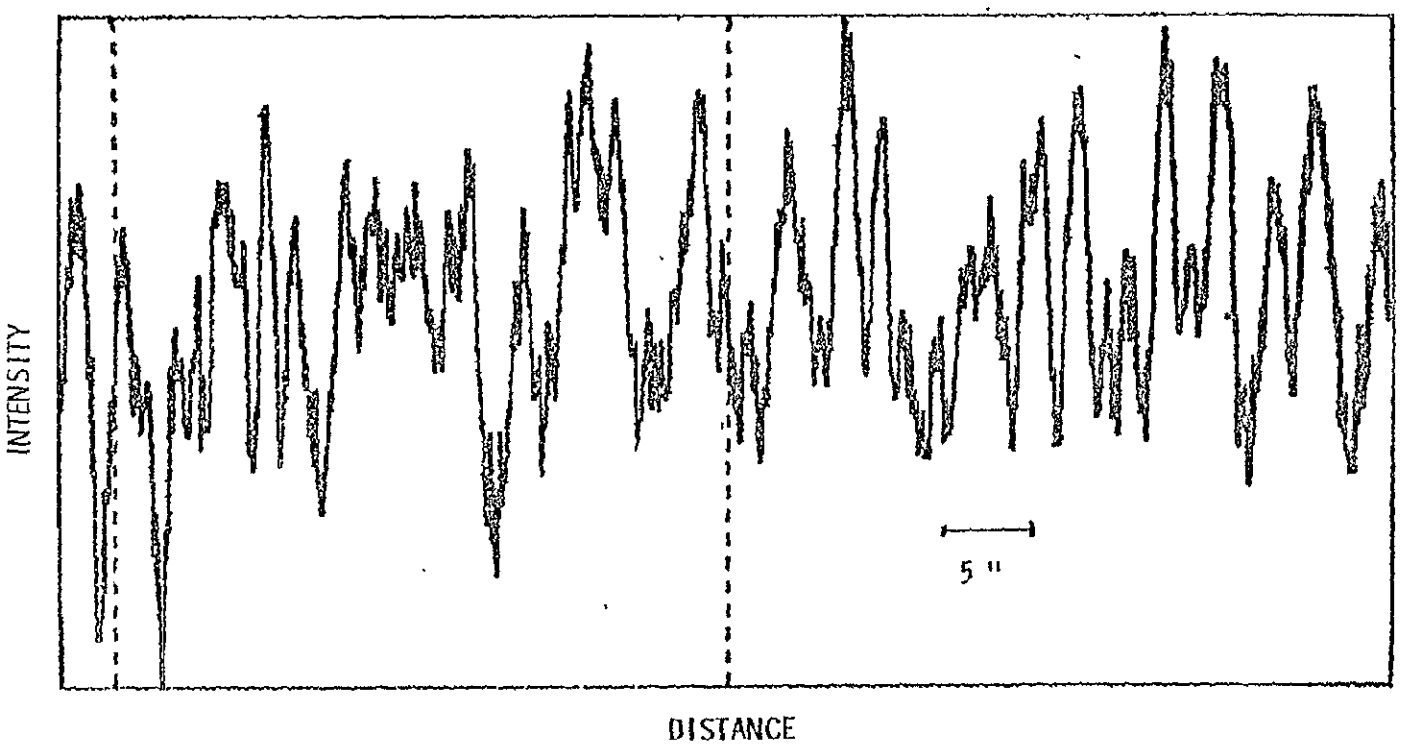

Fig. 3-1 Tracing of a Granulation Scene

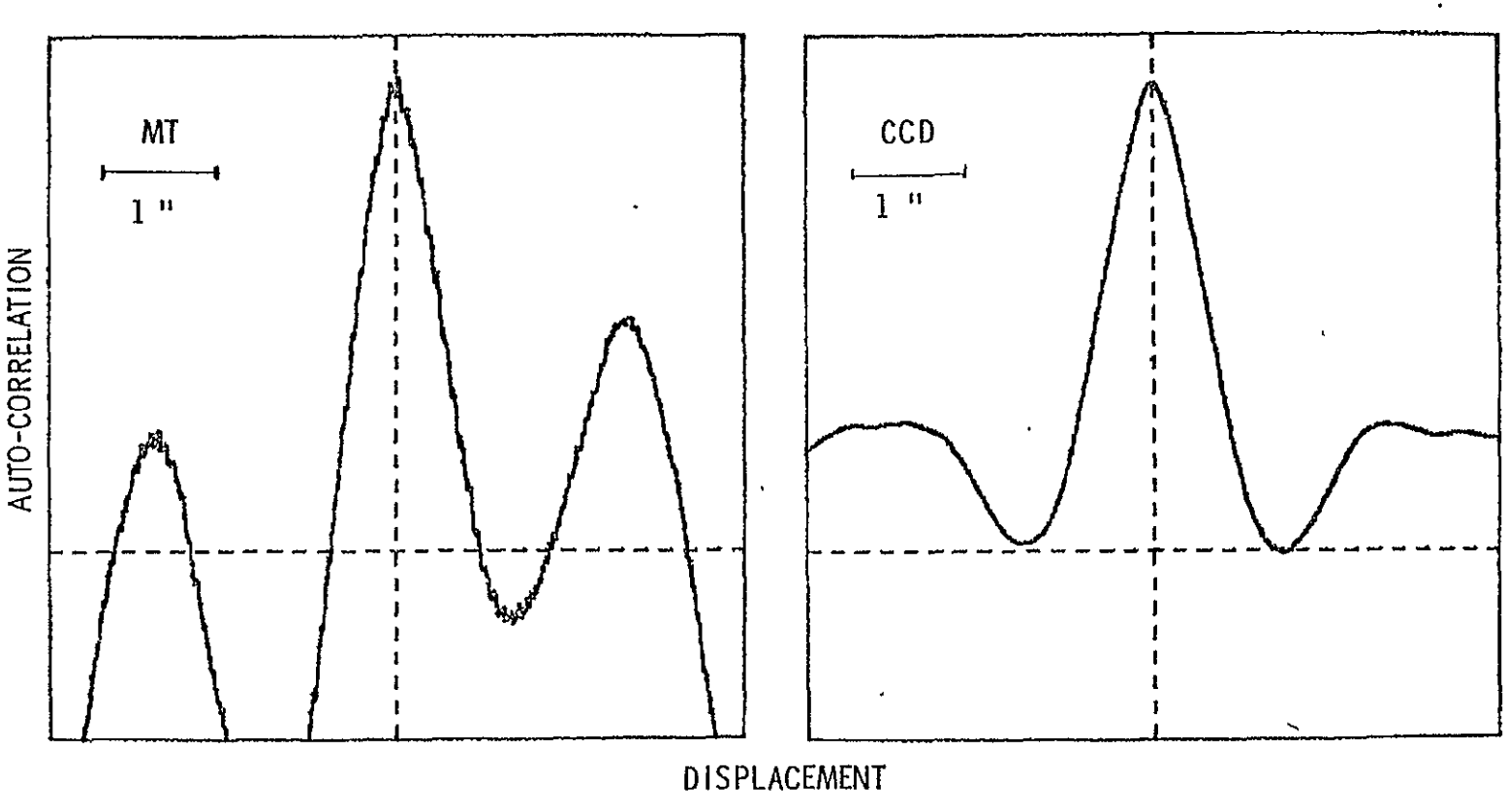

Fig. 3-2 Correlation Peaks for the Data of Fig. 3-1

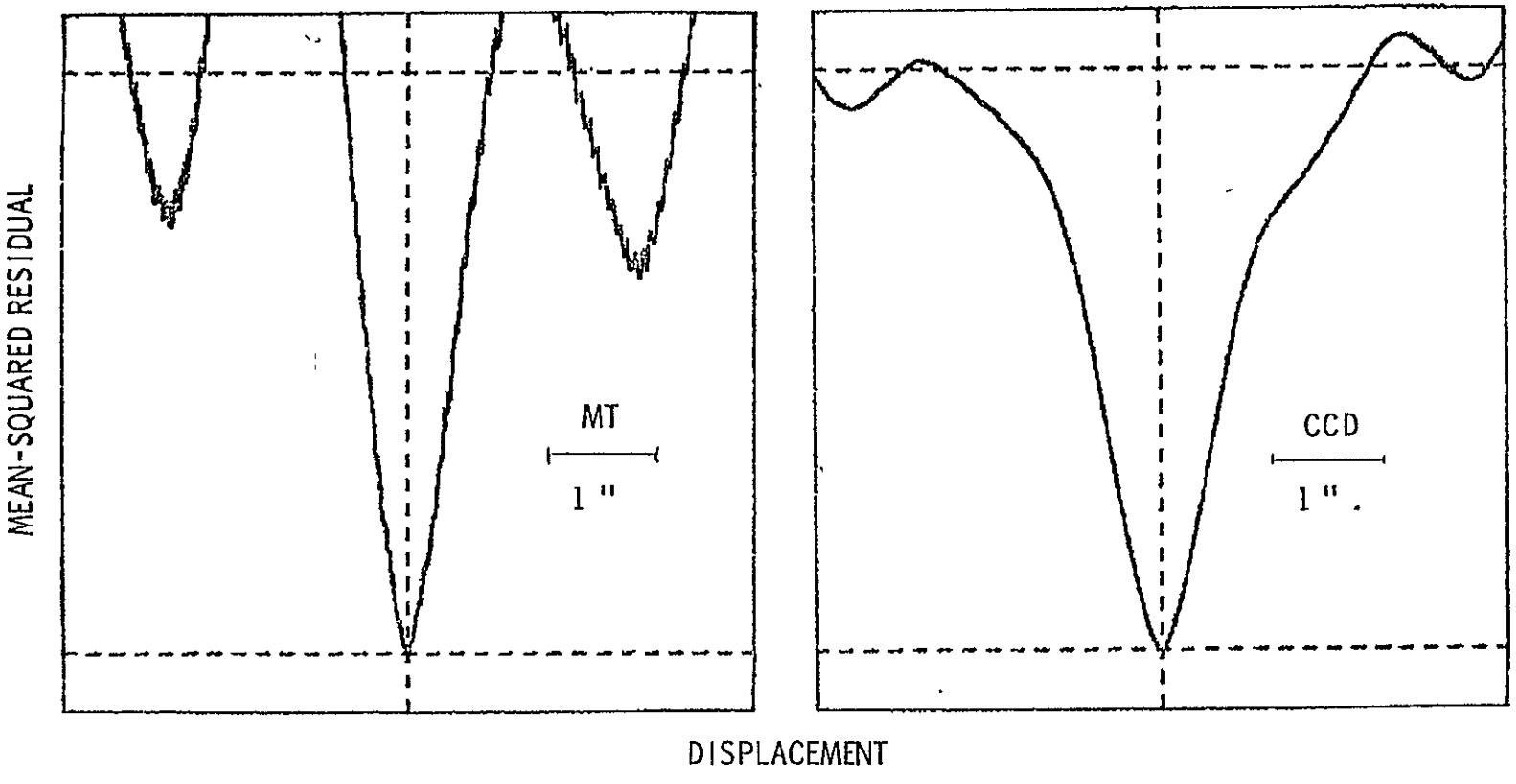

Fig. 3-3 Residual Functions for the Data of Fig. 3-1

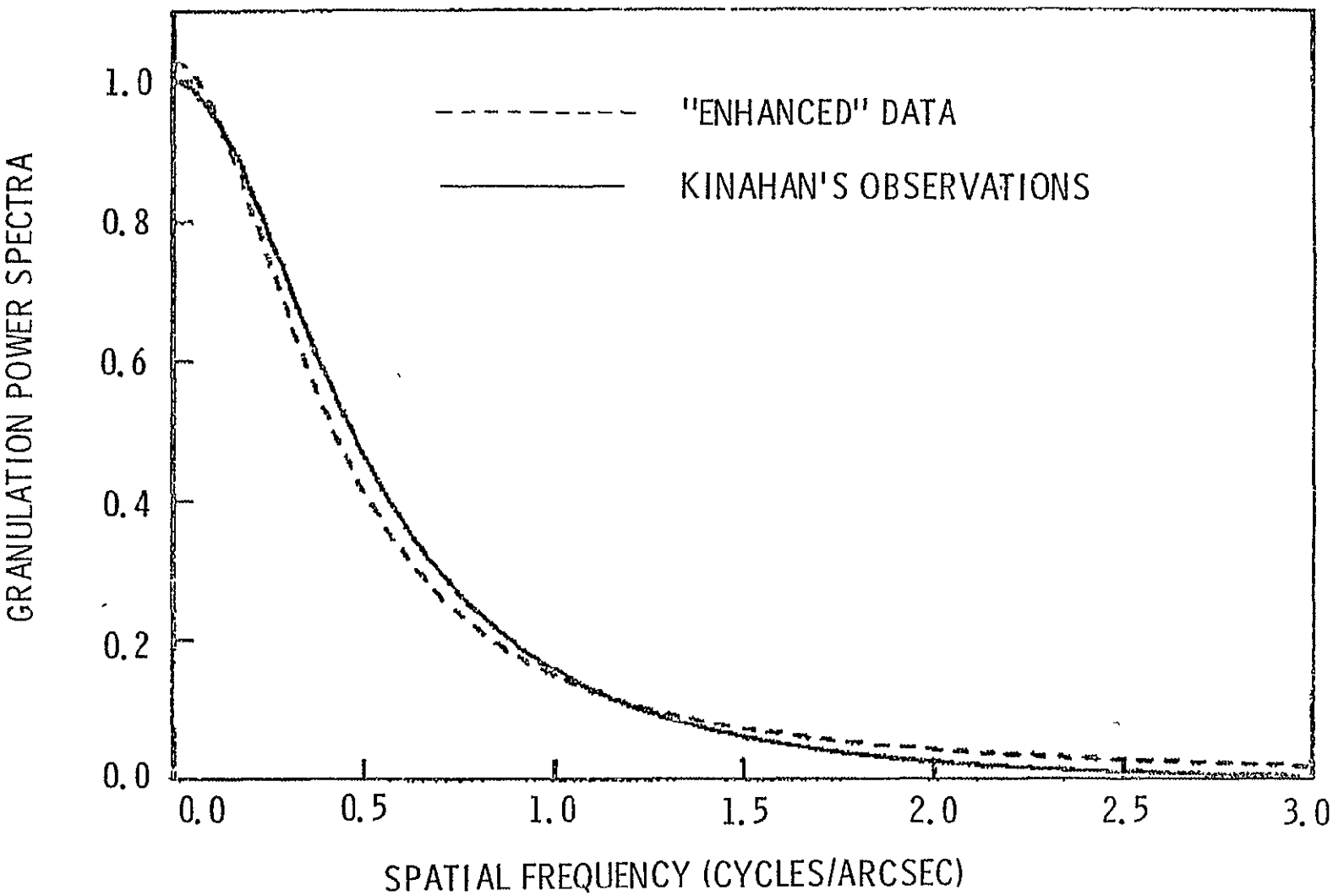

Fig. 3-4 Granulation Power Spectra

$$PSF\ (X) = \frac{\sin^2\left[\frac{\pi x}{X_o}\right]}{\left(\frac{\pi x}{X_o}\right)^2} \qquad (3\text{-}1)$$

where

$$X_o = 0.080'' \left(\frac{125\ cm}{D\ cm}\right)$$

and D is the diameter, 65 cm or 125 cm. Figure 3-4 shows that the 65 cm and 125 cm enhanced data yield plausible lower limits to tracker errors.

Finally, note that the intensity units used are arbitrary. All trackers were assumed to subtract the average level I_{av} before processing, and so the only important quantity is:

$$\Delta I_{rms} \equiv \frac{\langle (I - I_{av})^2 \rangle^{1/2}}{I_{av}} \qquad (3\text{-}2)$$

The effective signal-to-noise ratio for detecting intensity fluctuations is $SN \sim \Delta I_{rms}$, and all noise errors depend on this product. For the solar granulation, recent measurements seem to be converging on $\Delta I_{rms} \approx 10\%$ at disk center (Refs. 1-4); it increases to 15-20% at a heliocentric angle of 50° and then decreases, falling to zero within 5 " of the limb (Ref. 5).

3.3 Time-Dependence of Tracker Errors

The granulation pattern within the tracker FOV changes in time so that correlation with a stored scene decreases. This causes noise errors to increase with time and also necessitates updating, storing the new scene in memory, which permanently stores the tracker error at the instant of updating. Furthermore, motion of features in the tracker FOV can cause the aimpoint or stable point of the tracker to move with a varying drift velocity $V_\alpha(t)$.

The auto-correlation function of the granular intensity pattern has been measured by Bahng and Schwarzschild (Ref. 1):

$$\langle I(t)\, I(o) \rangle = \langle I(o)^2 \rangle\ e^{-t/\tau_o}; \qquad (3\text{-}3)$$

$$\tau_o = 6.27 \text{ minutes};$$

where the brackets represent ensemble averages. This has been confirmed by recent unpublished work of J. P. Mehltretter. The spatial correlation

function, $< I(x, t)\, I(o,o) >$, broadens slightly as t increases. This broadening is consistent with transverse granule velocities, V_o, of 1 km/sec or 0.08 arcsec/min., root-mean-square. A tracker with large FOV containing many independent granules can be analyzed very accurately using these observed correlation functions. However, the present Marshall Tracker (Ref. 6) sees at most two distinct granules, and so sizable fluctuations about this average behaviour must be expected. It is not possible to describe these fluctuations without more specific knowledge about the time-dependence of individual small granules, and so this report is limited to study of average update times τu and errors.

If the correlation tracker is used to follow a specific feature on the sun, then tracker drift between updates is presumably caused by motion of the feature. In this case, only the accumulation of noise and systematic errors need be considered. The noise error, $\sigma_n(\Delta t)$, must be known as a function of the time interval since the last update, Δt; explicit expressions are derived for each tracker algorithm studied below. Whenever an image is stored in memory, a systematic error (rms value σ_s) is added, and, for each update after initial acquisition of the feature, a noise error (rms value $\sigma_n(\tau_u)$) is also stored. Therefore, after tracking for a total time interval $t = n\tau_u + \Delta t$, the "feature-following" error $E_{FF}(t)$ is given by

$$< E_{FF}^2(t) > = n\left[\sigma_s^2 + \sigma_n^2(\tau_u)\right] + \sigma_s^2 + \sigma_n^2(\Delta t). \qquad (3\text{-}4)$$

An optimum update time can always be found to minimize $< E_{FF}^2(t) >$, several examples of which are discussed below. In actual operation, the tracker should update when the correlation peak has decreased by a factor $EXP(-\tau_u/\tau_o)$, τ_u being the optimum value, and a distribution of actual update times will result.

If tracking in absolute coordinates with respect to the solar limb is desired, then tracker drift must be added to $< E_{FF}^2 >$. To estimate the drift rate, suppose that m independently moving features are present in the tracker FOV and that the drift velocity $V_\alpha(t)$ is the resultant of the m random velocities. Then $V_\alpha(t)$ has a mean-squared value of V_o^2/m, and, in absence of

any observational data, the auto-correlation function can be assumed to be

$$< V_\alpha (\Delta t)\ V_\alpha (o) > = \frac{V_o^2}{m} \quad e^{-\Delta t/\tau_o} \qquad (3\text{-}5)$$

With this, it is easy to show that the men-squared drift after a time interval Δt is:

$$< \left| \int_o^{\Delta t} V_\alpha (t)\, dt \right|^2 > \qquad (3\text{-}6)$$

$$= \frac{2\, V_o^2\, \tau_o}{m} \quad [\ \Delta t - \tau_o\ (1 - \quad e^{-\Delta t/\tau_o})\ ].$$

This model can provide reasonable bounds to tracker drift as follows. For an upper limit, assume that updating has no effect on the drift velocity. After a time $t = n\tau_u + \Delta t$, the <u>total tracker error in absolute coordinates</u> <u>E(t)</u> obeys

$$< E^2 (t) > \quad \leqslant \quad < E_{FF}^2 (t) > \qquad (3\text{-}7)$$

$$+ \frac{2V_o^{\,2}\, \tau_o}{m} \quad [t - \tau_o\ (1 - \quad e^{-t/\tau_o})\ ].$$

For a lower limit, assume that updating resets $V_\alpha (t)$ to a new, random value, which leads to the expression

$$< E^2 (t) > \quad \geqslant \quad < E_{FF}^2 (t) > \qquad (3\text{-}8)$$

$$+ \frac{2nV_o^{\,2}\, \tau_o}{m} \quad [\ \tau_u - \tau_o\ (1 - \quad e^{-\tau_u/\tau_o})\ ]$$

$$+ \frac{2V_o^{\,2}\, \tau_o}{m} \quad [\ \Delta t - \tau_o\ (1 - \quad e^{\Delta t/\tau_o})\ ].$$

The previous two equations can be used to bound tracker errors as a function of time and to find optimum update times. Clearly, the choice of m, the number of independently moving features seen by the tracker, is critical in determining the drift rate. In the following analyses, one feature for every 1.5 - 2 " in tracker length was assumed, corresponding to a typical granule diameter. However, there is some indication (J. P. Mehltretter, private communication) that clusters of several granules may move together. If true, this would necessitate a larger tracker FOV for a given acceptable drift rate. Two-dimensional simulation using a seeing-free granulation movie is necessary to settle the matter. Finally, the effects of solar

rotation would need to be compensated if a constant aimpoint with respect to the solar limb is required for more than about 30 seconds. (Assuming a shift of more than 0.1 " is unacceptable).

3.4 Marshall Tracker (MT) Simulation

(a) Mathematical Description

The tracking algorithm of the MT has been fully described above: see Section 2 - 9. It computes the "up" and "down" correlations, C_u and C_d, according to

$$\begin{matrix} C_u \\ d \end{matrix} (y') = \sum_{i=1}^{N_{el}} I_i (y_o \pm d) \, I_i' (y'). \qquad (3\text{-}8)$$

Here, $I_i(y_o \pm d)$ are the outputs of the i^{th} detector element in the stored up/down pictures, which correspond to the initial aimpoint y_o; $I_i' (y')$ is the real-time result, corresponding to the real-time aimpoint y'. Tracking error is zero when $y' = y_o$. These intensities are quantized in eight levels after subtraction of the average.

The stable point of the MT, y_o', is the value of y' where, in absence of noise,

$$C_u (y' = y_o') = C_d (y' = y_o'). \qquad (3\text{-}9)$$

Asymmetries in the observed correlation peaks cause the systematic error, given by

$$\sigma_s^2 \equiv \langle (y_o' - y_o)^2 \rangle, \qquad (3\text{-}10)$$

where the brackets represent averaging over an ensemble of scenes.

When the tracker is aimed at its stable point, noise in the measured intensities causes it to produce a noisy error signal, Δy_n. This error signal is

$$\Delta y_n = \frac{C_u (y_o') - C_d (y_o')}{\partial C (y') / \partial y'}. \qquad (3\text{-}11)$$

Its rms value, σ_n, is given by

$$\sigma_n^2 = \frac{2 \sigma^2 (C)}{| \partial C / \partial y' |^2}, \qquad (3\text{-}12)$$

where σ^2 (C) is the variance of C_u or C_d due to noise. It is shown in Appendix A that

$$\sigma^2 (C) = p\, \Delta I^2 [2 \sum_i I_i^2 + N_{el}\, p\, \Delta I^2]; \qquad (3\text{-}13)$$

$$p = \frac{0.698\, I_{av}}{SN \cdot \Delta I}. \qquad (3\text{-}14)$$

ΔI is the quantization unit, approximately equal to $5\, I_{av}\, \Delta I_{rms}/8$, and p is the probability of a noise-induced quantization error.

The preceding equations accurately describe tracker errors in one dimension. Since the x and y directions are handled independently by the MT, the simulation values of σ_n and σ_s reported in the next section have been multiplied by $\sqrt{2}$.

(b) Fixed-Scene Results

Noise and systematic errors were evaluated from eqns. (3-10) and (3-12) using the same granulation trace to evaluate the stored and real-time intensities. The Standard MT (Ref. 6) was defined by:

$$\begin{aligned} SN &= 100, \quad \Delta I_{rms} = 10\% \\ N_{el} &= 66 \\ d &= 0.05". \end{aligned} \qquad (3\text{-}15)$$

A large number of trackers with variations on these standard values were studied three times each, using ground data, 65 cm, and 125 cm enhanced data.

Figure 3-5 gives an approximate summary of these results, while detailed plots are shown in Figures 3-6 through 3-11. On all of these plots, errors are given in hundreths of an arcsecond. The solid line represents ground data (upper limits) and the dashed and dotted lines represent 65 cm and 125 cm enhanced data, respectively (lower limits). Noise errors for the standard MT lie between 0.018" and 0.034", depending on the type of data, and systematic errors are between 0.007" and 0.019". Therefore, total tracking errors for fixed scenes are in the range 0.019" to 0.039".

Noise errors for the MT are relatively insensitive to SN, varying as $SN^{-0.5}$. This happens because the quantization interval ΔI is much larger than the detector noise. Quantization acts as a nonlinear pre-amplifier,

- GROUND DATA: UPPER LIMITS

$$\sigma_N \approx 0.034'' \left[\frac{SN}{100} \cdot \frac{\Delta I_{rms}}{10\%}\right]^{-0.5} \left[\frac{N_{el}}{66}\right]^{-0.2} \left[\frac{d}{0.05''}\right]^{0.15}$$

2-SIGMA ERROR $\approx 2\,\sigma_N$, UNLESS OTHERWISE STATED

$$\sigma_S \approx 0.019'' \left[\frac{N_{el}}{66}\right]^{-0.3} \left[\frac{d}{0.05}\right]^{0.1}$$

- ENHANCED DATA: LOWER LIMITS

$$\sigma_N \approx \begin{pmatrix} 0.028'' \\ 0.018'' \end{pmatrix} \left[\frac{SN}{100} \cdot \frac{\Delta I_{rms}}{10\%}\right]^{-0.5} \left[\frac{N_{el}}{66}\right]^{-0.5}$$

$$\sigma_S \approx \begin{pmatrix} 0.008'' \\ 0.007'' \end{pmatrix} \left[\frac{N_{el}}{66}\right]^{-0.5} \left[\frac{d}{0.05''}\right]^{0.3}$$

UPPER NUMBER FOR 65-CM DATA, LOWER FOR 125 CM

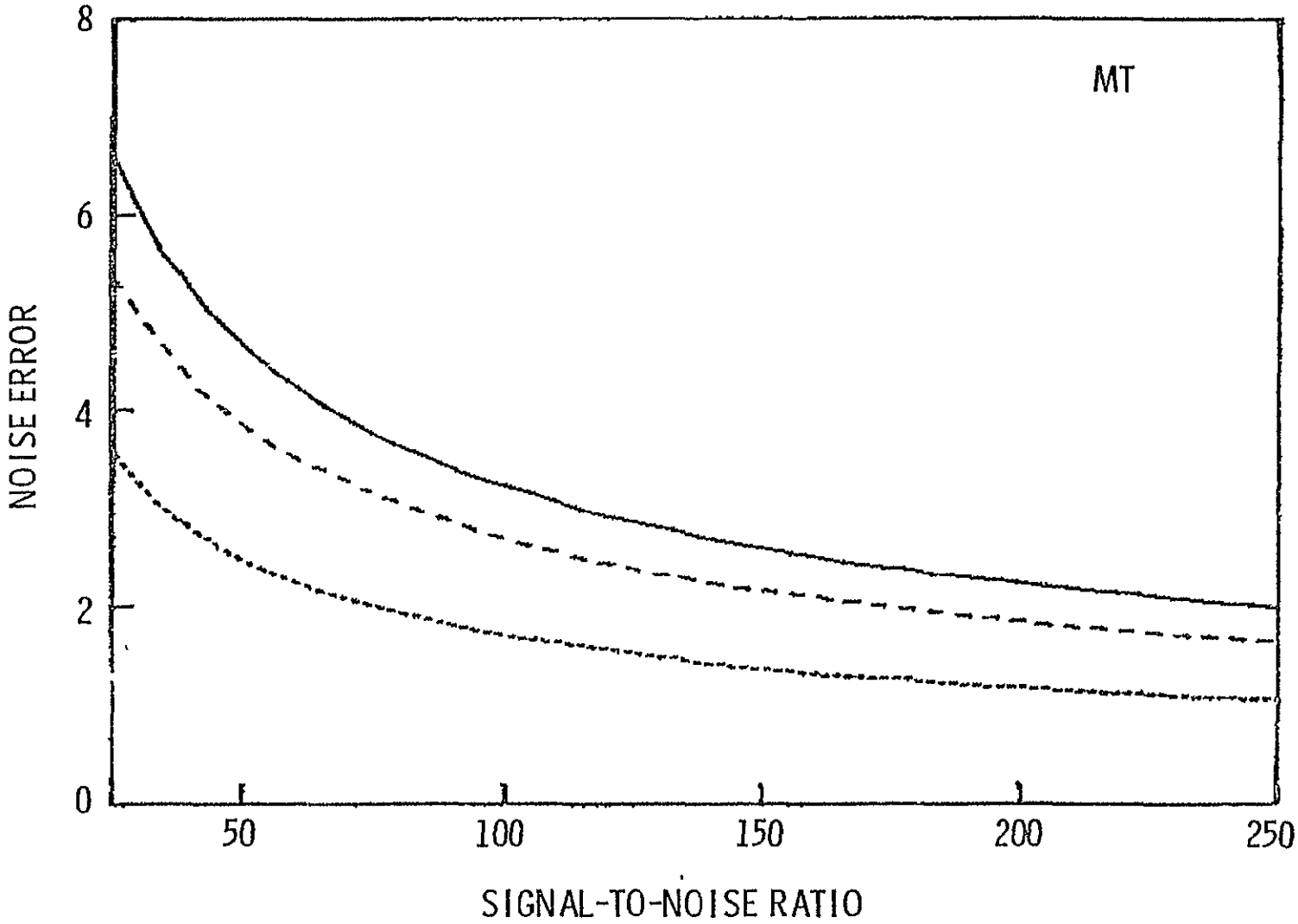

Fig. 3-6 MT Noise Errors (Centi-Arcseconds). From top to bottom, curves show results from ground data, 65 cm, and 125 cm enhanced data

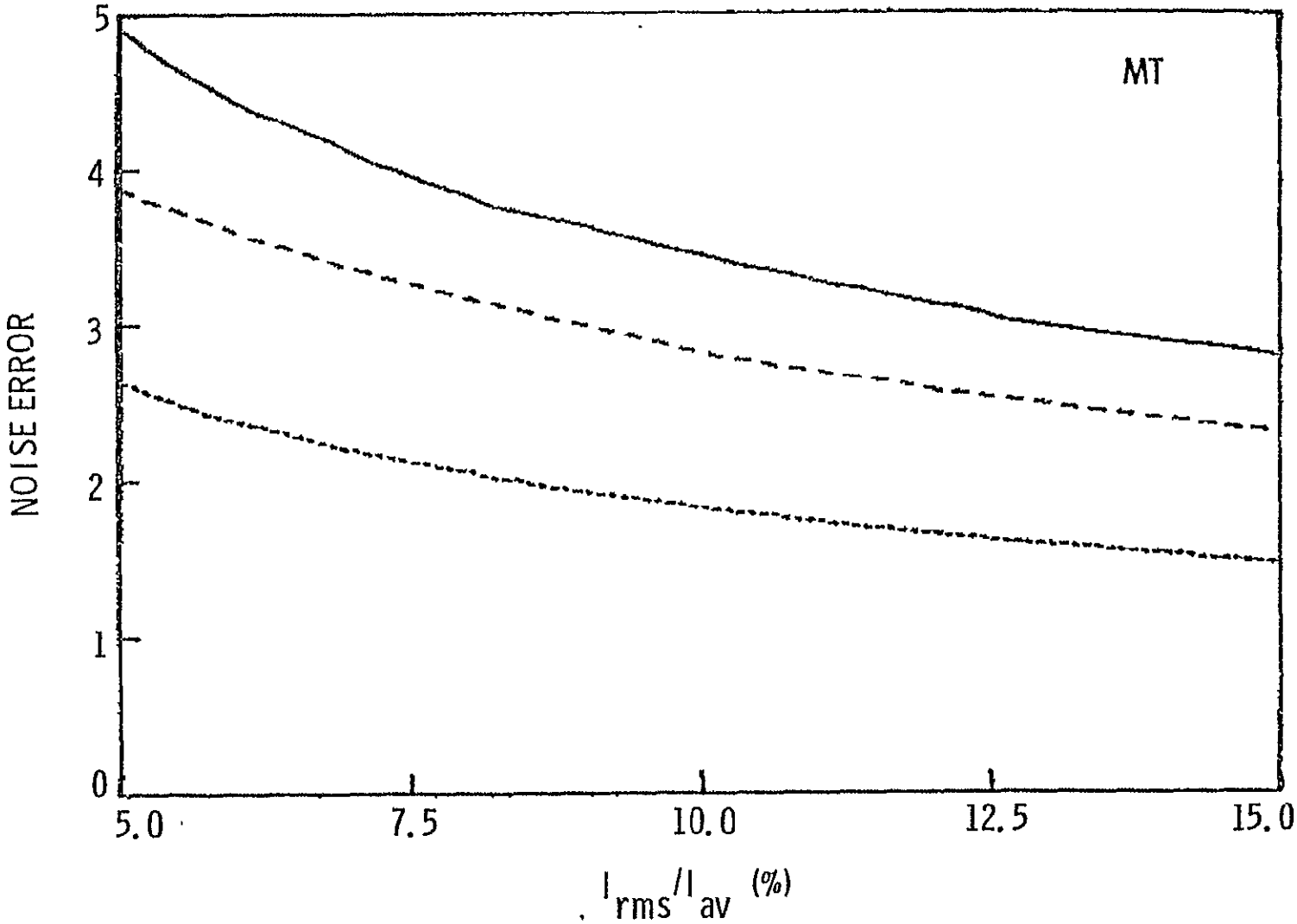

Fig. 3-7 MT Noise Errors Versus Granular Contrast

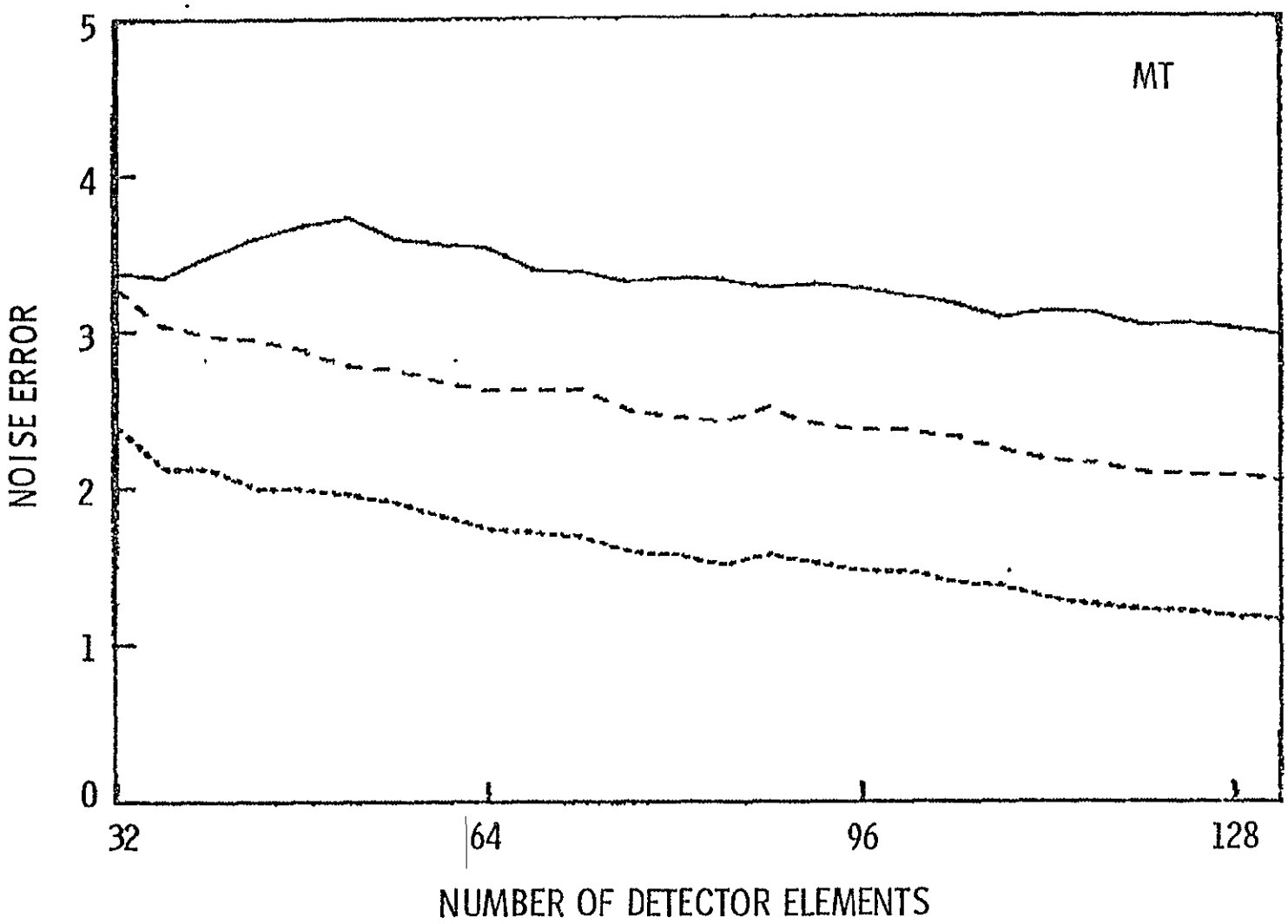

Fig. 3-8 MT Noise Errors Versus N_{el}

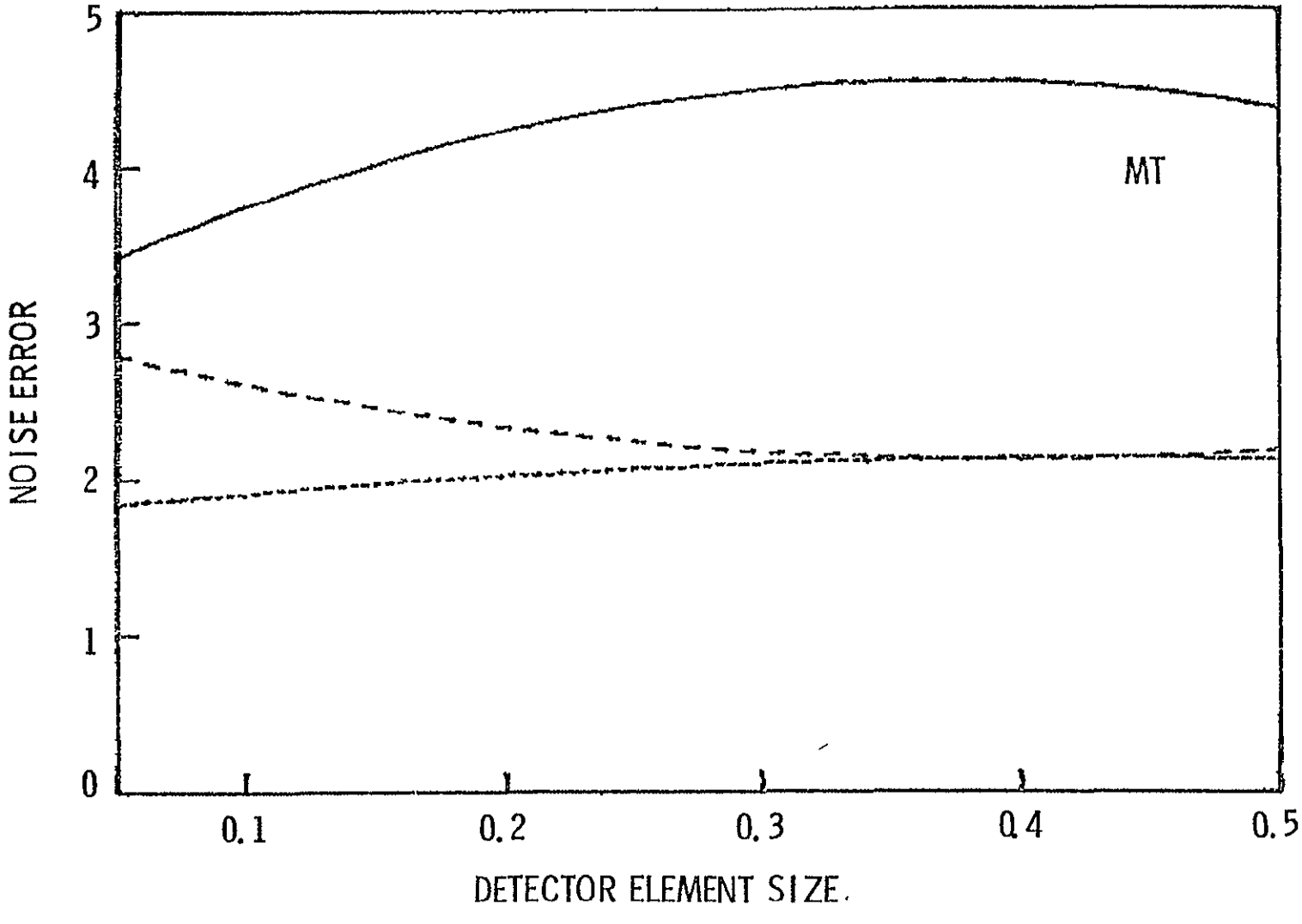

Fig. 3-9 MT Noise Errors Versus Image Scale

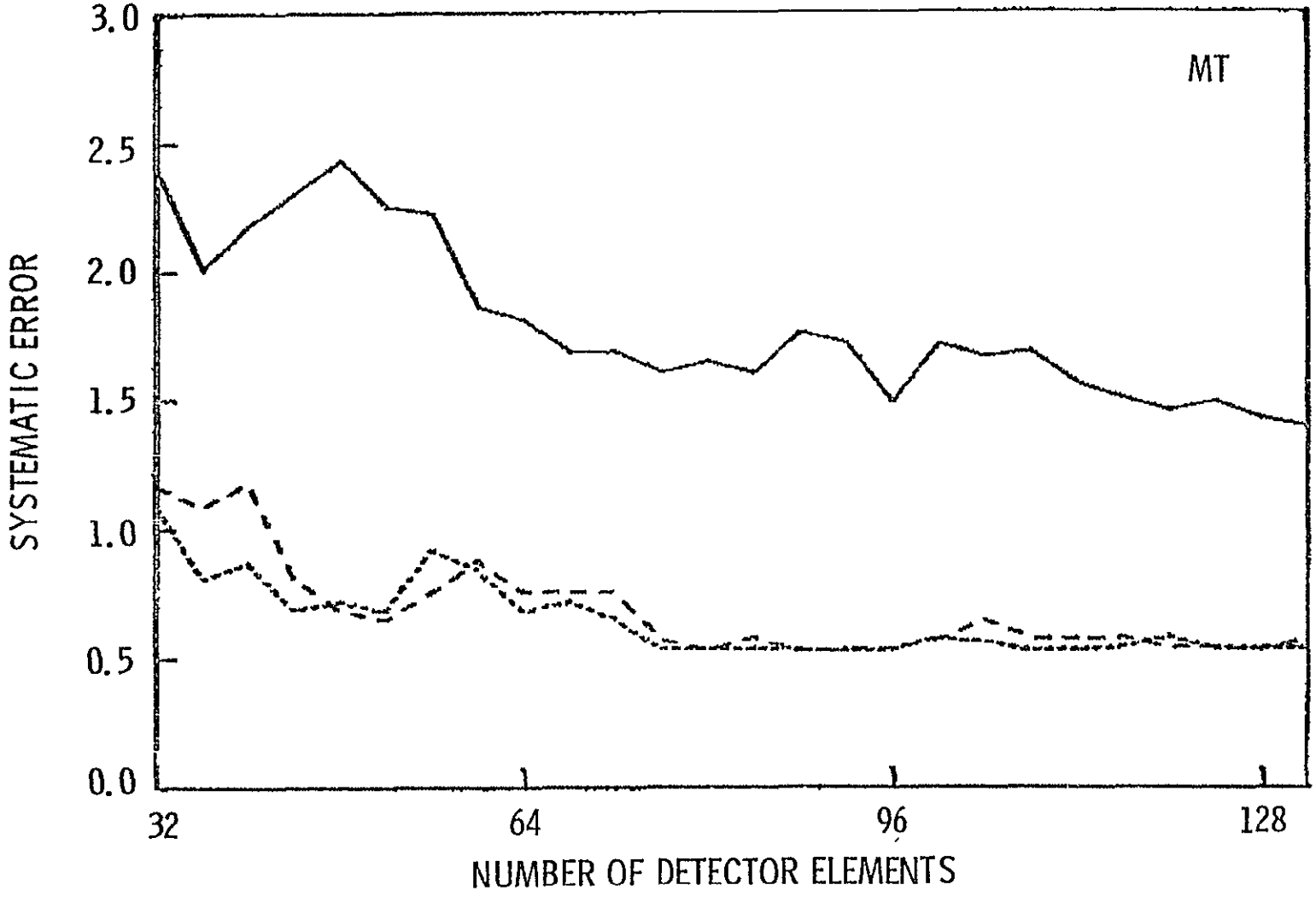

Fig. 3-10 MT Systematic Errors Versus N_{el}

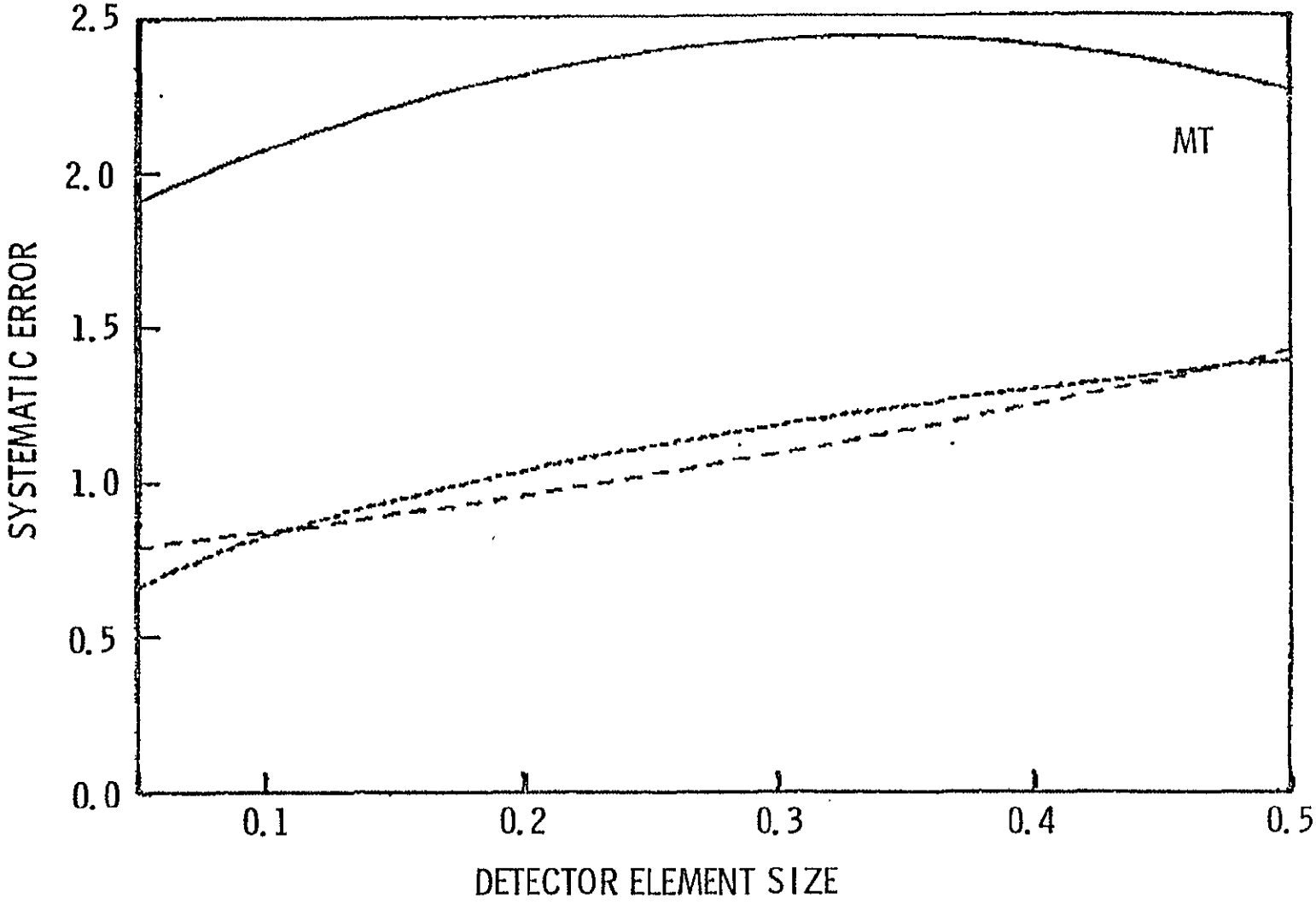

Fig. 3-11 MT Systematic Errors Versus Image Scale

converting small intensity changes to large, fixed increments in I_i. Other simulations show that finer quantization, say 10-bit instead of 3-bit, would lead to larger tracker errors when SN $\sim$ 100 but improved performance if SN were increased to 500. Figure 3-7 is included to show that a change in granular contrast, ΔI_{rms}, is equivalent to a change in SN, only their product being relevant.

Both noise and systematic errors decrease roughly as $N_{el}^{-0.5}$, as shown in Figures 3-8 and 3-10; the slower decrease for ground data is a result of correlation peak broadening as N_{el} increases. The noisy behaviour of the systematic errors, which are averages over 100 independent scans, shows the large variation in tracker performance from scene to scene. This sensitive scene-dependence would also have appeared in Figures 3-9 and 3-11, showing dependence on image scale: however, these are smooth curves fitted through three (five for ground data) simulation points. Recall that d, the detector element size in arcseconds, is also a scale factor for the effective focal length. Errors are surprisingly insensitive to d over the range plotted, but increasing d must eventually cause very large errors when elements become too large to resolve dark lanes and bright granules.

(c) Time Dependence of Errors

Two additional items of information are needed before the model of Section 3.3 can be applied to the MT. First, the Standard MT scan pattern is a circle 1" in diameter. Therefore, although the tracker length is 3.14" or $\sim$ 1.5 granule diameter, the MT only sees one independently moving feature: m = 1 in eqns. (3-7) and (3-8). Second, Appendix A shows that

$$\sigma_n(\Delta t) = \sigma_n(o) \quad e^{\Delta t/\tau_o}, \qquad (3\text{-}16)$$

where Δt is the time since the last update, $\sigma_n(o)$ is the fixed-scene noise error, and τ_o is the correlation time (Ref. 1), 6.27 minutes.

In all plots of time dependence, errors are in centi-arcseconds and times are in minutes. Solid curves show upper and lower limits to absolute errors from eqns. (3-7) and (3-8); dashed curves show feature-following errors (eqn. 3-4).

Errors for the Standard MT with ground data are shown in Figure 3-12 for times between zero and ten minutes. The update time, 30 seconds, is

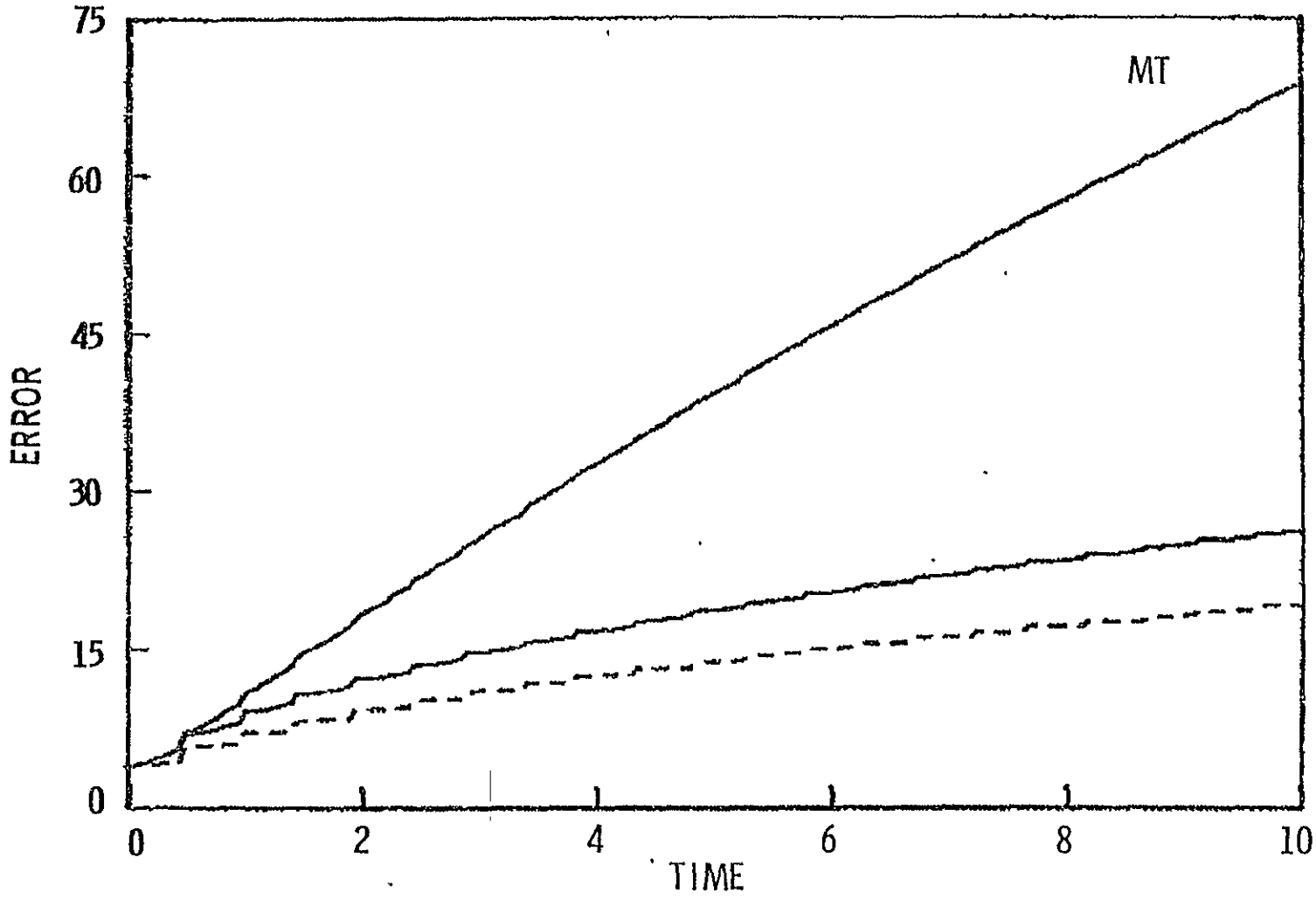

Fig. 3-12 MT Errors Versus Time. Dashed curve is feature-following error, solid curves are absolute error limits

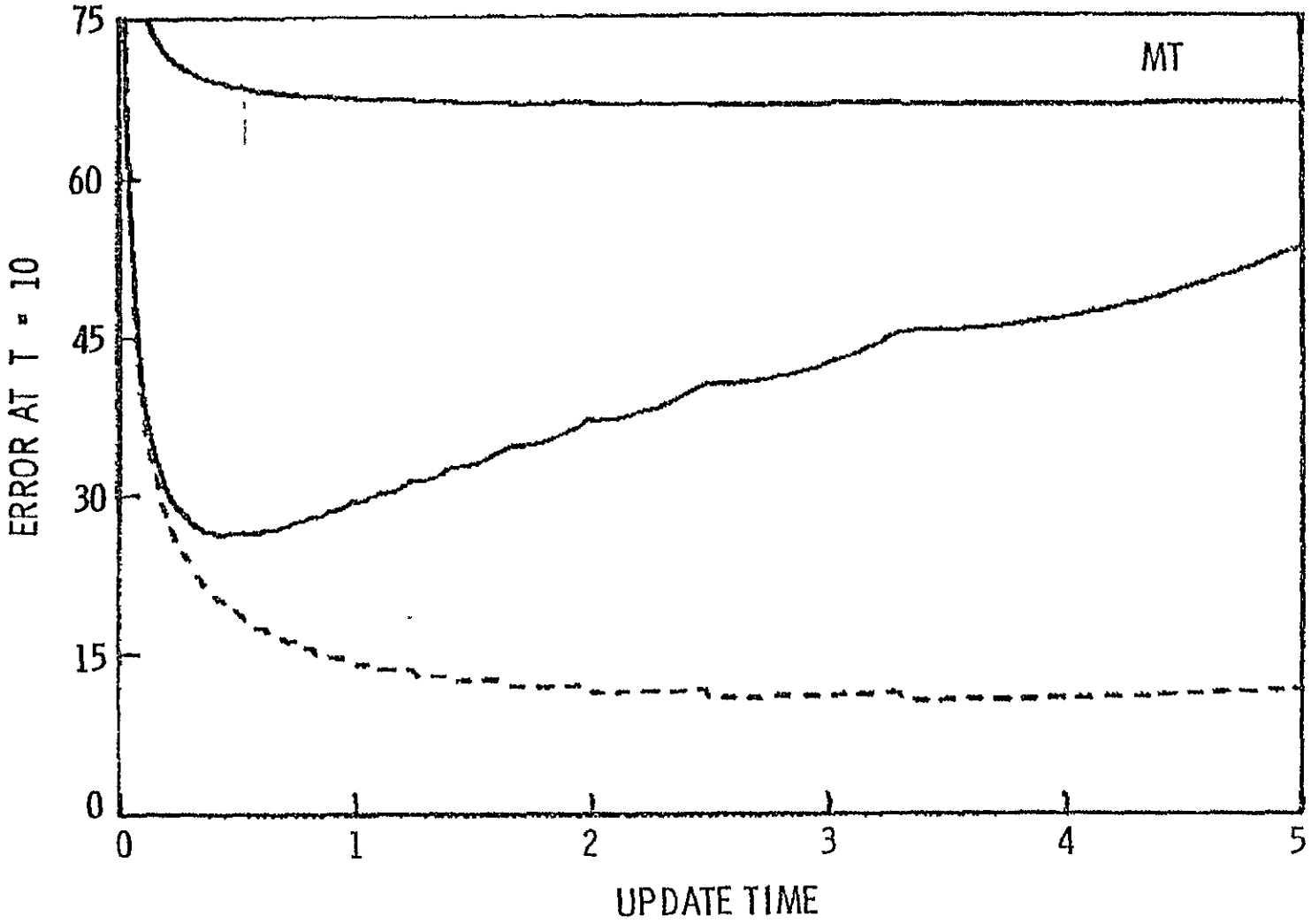

Fig. 3-13 MT Errors After 10 Minutes Versus Update Time

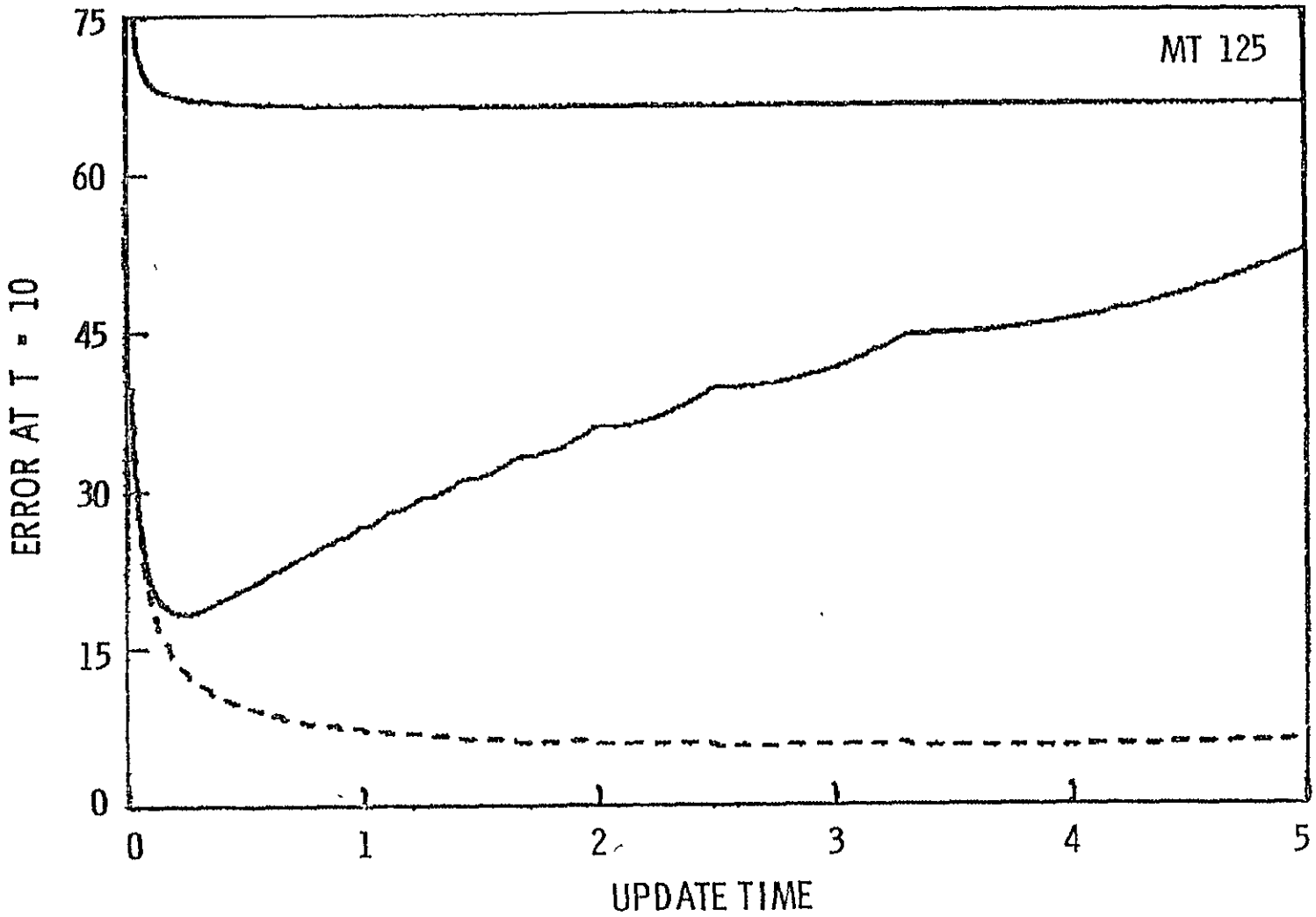

Fig. 3-14 MT Errors for 125 cm Data

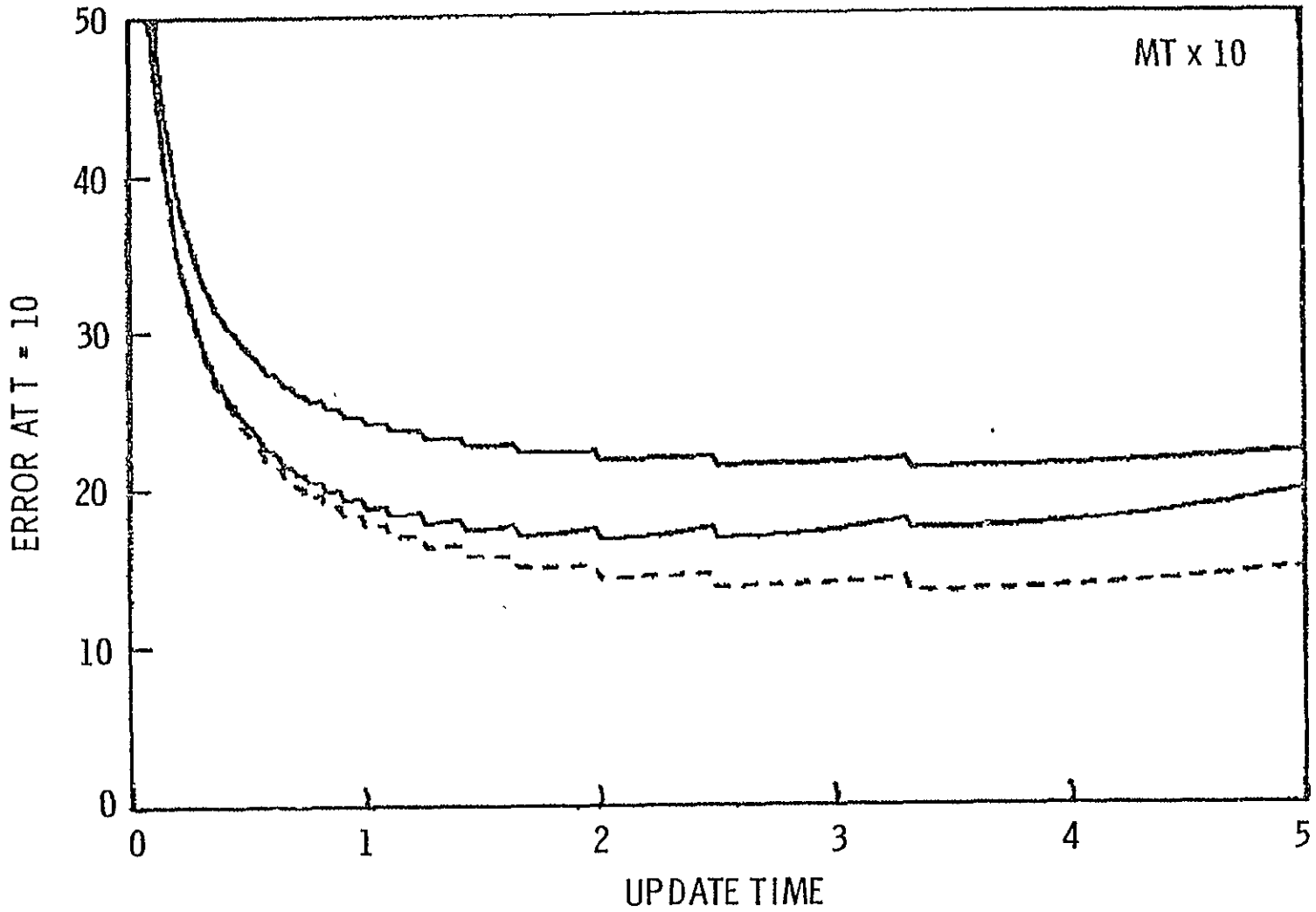

Fig. 3-15 Errors for MT With FOV Increased Tenfold

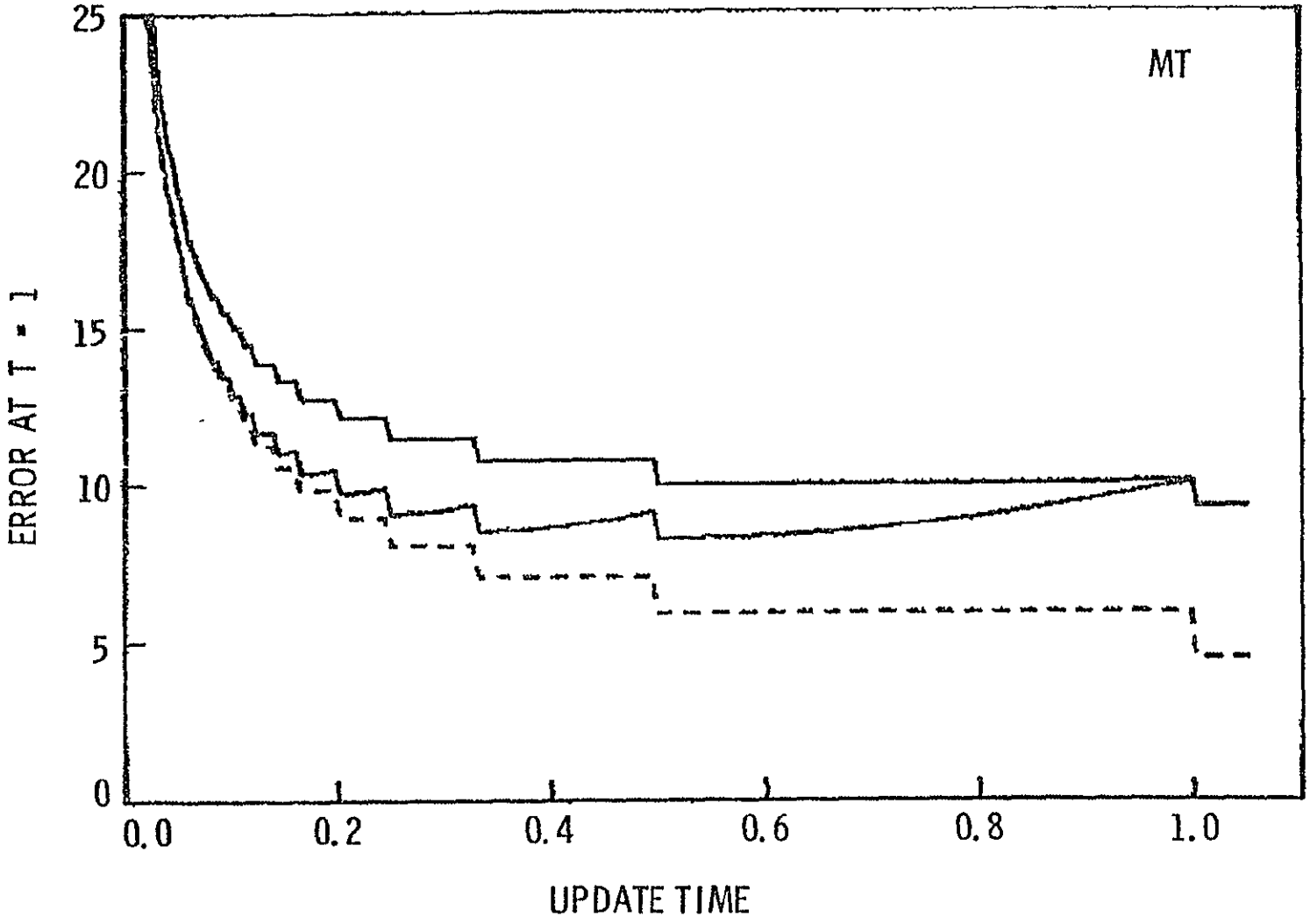

Fig. 3-16 MT Errors After 1 Minute

chosen to minimize the absolute tracking errors, the solid lines. More informative are plots of the expected tracking errors after a fixed time interval (say, ten minutes) as a function of update time τ_u, as in Figure 3-13. It is evident that feature-following requires $\tau_u \approx 3$ mins. for optimum performance, whereas absolute tracking calls for τ_u in the range of 30 secs. to one minute. Regardless of τ_u, the Standard MT shows large absolute tracking errors, between 0.3" and 0.7" after ten minutes.

Improved telescope resolution, using 125 cm enhanced data, reduces feature-following errors but has no effect on the drift rates, as seen from Figure 3-14. The only way to obtain absolute tracking near the noise limit is to increase the tracker FOV to include many granules. Figure 3-15 plots the same error curves when the MT uses 66 elements 0.5" long around a circle of 10" diameter (i.e., the Standard MT with d increased to 0.5"); 16 independent granules are assumed in this FOV. Although the noise errors are increased, absolute tracking to better than 1/4" over a ten minute period is possible.

In some applications, such as use in conjunction with a second guider, the MT may only be required to track for short periods of time. Errors of the standard MT after one minute are plotted in Figure 3-16: updating is undesirable, and drift is only slightly larger than the fixed-scene errors. Even so, the tracking error is still comparable to a 125 cm telescope's resolution and is therefore unacceptable.

3.5. Modified Marshall Tracker (MMT) Simulation

(a) Mathematical Description

A simple change in the MT algorithm has been found which reduces the fixed-scene errors considerably. Specifically, the MMT uses the "squared residuals function" $R(y')$ instead of the correlation function $C(y')$ used by the MT. This function is defined by

$$R_{\substack{u \\ d}}(y') \equiv \sum_{i=1}^{N_{el}} [I_i(y_o \pm d) - I'_i(y')]^2, \qquad (3\text{-}17)$$

where the symbols all have the same meanings as for the MT (see eqn. 3-8). It should be possible to convert the MT hardware to the MMT algorithm with

minor changes in the electronics. Figure 3-3 shows examples of the residual function as measured by the Standard MT (or MMT - the detector arrays are identical) and a CCD tracker described in Section 3.6.

The MMT locates a minimum in the residual function by the same method which the MT uses to find a correlation peak. Although noiseless, fixed scenes can be matched perfectly in principle by looking at the residual function, the MMT will have a non-zero systematic error when R is not a symmetrical function of displacement. The MMT stable point is defined by $R_u(y'_o) = R_d(y'_o)$, and the systematic error is again given by eqn. (3-10).

For fixed-scene noise errors, the MT equations (3-12) and (3-13) become

$$\sigma_n^2 = \frac{2\,\sigma^2(R)}{|\,\partial R/\partial y'\,|^2}\,; \qquad (3\text{-}18)$$

$$\sigma^2(R) = 2\,N_{el}\,p\,\Delta I^4. \qquad (3\text{-}19)$$

The quantities ΔI and p are again the quantization unit and the probability of error (see eqn. 3-14). Equation (3-19) is derived in Appendix A and is true only for fixed scenes with residual functions much broader than the element size d. Noise errors become much larger as the two scenes I_i and I_j' decorrelate, as discussed below.

(b) Fixed-Scene Results

For computer simulation, the Standard MMT was assumed to use the same detector array as the Standard MT: SN = 500, N_{el} = 66, d = 0.05". A summary of the fixed-scene errors is given in Figure 3-17. Noise errors for the Standard MMT are smaller by a factor of 4 to 7 depending on the data than those of the MT; systematic errors show less dramatic improvement. Nevertheless, total errors for fixed-scene tracking lie between 0.007" and 0.010": MMT errors are three to four times smaller for tracking over short time intervals (less than a minute) or for aligning two identical scenes for two different instruments.

Figures 3-18 through 3-22 give more accurate results than the rough formulae of Figure 3-17. Again, all plotted errors are in centi-arcseconds, and the three curves represent data-sets of different resolution. In general, the trends are similar to those discussed above for the MT. One curious

RESULTS FOR MMT

- NOISE ERRORS: ALL DATA

$$\sigma_N \approx \sigma_o \left[\frac{SN}{100} \cdot \frac{\Delta I_{rms}}{10\%}\right]^{-0.5} \left[\frac{N_{el}}{66}\right]^{-0.4}$$

WHERE

$$\sigma_o = \begin{cases} 0.0081'' & \text{GROUND DATA} \\ 0.0038'' & \text{65-CM DATA} \\ 0.0025'' & \text{125-CM DATA} \end{cases}$$

- SYSTEMATIC ERRORS: ALL DATA

$$\sigma_S \approx 0.0065 \left[\frac{N_{el}}{66}\right]^{-0.3} \left[\frac{d}{0.05''}\right]^{-0.3}$$

- THESE VERY LOW NOISE ERRORS ARE OBTAINED ONLY FOR FIXED SCENES; σ_N INCREASES RAPIDLY IN TIME AS THE SCENE CHANGES

Fig. 3-17

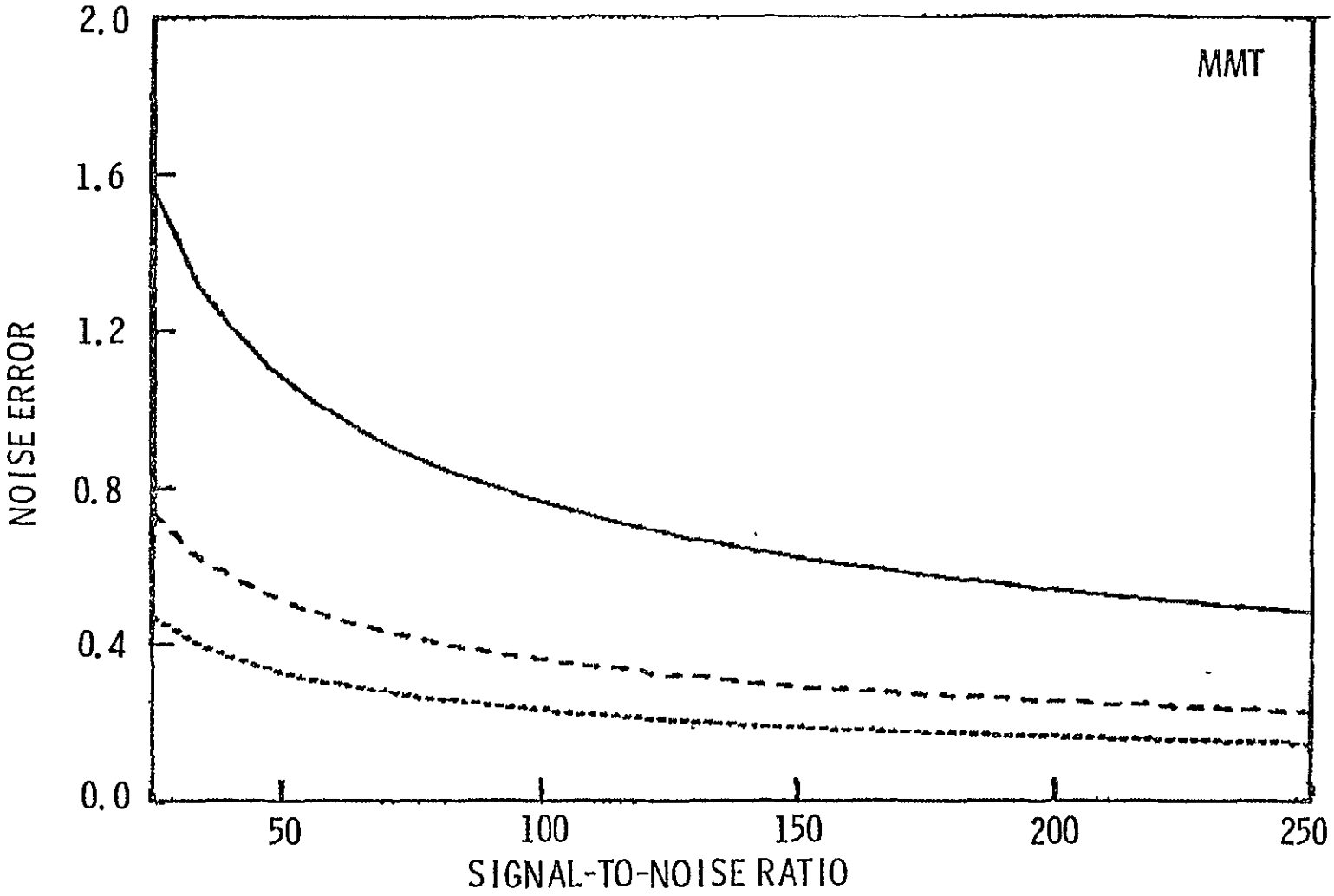

Fig. 3-18 MMT Noise Errors (Centi-Arcseconds). Results From Ground Data, 65 cm, and 125 cm enhanced data

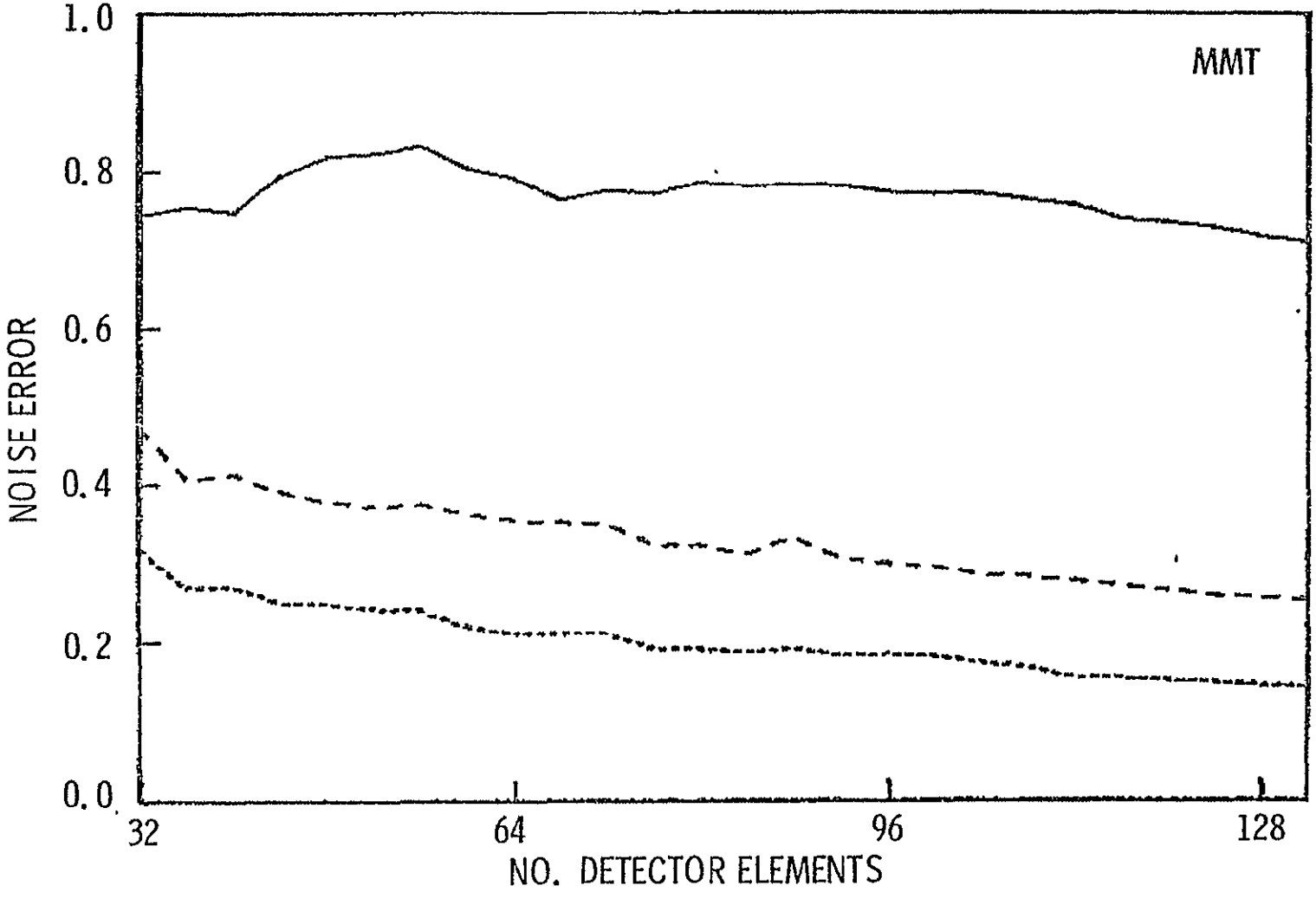

Fig. 3-19 MMT Noise Errors Versus N_{el}

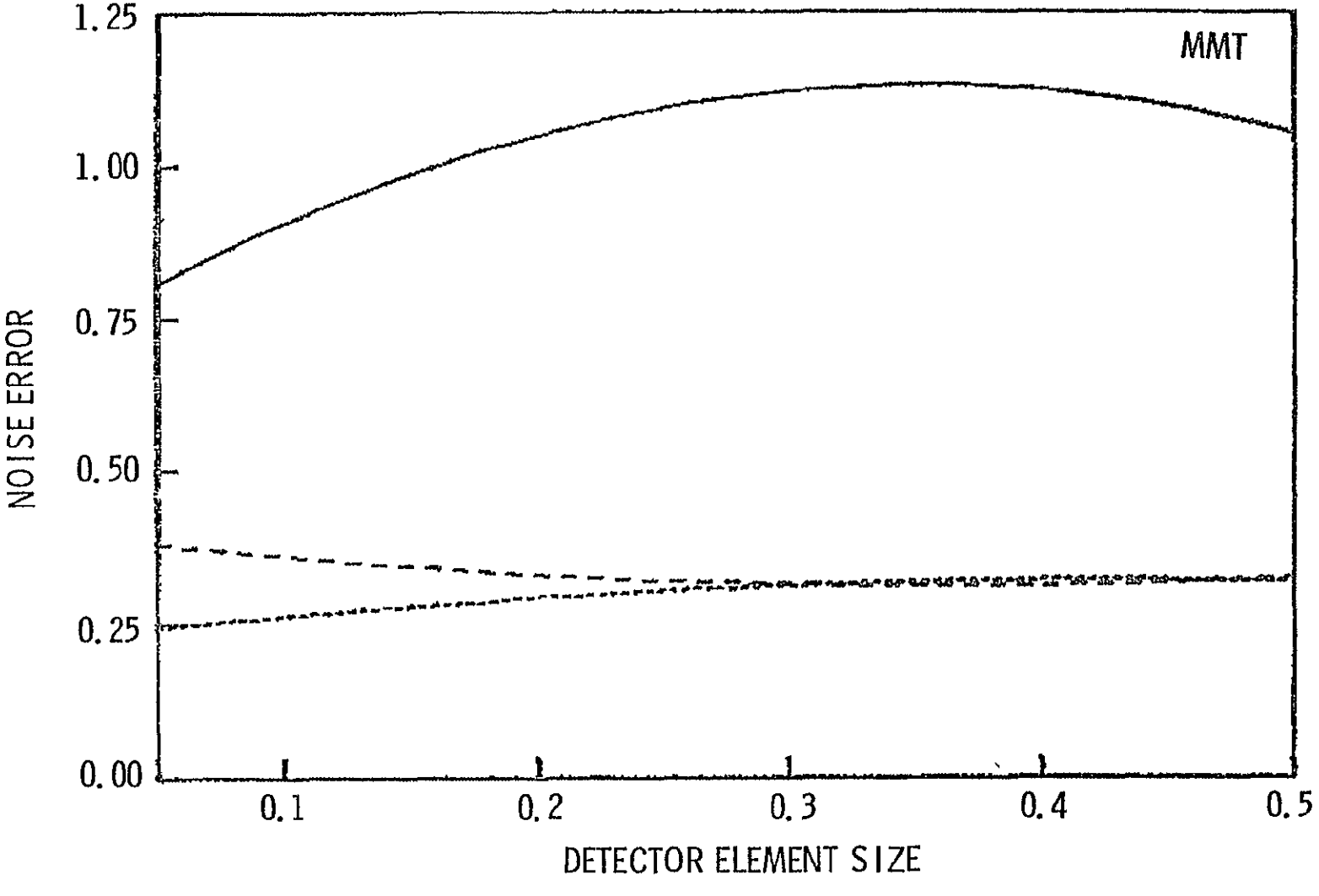

Fig. 3-20 MMT Noise Errors Versus Image Scale

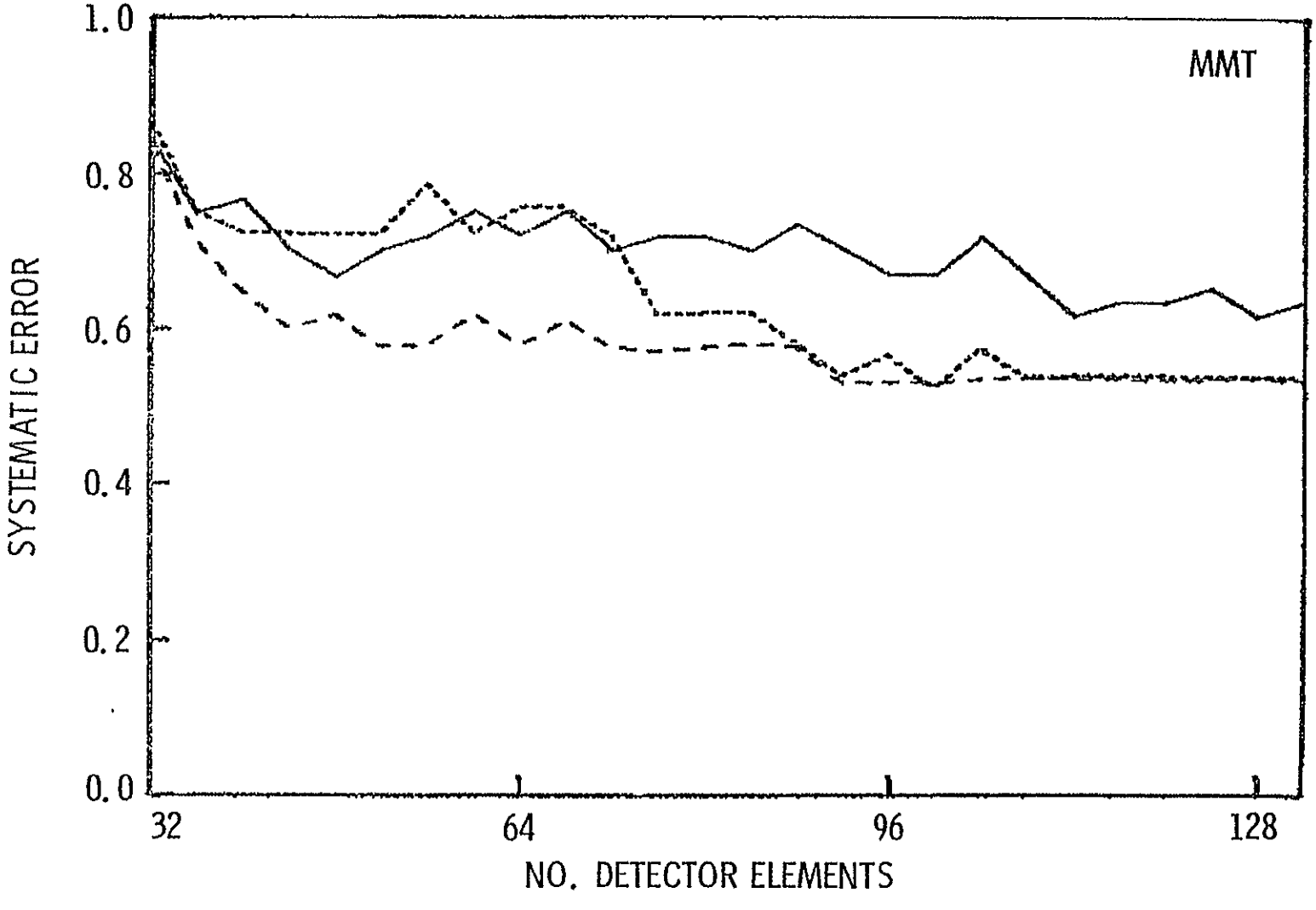

Fig. 3-21 MMT Systematic Errors Versus N_{el}

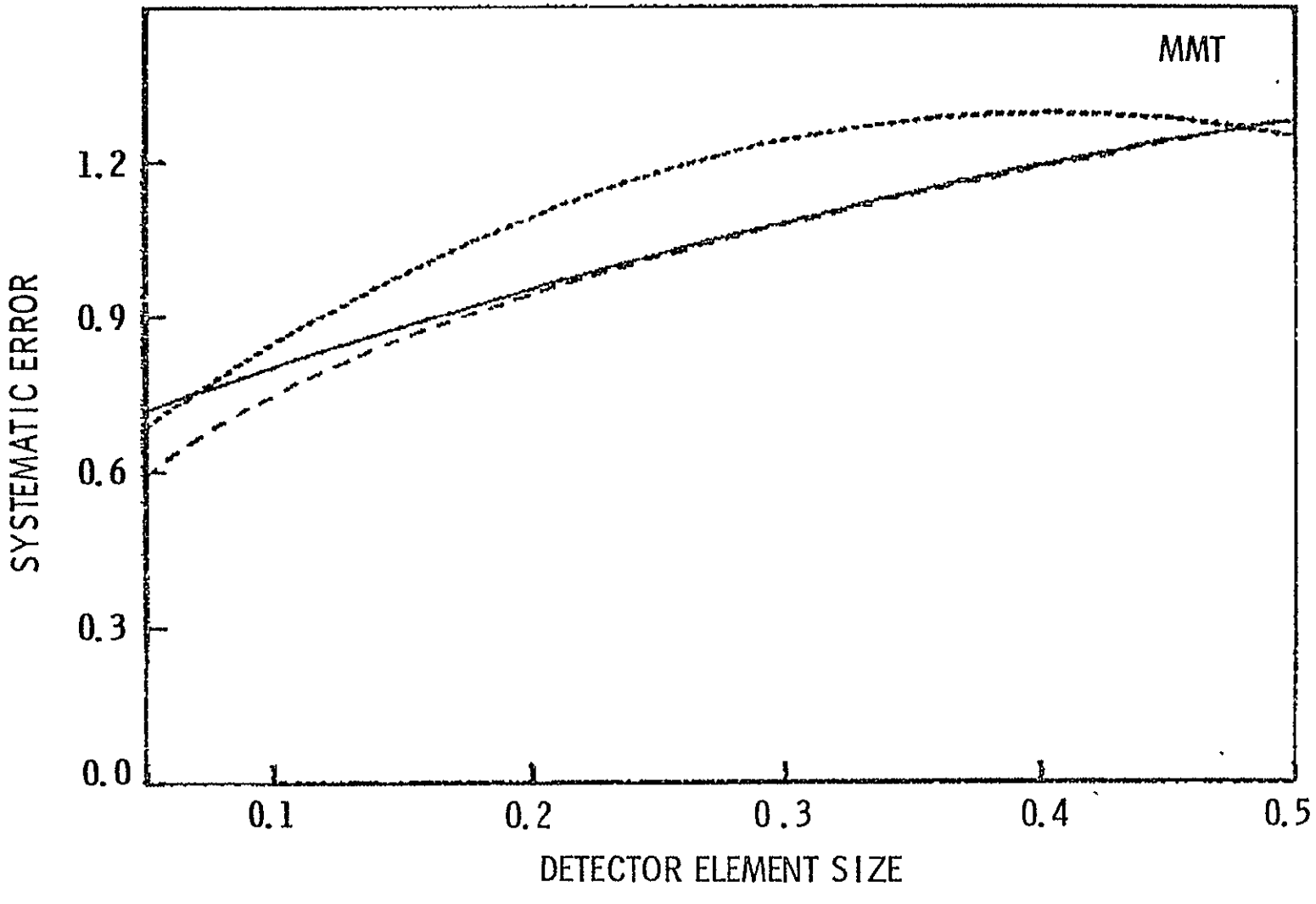

Fig. 3-22 MMT Systematic Errors Versus Image Scale

difference is that MMT systematic errors are essentially the same for all types of data used; this accounts for the reduced uncertainty for the total fixed scene errors.

(c) Time Dependence of Errors

Feature-following and absolute tracking errors are again calculated from eqns. (3-4), (3-7) and (3-8). For the Standard MMT, one feature in the FOV is assumed (m = 1). As the real-time scene changes, perfect cancellation of the stored scene in the residual function no longer occurs, and noise-signal cross-terms cause the noise error $\sigma_n(\Delta t)$ to increase rapidly. Appendix A shows that

$$\sigma_n^2(\Delta t) \approx \sigma_n^2(o)\ e^{2\Delta t/\tau_o}\left[1 + 20.5\left(1 - e^{-\Delta t/\tau_o}\right)\right]. \quad (3\text{-}20)$$

Figure 3-23 shows the feature-following and absolute errors (upper and lower limits) after ten minutes for the Standard MMT. Because of the rapid growth of noise errors, best update times are somewhat shorter than those for the MT. More frequent updating causes the feature-following errors and the most optimistic absolute errors to be about half those of the MT, although fixed-scene errors are three times smaller. The full advantage of the MMT is obtained for short time intervals, as comparison of Figures 3-24 and 3-16 shows.

Drift rates are of course identical for the MMT and the MT. They are greatly reduced by increasing the FOV ten-fold, as shown in Figure 3-25. With this image scale, absolute tracking to at least 0.2" accuracy over ten minutes is possible. For longer time, errors increase roughly proportional to the square root of the elapsed time.

3.6. CCD Tracker Simulation

(a) Mathematical Description

The CCD tracker which has been studied uses a detector array of two perpendicular lines of elements, which are analyzed independently. As usual, only one line was simulated and errors were increased by a factor of $\sqrt{2}$. Basically, the CCD tracker performs a least-square fit of the real-time scene to the stored scene, finding the position of minimum residuals.

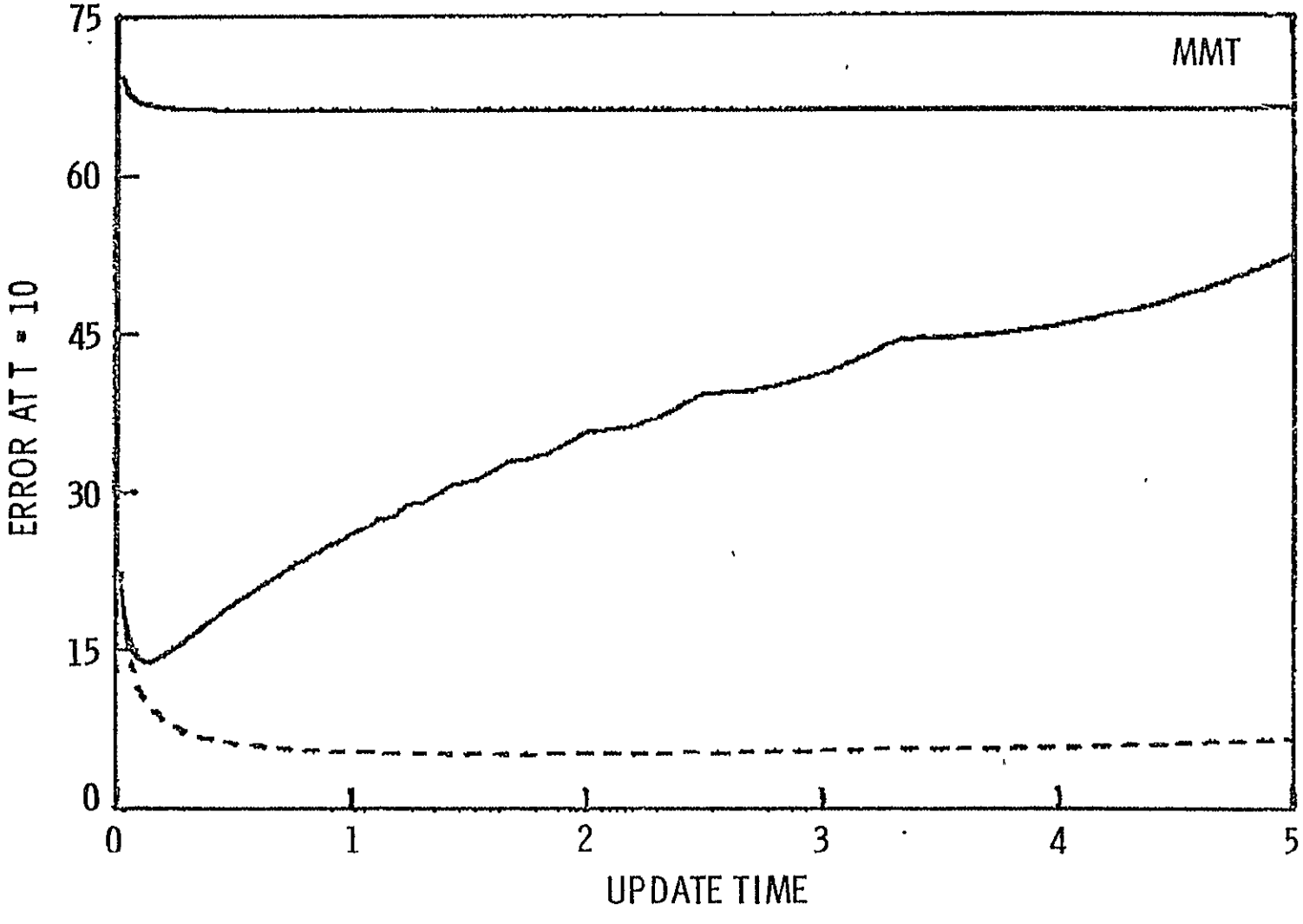

Fig. 3-23 MMT Errors After 10 Minutes (Feature-Following Errors and Bounds for Absolute Error)

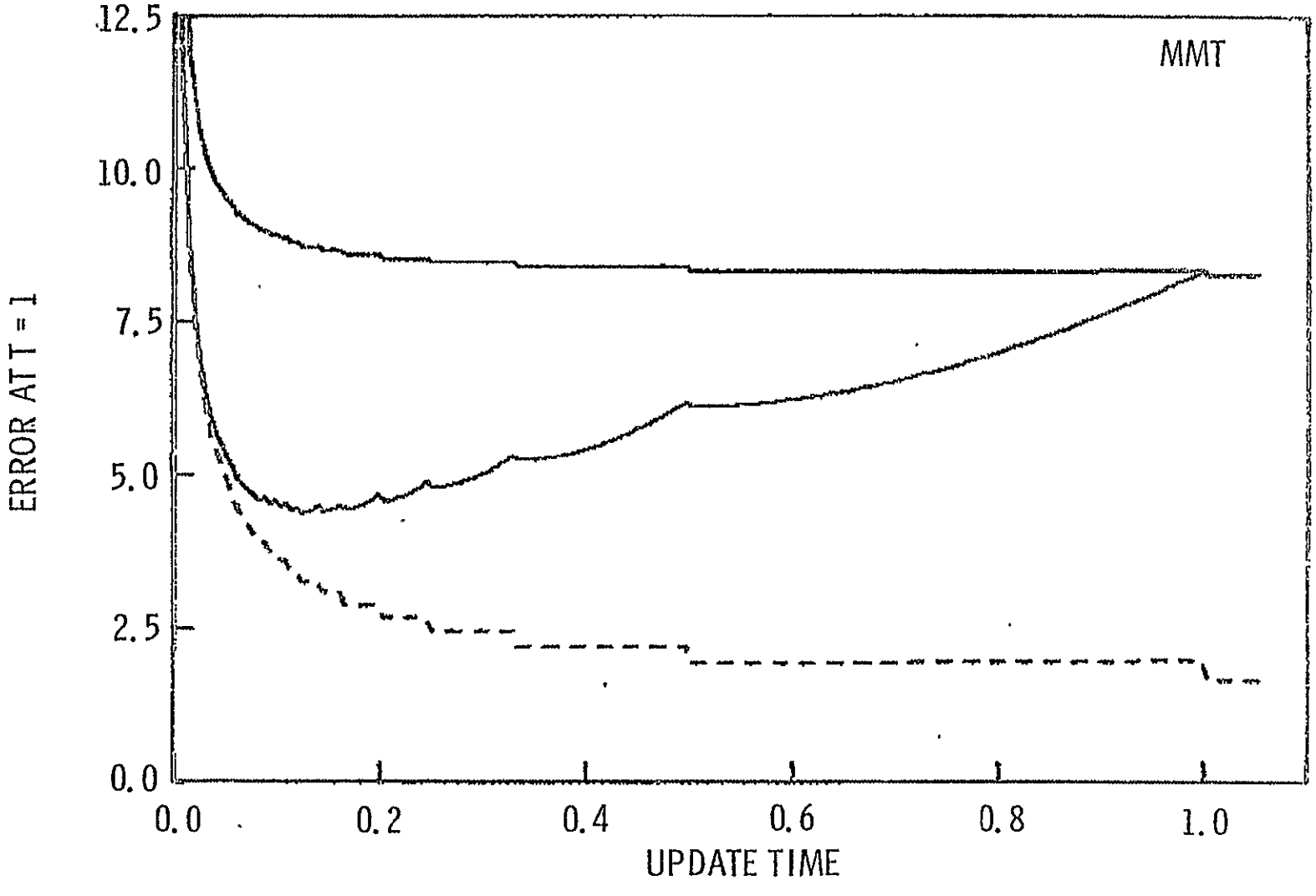

Fig. 3-24 MMT Errors After 1 Minute

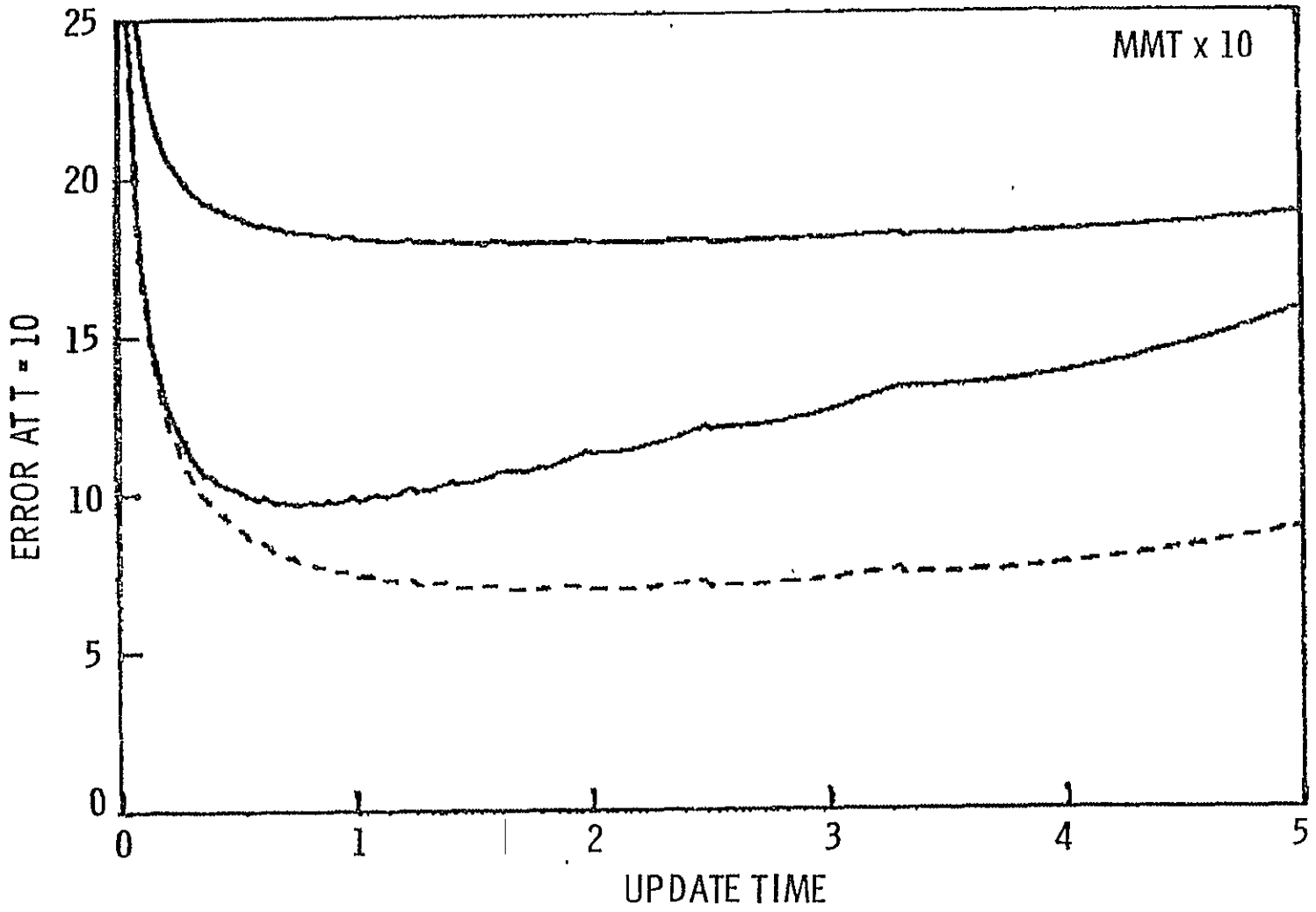

Fig. 3-25 Errors for MMT With FOV Increased Tenfold

The residual function is defined, as in eqn. (3-17),

$$R(y) \equiv \sum_{i=1}^{N_{el}} [I_i'(y, t) - I_i(0, 0)]^2 . \qquad (3\text{-}21)$$

Tracker stable point is the point $y_o(t)$ where $R(y_o)$ is an absolute minimum.

For simulation purposes, the detailed method of varying y to search for the stable point has not been specified: error results are therefore somewhat idealized lower limits to an actual CCD tracker's performance. However, it should be possible to approach these limits rather closely with an intelligently designed search algorithm and servo system. The real-time intensities $I_i'(y, t)$ are measured at evenly spaced points $y_i = y + (i - 1)\, d$, and so the approximate location of the stable point can be found from each measurement of the I_i'. Note that this requires the computing power to evaluate the residual function several times, using data interpolated from the measured I_i', for each real-time look at the scene.

The CCD tracker has two conceptual advantages over the MT, in addition to larger values of SN and N_{el}. First, quantization effects can be ignored, assuming ten bits are available, which allows the tracker to take full advantage of its increased sensitivity. Second, it is clear that the systematic error σ_s is always zero (recall that σ_s is the tracking error on fixed, noiseless scenes). Only noise errors and tracker drift need be considered.

The noise error σ_n for fixed-scene tracking is defined as follows. In the vicinity of $y = y_o$, the measured residual function R(y) is noisy with variance $\sigma^2(R)$, which is calculated is Appendix A. This noise causes the absolute minimum of R(y) to deviate from y_o. Then the rms noise error σ_n is one-half the interval Δy such that

$$R(y_o \pm \Delta y) - R(y_o) = \sigma(R), \qquad (3\text{-}22)$$

where $\sigma(R)$ is given by eqn. (A17). Errors reported in the next section are ensemble averages of σ_n, calculated from eqn. (3-22) using noise-free residual functions for 100 granular scenes. Use of one-half Δy as the rms error was justified by Monte Carlo calculations: repeated addition of computer-generated noise to a variety of residual functions showed this to

be the correct one-sigma variation of the apparent stable point.

Noise errors for tracking time-dependent scenes are defined in the same way. To evaluate them, the temporal behaviour of R (y, t) must be known. By expanding the squares in eqn. (3-21) and substituting eqn. (3-3), the following approximate expression is found:

$$R(y, t) \approx \sum_i [2I_i(o, o) + e^{-t/\tau_o} I_i'(y, o)] I_i(o, o) \quad (3\text{-}23)$$

In the vicinity of $y = y_o$, the residual function has a parabolic shape for all trackers and data-sets studied: finite telescope resolution and detector element size always blur the intrinsic cusp-like behaviour expected of random granular scenes. Therefore, this result can be compactly rewritten as

$$R(y, t) \approx R(y_o, t) + 1/2 \; e^{-t/\tau_o} R''(y - y_o)^2. \quad (3\text{-}24)$$

When this is used to evaluate $\sigma_n(t)$ according to eqn. (3-22), it turns out that

$$\sigma_n^2(t) \; \alpha \; e^{t/\tau_o} \; \sigma(R(t)). \quad (3\text{-}25)$$

Finally, eqn. (A17) of Appendix A shows that

$$\sigma_n^2(t) = \sigma_n^2(o) \; e^{t/\tau_o} [1 + 2(SN \; \Delta I_{rms})(1 - e^{-t/\tau_o})] \quad (3\text{-}26)$$

Noise errors increase rapidly in time after each update, similar to the MMT behaviour.

Tracker drift rate is calculated as usual from eqns. (3-7) and (3-8), providing upper and lower limits, respectively.

(b) Fixed-Scene Results

Fixed-scene noise errors were evaluated from eqn. (3-22) for a large grid of CCD trackers using ground, 65 cm, and 125 cm enhanced data. The Standard CCD tracker for illustration is

$$\begin{aligned} SN &= 500, \qquad \Delta I_{rms} = 10\% \\ N_{el} &= 512 \\ d &= 0.167''. \end{aligned} \quad (3\text{-}27)$$

Note that N_{el} is the number of elements in each of the two lines of the detector array. The detector element size d is the angular size of a 0.001 inch element in the focal plane of either a 125 cm F25 aperture or a 65 cm F50 aperture; values appropriate to 125 cm F50 and 65 cm F25 were used in other calculations.

Figure 3-26 gives a brief summary of the fixed-scene noise errors. The Standard CCD tracker has a noise error between 0.0021" and 0.0004". The lower limits from enhanced data seem suspiciously small, even though they were computed in precisely the same way as the upper limits from ground data. In any case, these errors are between 16 and 40 times smaller than those of the MT, and between 4 and 6 times less than the MMT's errors. As shown above by eqn. (3-26), they increase rapidly as the real-time scene deforms.

The detailed plots show noise errors in centi-arcseconds versus SN, N_{el}, and d for the three data-sets. As discussed above, the parabolic behaviour of R(y) causes very precise SN^{-1} dependence of the noise error. Quantization does not change this unless the interval ΔI becomes comparable to I_{av}/SN, which does not happen unless the number of levels is less than about 5 $SN \cdot \Delta I_{rms}$. In Figure 3-28, N_{el} is varied between 20 and 220, a limit set by computer memory: the extrapolation to 512 elements seems safe. Variations of σ_n with d in Figure 3-29 are also expected and unexciting.

(c) Time Dependence of Errors

The theory of feature-following and absolute tracking errors is summarized in eqns. (3-4), (3-7) and (3-8). Feature-following errors are assumed to be caused by noise alone. Growth of the noise error $\sigma_n(t)$ as the scene changes is given by eqn. (3-26). Total length of the Standard CCD tracker is 85.5" in each arm, which was assumed to contain 43 granules.

Figures 3-30 and 3-31 show the absolute errors (upper and lower limits in solid curves) and the feature following errors after 10 and 60 minutes obtained with ground data. Optimum update times are again between 30 and 60 seconds for absolute accuracy and 2 to 4 minutes for minimizing noise errors alone. The worst-case errors are approximately 1 and 3 resolution elements after 10 and 60 minutes for a 125 cm aperture. Although many more curves

RESULTS FOR CCD TRACKER

- NOISE ERRORS: ALL DATA

$$\sigma_N \approx \sigma_o \left[\frac{SN}{500} \cdot \frac{\Delta I_{rms}}{10\%}\right]^{-1.0} \left[\frac{N_{e\ell}}{512}\right]^{-0.3} \left[\frac{d}{0.17"}\right]^{0.4}$$

WHERE

$$\sigma_o = \begin{cases} 0.0021" & \text{GROUND DATA} \\ 0.0007" & \text{65 cm DATA} \\ 0.0004" & \text{125 cm DATA} \end{cases}$$

2-SIGMA ERROR $\approx 1.5\ \sigma_N$

- SYSTEMATIC ERRORS

LEAST-SQUARE FITTING OF A FIXED SCENE MAKES NO SYSTEMATIC ERROR

- THESE VERY LOW NOISE ERRORS ARE OBTAINED ONLY FOR FIXED SCENES; σ_N INCREASES RAPIDLY WITH TIME AS THE SCENE CHANGES

Fig. 3-26

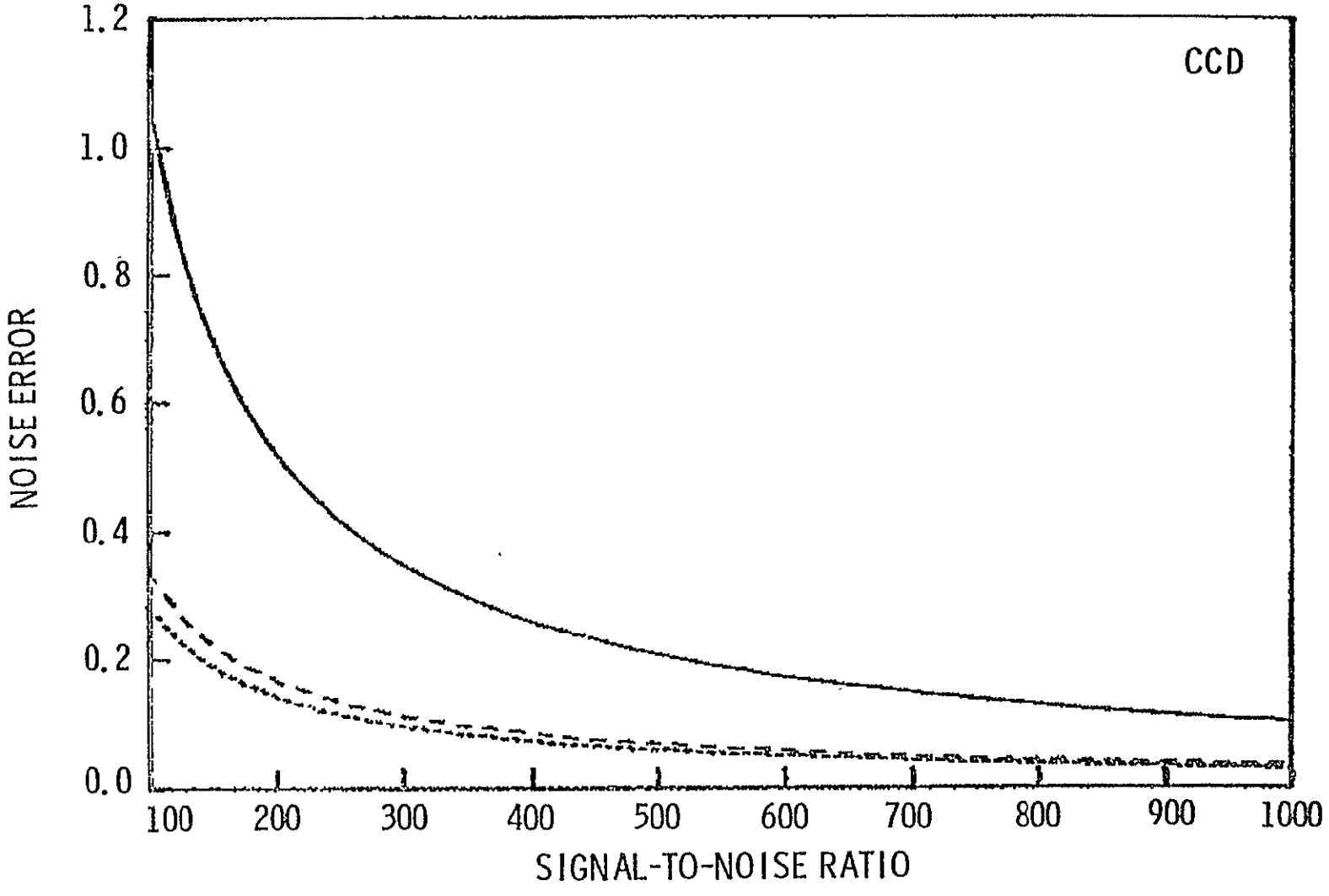

Fig. 3-27 CCD Noise Errors (Centi-Arcseconds). Results for Ground, 65 cm and 125 cm Data

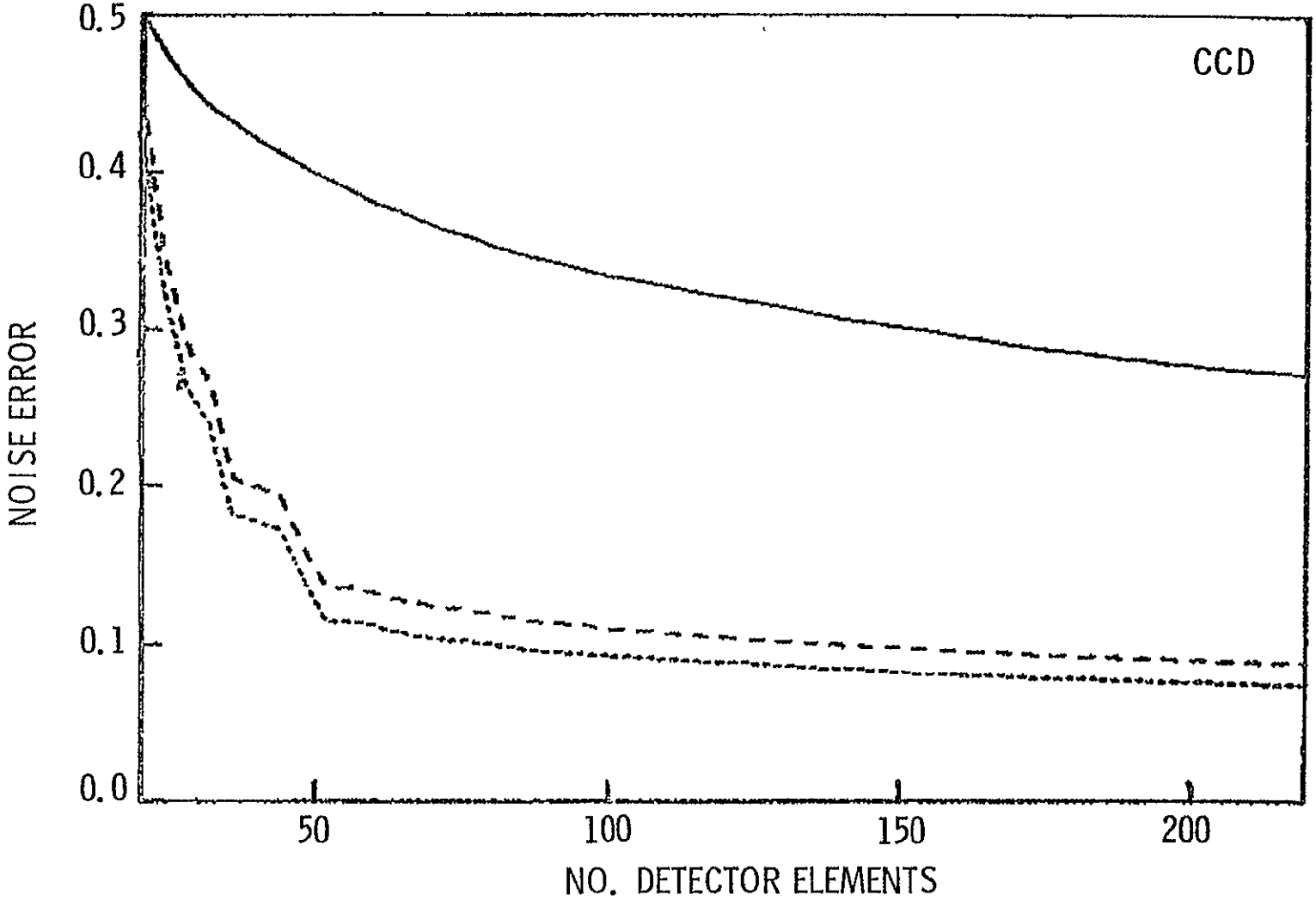

Fig. 3-28 CCD Noise Errors Versus N_{el}

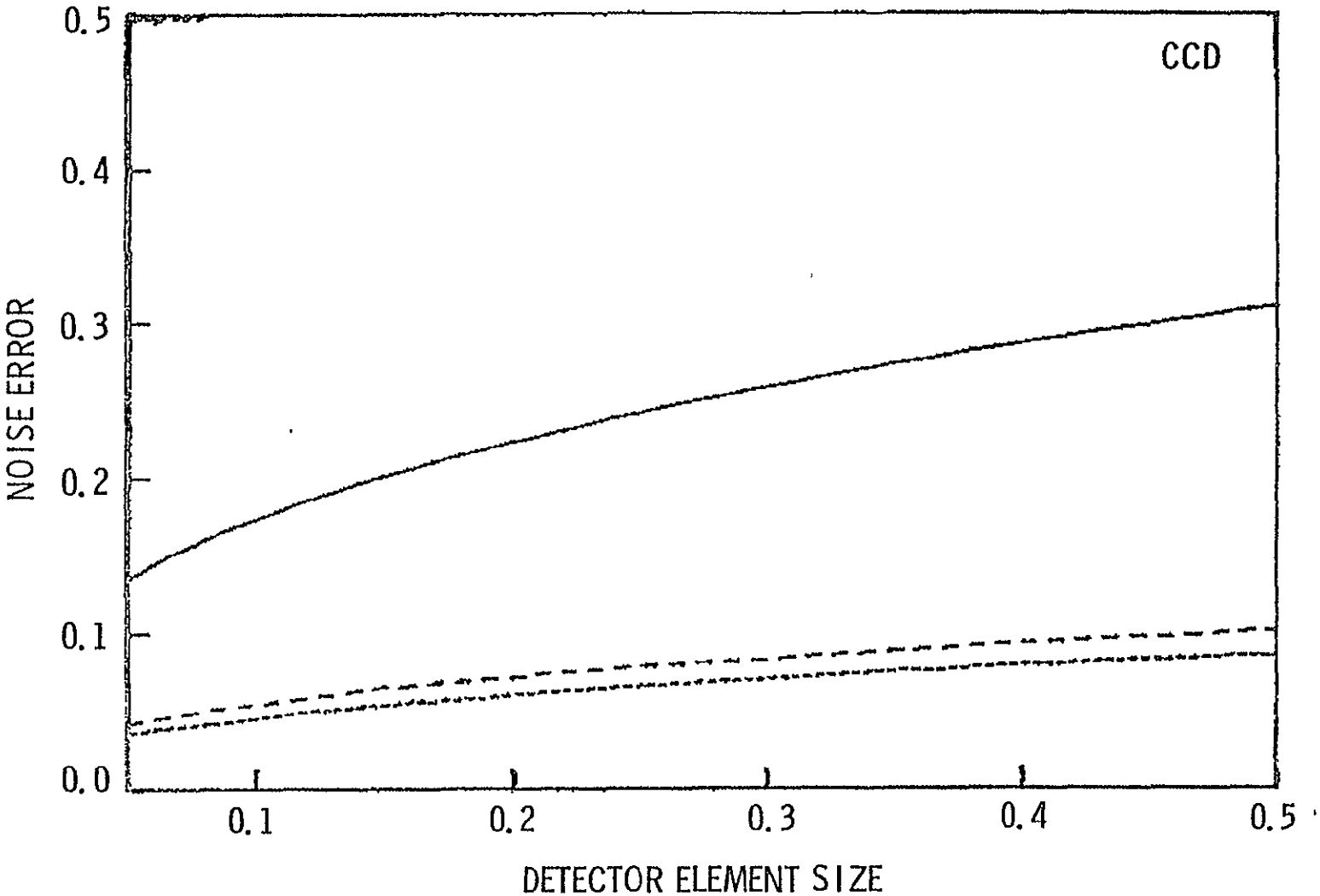

Fig. 3-29 CCD Noise Errors Versus Image Scale

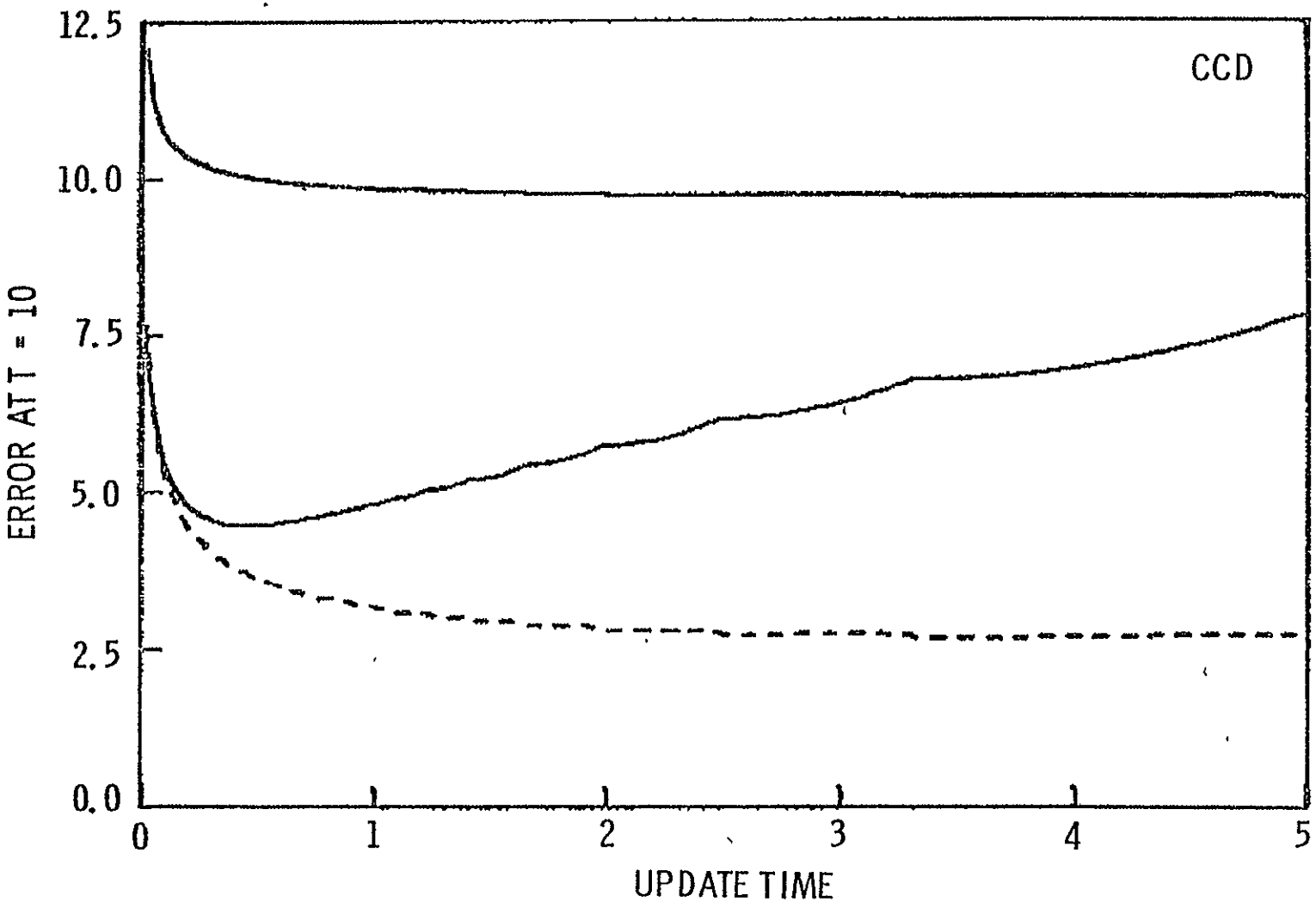

Fig. 3-30 CCD Errors After 10 Minutes (Feature-Following Error and Bounds for Absolute Error)

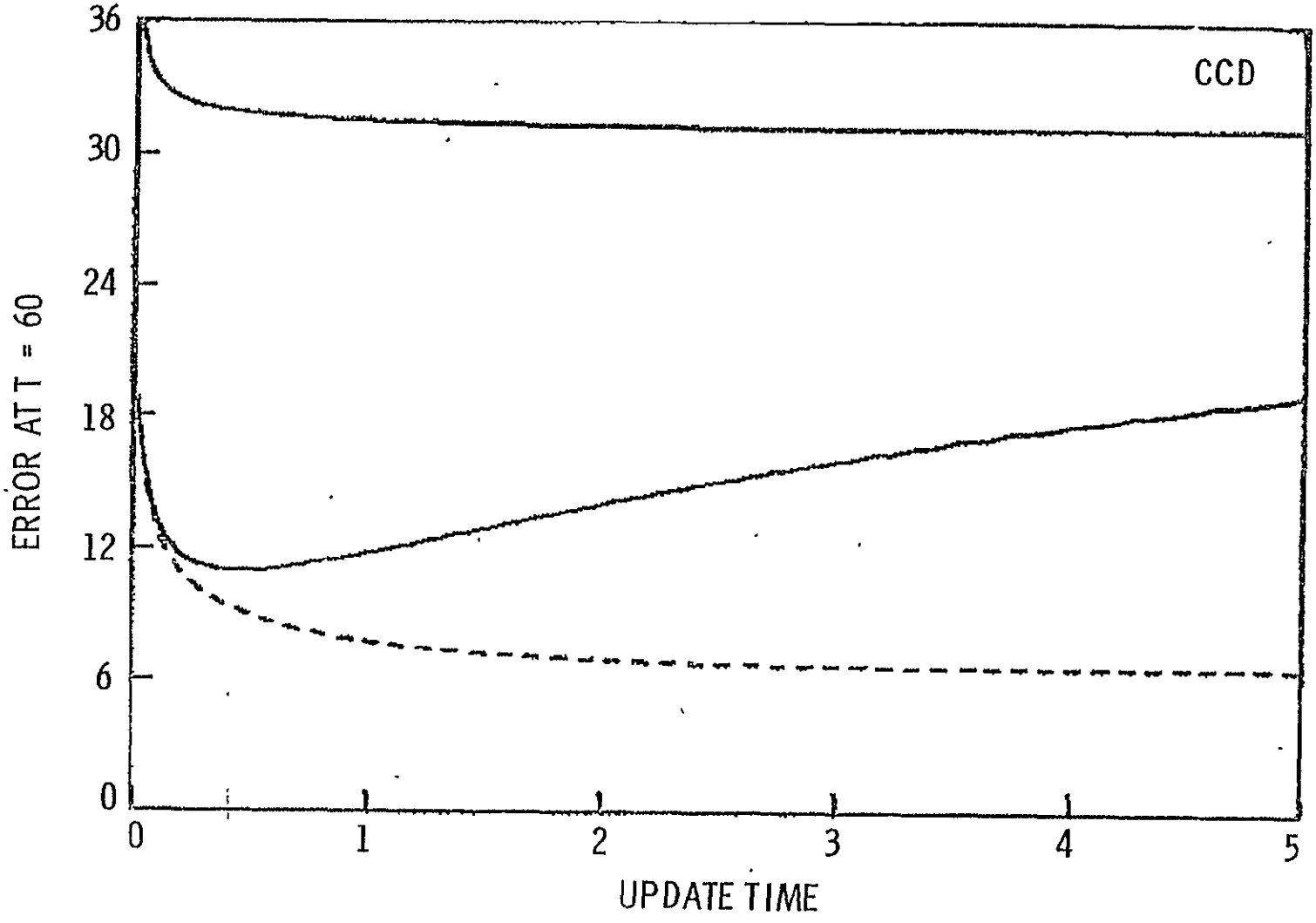

Fig. 3-31 CCD Errors After 60 Minutes

could be generated, as for the MT and MMT, these two plots are sufficient to show the capability of the Standard CCD tracker.

3.7. Worked Example of Tracker Error Analysis

In this section, the errors of a hypothetical CCD tracker are calculated in detail, to illustrate the use of the formulas and plots of the preceding sections. Although the example is completely contrived, none of the numbers chosen is unrealistic.

Problem: A correlation tracker has two crossed lines of 256 detector elements each. The CCD array has elements 0.001 inch square to be used in the focal plane of a 125 cm F50 telescope. The tracker performs a least square fit between its stored and real-time scenes, pointing the telescope to minimize the residuals of the fit. The real-time scene is measured 200 times per second. If the detector elements have a signal-to-noise ratio of 800, how accurately can it track granulation scenes at disk center? Specifically, calculate the rms tracking errors expected one and ten minutes after initial acquisition of the target.

Solution: The first step is to calculate the rms tracking error caused by noise on scenes which are independent of time. Upper and lower limits for this quantity, σ_n, are most easily obtained from the equation in Figure 3-26. Substituting SN = 800, ΔI_{rms} = granulation contrast at disk center = 10%, N_{el} = 256, we obtain

$$\sigma_n = 0.77\ \sigma_o \left(\frac{d}{0.17''} \right)^{0.4}, \quad .0004'' < \sigma_o < .0021''.$$

Here, d is the angle subtended by the length of one detector element in the focal plan:

$$d = \left(\frac{0.001 \text{ inch}}{\text{focal length}} \right) = 0.084 \text{ arcseconds.}$$

This leads to $0.0002'' < \sigma_n < 0.0012''$; the upper limit will be used in the rest of the calculation. Errors in both x and y directions are included in σ_n.

If the tracker were always used to align two identical scenes, then the only tracking error would be $\sigma_n \leq 0.0012''$. However, this result could

be changed by the frequency response of the servo loop of which the tracker is a part as discussed in Section 2.7. As an error sensor, the tracker has a bandwidth of 0-200 Hz with a white noise spectrum. However, since the tracker uses crossed lines instead of a raster pattern, it would lose its lock on the target if image displacements of more than $\sim$ 1" or speeds exceeding 200 arcsec/sec were encountered.

In most applications, the tracker would be attempting to match time-variable scenes. Changes in the noise error in time and the tracker drift rate caused by motion of granules in its FOV must be considered. The noise error $\sigma_n(t)$ is given by eqn. (3-26), where τ_o = 6.27 minutes is the granular correlation time. For t = 1 minute, this equation gives $\sigma_n(1) = 0.0064"$; this is the "feature-following" error E_{FF} discussed in previous sections. The absolute error, including noise and tracker drift, is bounded by the results of eqns. (3-7) and (3-8). Substituting V_o = rms granular speed = 1 km/sec = 0.083 arcsec/min, m= number of granules in FOV = $N_{el} \cdot d/2"$ = 10, and n = number of updates = 0, we find that the tracker will drift by about 0.026" in one minute, on the average. This is much greater than the noise error, and so the total absolute error after one minute is

$$E(1) \approx 0.026" \text{ rms.}$$

To track accurately over ten minutes, the tracker must update its stored picture periodically. For absolute tracking, an update time τ_u = 1 minute is near the optimum value, as shown by Figure 3-30. The accumulation of noise errors is now described by eqn. (3-4), with σ_s = o, n = 10, and Δt = o; this yields

$$E_{FF}^2(10) = 10\,(0.0064)^2 + (0.0012)^2;$$

$$E_{FF}(10) = 0.020".$$

Upper and lower limits to the total error come from substitution into eqns. (3-7) and (3-8):

$$0.085" < E(10) < 0.21".$$

Thus, the tracker will drift by one or two resolution elements in a ten minute interval.

Two final comments are in order. First, τ_u = 1 minute is the average update time. In fact, the tracker should update when its minimum residual rises to a fraction

$$(1 - e^{-\tau_u/\tau_o}) = 0.15$$

of the uncorrelated value, $2 N_{el} \langle I^2 \rangle$. Second, the absolute tracking errors refer to coordinates moving with the average solar rotation at disk center, 0.15 arcseconds/min. If desired, the rotation could be removed independently of correlation tracker operation.

3.8. Summary of Tracker Performance

The three trackers analyzed in detail above are summarized in Figure 3-32. This shows upper and lower limits to the rms tracking errors ten minutes after initial target acquisition. The trackers are used with a 65-125 cm telescope to follow specific features or to track in absolute coordinates with respect to the solar limit.

The present Marshall Tracker shows errors between one and ten telescope resolution elements. It suffers from a small field-of-view and a poor choice of algorithm, aggravated by low sensitivity and three-bit quantization. The modified Marshall Tracker uses the same hardware with a minor (but effective) change in algorithm and with a variable image scale. Its performance is quite good, with errors of at most two resolution elements after ten minutes. Finally, the CCD Tracker corrects all shortcoming of the Marshall Tracker: sensitivity, FOV, algorithm and computing capability are all greatly improved. Taken together, these improvements result in errors one-third to one-half of those for the Modified Marshall Tracker.

TRACKER PERFORMANCE SUMMARY

ERRORS (ARCSEC) AFTER 10 MIN		
TRACKER	FEATURE-FOLLOWING COORDS. UPDATE TIME ≈ 1–2 MIN	ABSOLUTE COORDS. UPDATE TIME ≈ 30 SEC
MARSHALL	$0.07 < \epsilon < 0.10$	$0.20 < \epsilon < 0.70$
MODIFIED MARSHALL WITH VARIABLE IMAGE SIZE	$0.02 < \epsilon < 0.07$	$0.06 < \bar{\epsilon} < 0.20$
STANDARD CCD	$0.007 < \epsilon < 0.03$	$0.02 < \epsilon < 0.10$

Fig. 3-32

4. Focus Quality Information

4.1. Introduction

In principle, the detector array of a correlation tracker can be used to measure the focus quality of its image. Defocus, misalignment or aberrations always decrease the fine structure or high spatial frequency power in the image. Suitable processing of the tracker detector outputs can measure this fine structure content. There are two potential uses for such a system: (1) to assist in finding the position of sharpest focus, during a focussing operation; (2) to act as a constant monitor of image quality, signaling when refocussing is necessary. For either application, a single parameter derived from the tracker scene is needed for use in a control loop. The scene-to-scene variation of any parameter, even when focus is perfect, presents a problem for the second application: the optics must be focussed on each scene, and refocussed periodically as the scene changes, to provide a baseline for sensing image degradation.

In this study, two different indicators of focus quality were evaluated using statistical descriptions of granulation scenes. Detector configurations corresponding to the MT and the CCD tracker were modelled, and the average sensitivity to noise and to defocus of both indicators were computed. These indicators are: (1) the curvature of the correlation function, which can be obtained from the present MT with trivial modifications; (2) the image power in a pre-selected spatial frequency band, which requires real-time calculation of Fourier transformed images. This second indicator is an effective measure of image quality if used with a CCD tracker, but it is not a panacea for the problem of active focus control.

4.2. Mathematical Model

The mathematical formulation used to study focus quality indicators is described in this section. The fundamental theory is first presented as if a continuously sampled image were available, for simplicity. Then the effects of the finite number of detector elements and their spacing are considered. All calculations are one-dimensional, as if detector arrays were straight lines: this is a good approximation as long as the spatial frequencies considered are longer than the inverse curvature of the tracker element pattern.

Given a one-dimensional image I(x), the MT measures an approximation to the correlation function C(y) defined by

$$C(y) \equiv \frac{1}{L} \int_{-L/2}^{L/2} I(x)\ I(x + y)\ dx, \qquad (4\text{-}1)$$

where L is the total length (in arcseconds) of the detector array. The curvature D which can be measured by the MT is

$$D = \left| C(d) + C(-d) - 2\ C(o) \right|, \qquad (4\text{-}2)$$

d being the element size. Defocus always causes the curvature to decrease. If a tracker uses the residual function R(y), it is easy to show that the curvature is the same, on the average.

The second image quality indicator is based on the Fourier transform of I(x):

$$\tilde{I}(k) \equiv \int_{-\infty}^{\infty} e^{2\pi i k x}\ I(x)\ dx; \qquad (4\text{-}3)$$

here, k is the spatial frequency with units cycles/arcsecond. Power in a band, $k_1 < k < k_2$, is defined by

$$P(k_1, k_2) = \int_{k_1}^{k_2} \left| \tilde{I}(k) \right|^2 dk. \qquad (4\text{-}4)$$

By proper choice of k_1 and k_2, power in a band can be a sensitive measure of image quality. The value of the correlation peak curvature can also be expressed in terms of $\tilde{I}(k)$ by means of the relation:

$$D \ \alpha \int_{-\infty}^{\infty} [1 - \cos 2\pi kd] \left| \tilde{I}(k) \right|^2 dk; \qquad (4\text{-}5)$$

the exact proportionality constant will not be needed.

Actual (as opposed to measured) intensities of a granulation scene, $I_o(x)$ or $\tilde{I}_o(k)$, can be described statistically using the power spectrum $S_o(k)$. Specifically,

$$\left\langle \left| \tilde{I}_o(k) \right|^2 \right\rangle \quad \alpha \quad S_o(k). \qquad (4\text{-}6)$$

S_o (k), as measured by Kinahan (Reference 2, Chapter 3), is plotted in Figure 3-4. The intensities measured by a tracker detector array are described by the modified power spectrum S (k), which includes the effects of telescope resolution and detector element size:

$$S(k) = S_o(k) \left| MTF(k) \tilde{T}(k) \right|^2. \qquad (4\text{-}7)$$

MTF (k) is the modulation transfer function of the optical system, including defocus or aberrations, and $\tilde{T}$ (k) is the Fourier transform of the detector element profile.

$$\tilde{T}(k) = \frac{\sin(\pi k d)}{\pi k d} . \qquad (4\text{-}8)$$

All of these functions are even functions of k, and so only positive spatial frequencies need be considered, if desired.

It is convenient to express MTF (k) as a product of two terms, where the first represents the perfect, diffraction limited MTF, and the second simulates loss of resolution caused by defocus. This is not a rigorous procedure, by any means, but an exact treatment would require a much more elaborate specification of the optical system and its aberrations. The following simple model is certainly adequate for a one-dimensional calculation:

$$MTF(k, \sigma) = MTF_o(k) \cdot A(k, \sigma), \qquad (4\text{-}9)$$

where

$$MTF_o(k) = 1 - |k|/k_{max}; \qquad (4\text{-}10)$$

$$A(k, \sigma) = \exp\left[-\pi (\sigma k / k_{max})^2\right]. \qquad (4\text{-}11)$$

The largest detectable spatial frequency is

$$k_{max} = (4.85 \text{ cy/ }") \text{ (telecsope diamter/50 cm)}. \qquad (4\text{-}12)$$

Defocus is measured by the dimensionless parameter σ, which is defined by eqn. (4-11): this definition was chosen so that the effective resolution is given by

$$\left(\begin{array}{c}\text{Effective}\\ \text{Resolution}\end{array}\right) \approx \sqrt{1+\sigma^2} \quad \left(\begin{array}{c}\text{Diffraction}\\ \text{Limit}\end{array}\right). \tag{4-13}$$

Equations (4-7) through (4-13) permit the calculation of $<|\tilde{I}(k)|^2>$ for any values of the aperture size, defocus parameter σ, and detector element size d. The focus quality indicators can then be obtained from eqns. (4-4) and (4-5). Finite sampling effects are easily taken into account. If the tracker has N_{el} elements spaced at intervals of Δx, then $\tilde{I}(k)$ can only be measured at the discrete frequencies k_j, where

$$k_j = \frac{\cdots j}{N_{el}\,\Delta x}, \quad j = -\frac{N_{el}}{2}, \cdots \frac{N_{el}}{2}. \tag{4-14}$$

Each Fourier component $\tilde{I}(k_j)$ is an average over an interval $\Delta k = 1/N_{el}\,\Delta x$.

Finally, the sensitivity to detector noise of measured values of D and $P(k_1, k_2)$ must be calculated. Let n_j be the noise in the output of the j^{th} detector element. Since the various n_j are independent, the noise power spectrum has a constant value, P_n, over the allowed frequency band defined by the k_j. Using the fact that

$$<n_j^2> \quad \alpha \quad \sum_j \Delta k\, P_N(k_j), \tag{4-15}$$

one can derive expressions for P_N in terms of $S_o(k)$, maintaining consistent units. The results are

$$P_N = \frac{\sum_j S_o(k_j)}{N_{el}(SN\,\Delta I_{rms})^2} \tag{4-16}$$

for non-quantized data, and

$$P_N = \frac{0.44 \sum_j S_o(k_j)}{N_{el}\,(SN\,\Delta I_{rms})} \tag{4-17}$$

for three-bit quantized data. SN is the detector signal-to-noise ratio before quantization, and ΔI_{rms} is defined in eqn. (3-2). One P_N is known, the standard deviation of $|\tilde{I}(k_j)|^2$ is given by

$$\frac{\sigma(|\tilde{I}|^2)}{|\tilde{I}^2|} = \frac{P_N}{S(k_j)}\left[2 + 4\frac{S(k_j)}{P_N}\right]^{1/2}. \tag{4-18}$$

Noise sensitivities of D and P (k_1, k_2) are easily computed from this formula.

4.3. Results

Correlation peak curvature D and power in a selected bandwidth P (k_1, k_2) were calculated for two aperture sizes and two detector arrays. These results are most clearly summarized by a set of plots, showing the image quality indicator vs. effective resolution. The behaviour of each indicator in the vicinity of perfect focus is desired, and so curves are normalized to their diffraction limited values. Solid curves show expectation values, and dashed curves are ± one-sigma variations to show the effects of detector noise.

Figure 4-1 shows D (defined by eqn. 4-2) for the Standard Marshall Tracker of Section 3.4 used with a 50 cm aperature. The decreasing curvature with increased blurring is evident, but noise renders this useless as a focus indicator. A Standard CCD array (Section 3.6), as plotted in Figure 4-2, measures D accurately, but a sharper peak at perfect focus would be desirable. Although simple to compute and attractive in principle, D does not appear to be useful in practice.

Power in the 1-2 cycle/arcsecond band is shown in Figures 4-3 and 4-4 for the two trackers. This bandwidth was chosen to show the best possible behaviour of the Marshall Tracker as a focus quality sensor. Extending the band to higher frequencies admits too much noise, whereas a lower frequency band is less sensitive to focus changes. The figure shows that noise errors are comparable to a 50% loss of resolution: without a sizable increase in SN, the Marshall Tracker is a poor instrument for measuring image quality.

On the other hand, a CCD tracker has the sensitivity and the spatial resolution to make use of even higher spatial frequency components, if desired. Figures 4-4 through 4-6 demonstrate the potential for very accurate location of sharpest focus by adding Fourier transform capability to a CCD correlation tracker. The curve in the last figure is less steep than the others because detector sizes are nearly unchanged while diffraction limited resolution has increased by a factor of 2.5. Even so, the tracker can still sense resolution losses of 5% or less.

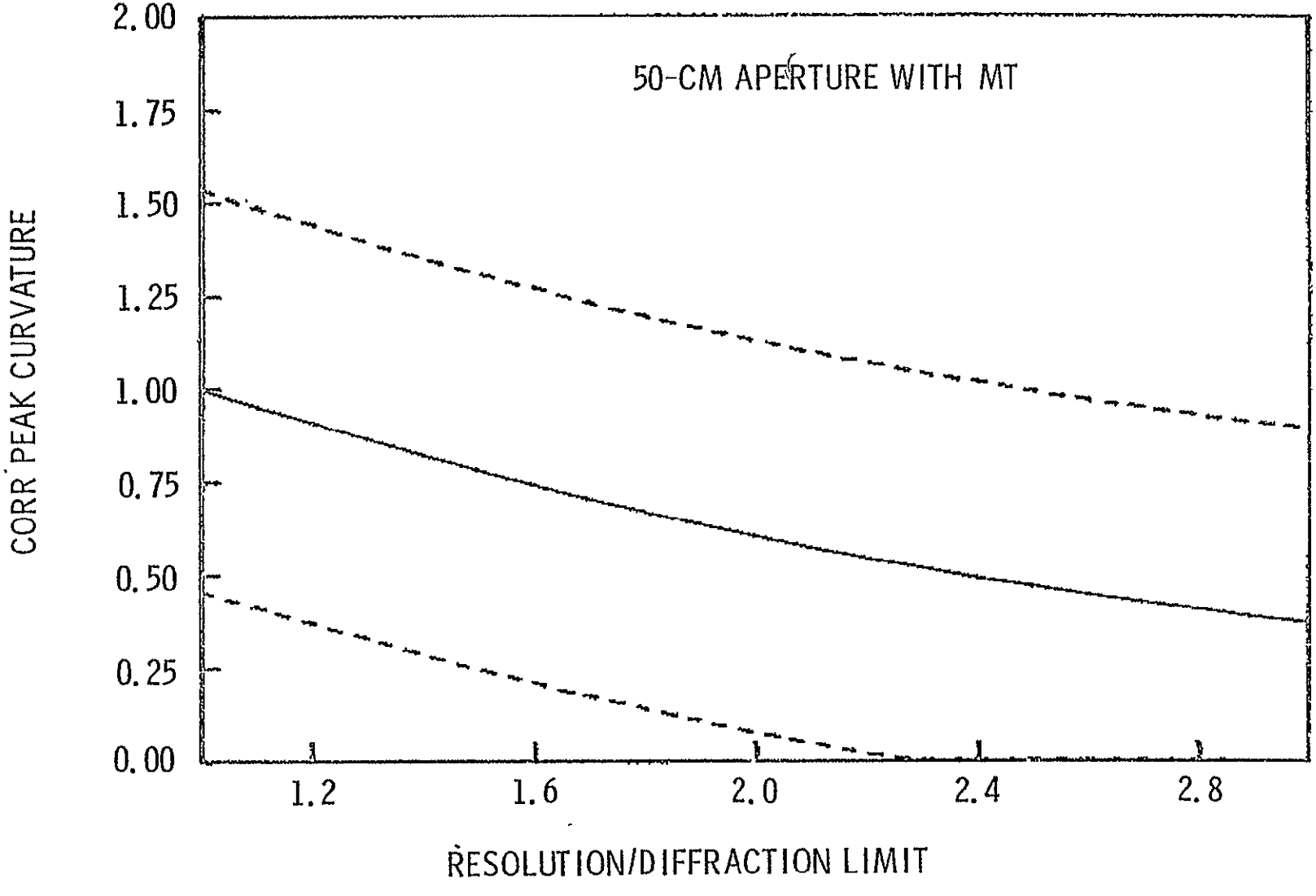

Fig. 4-1 MT Correlation Peak Curvature Versus Defocus

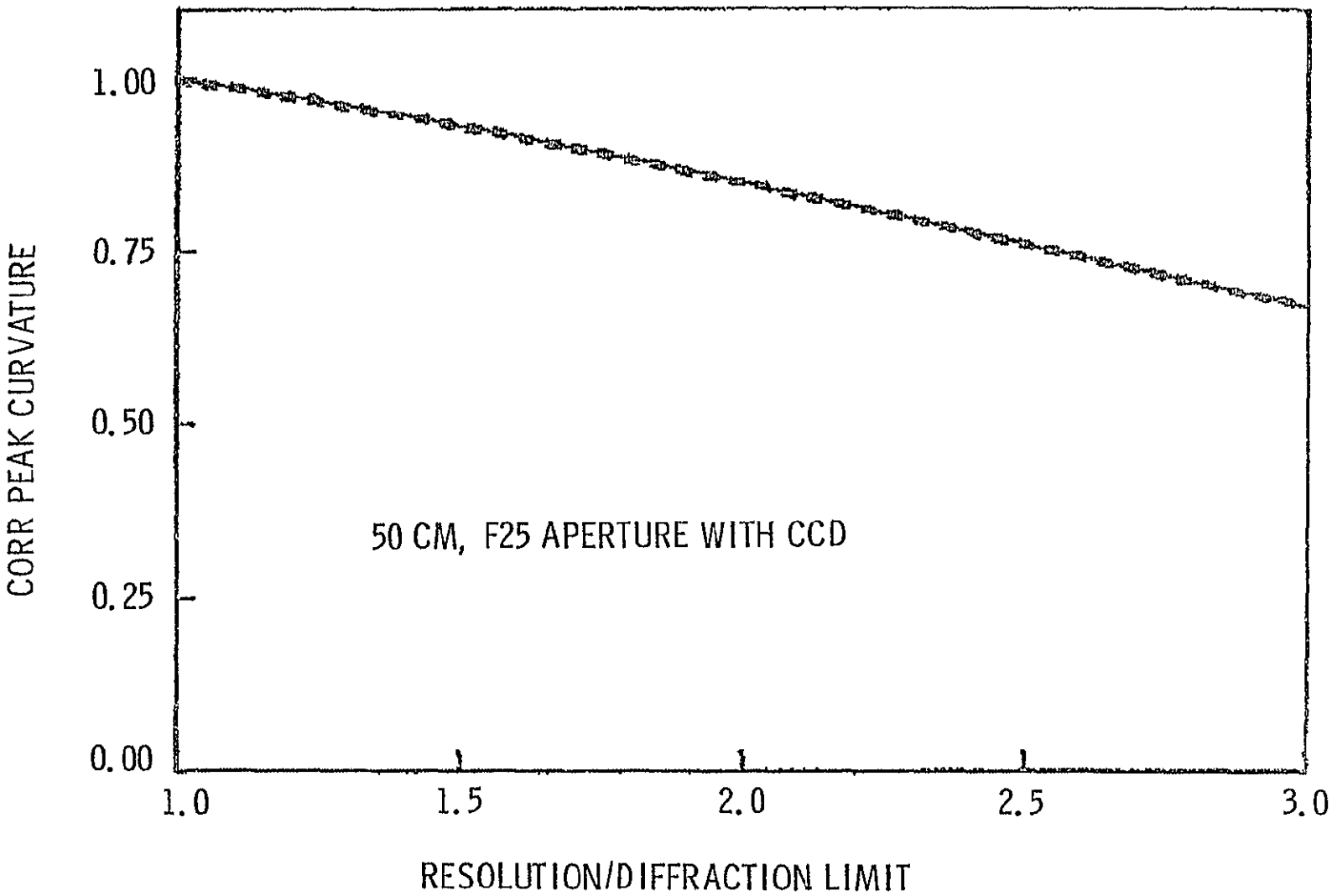

Fig. 4-2 CCD Correlation Peak Curvature

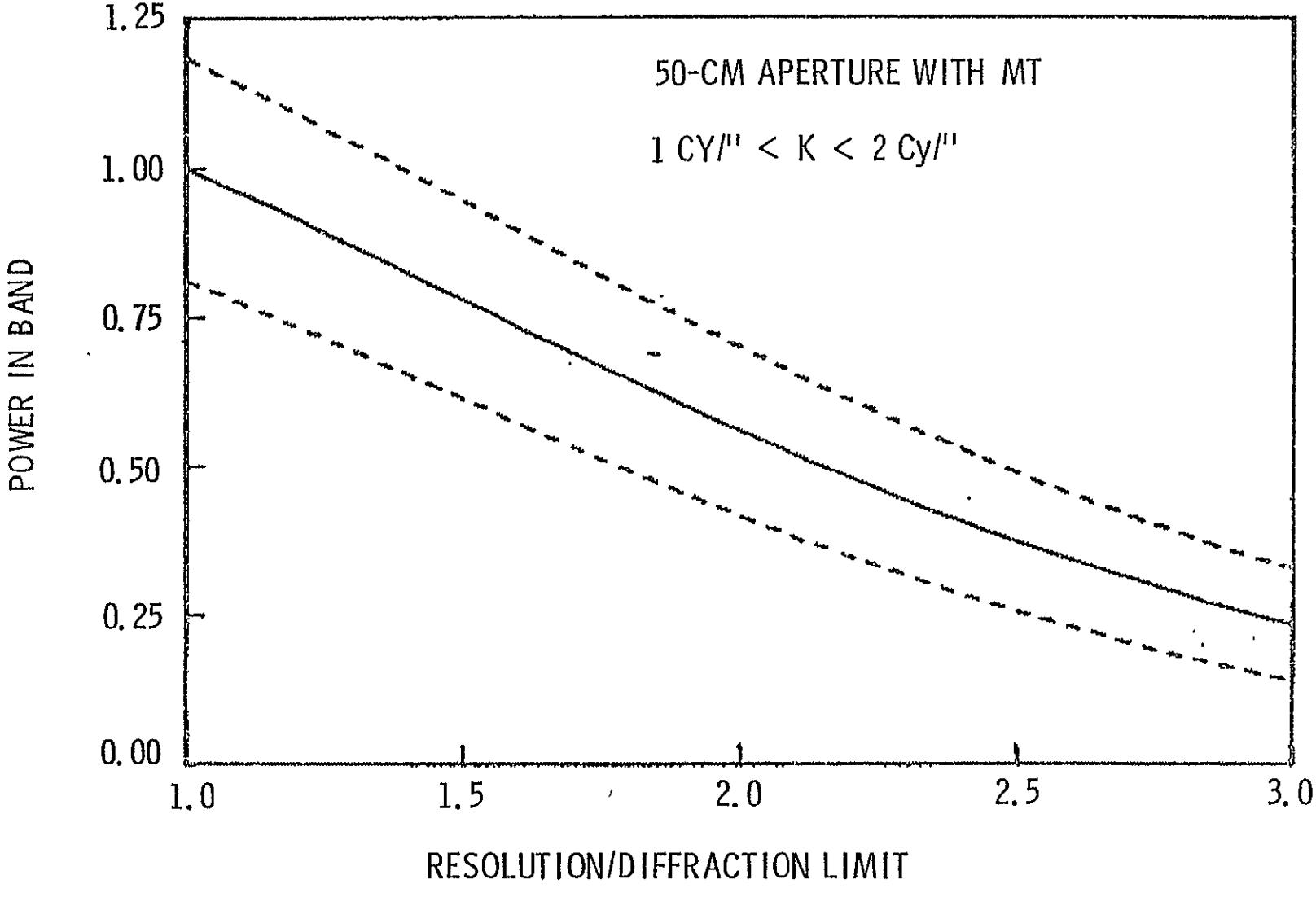

Fig. 4-3 MT Power in Band

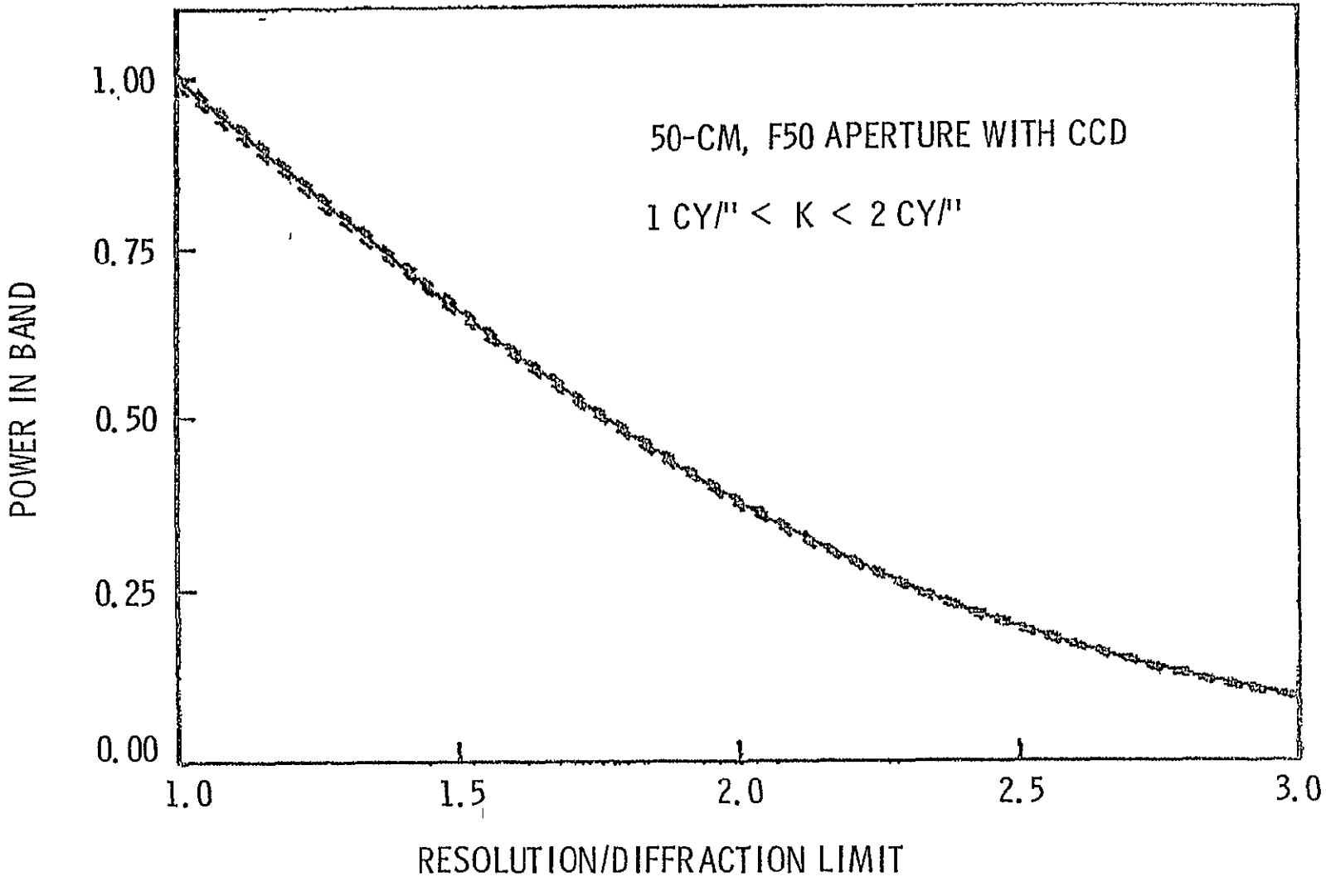

Fig. 4-4 CCD Power in Band

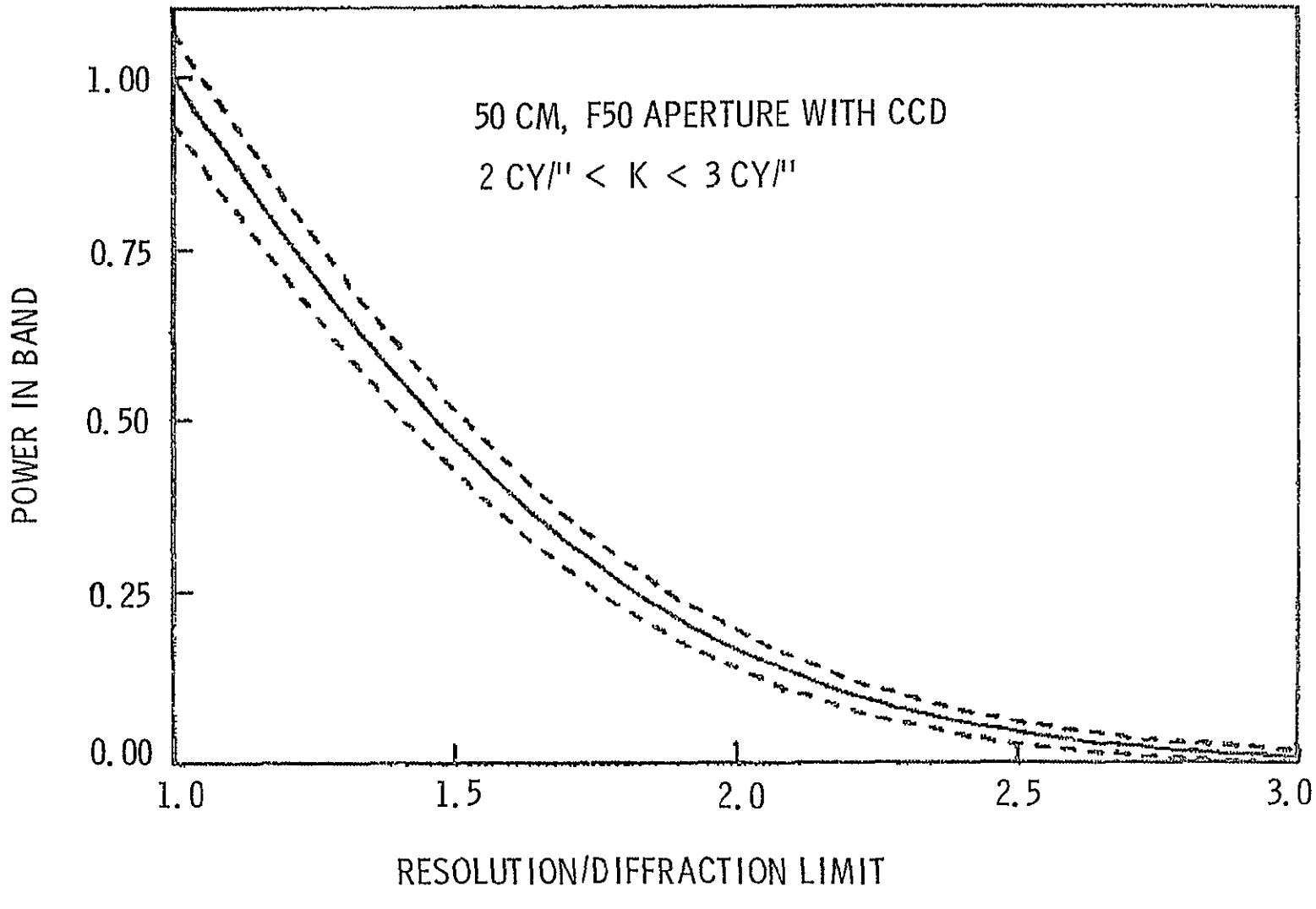

Fig. 4-5 CCD Power in Band: Higher Frequencies

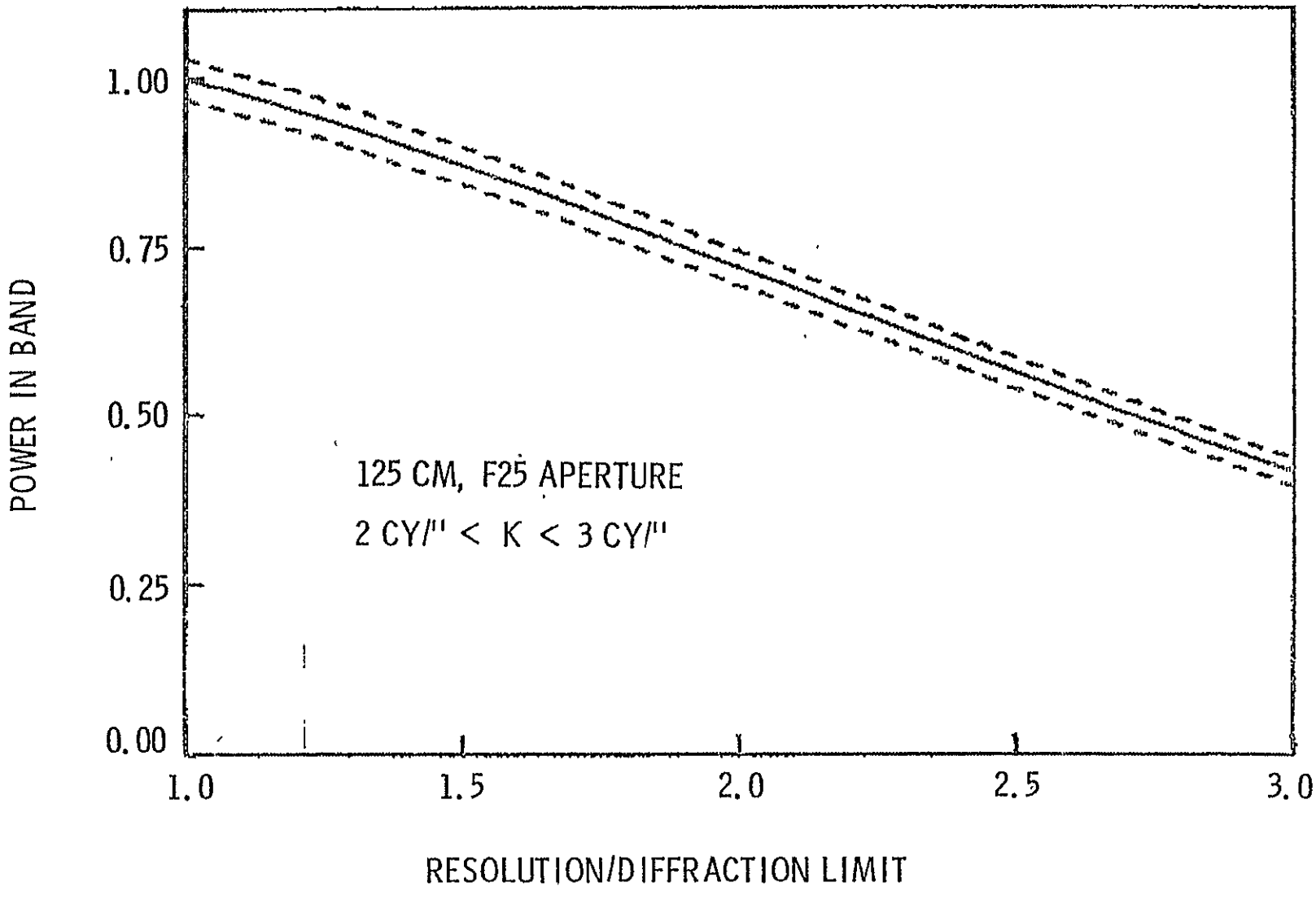

Fig. 4-6 CCD Power in Band: Larger Aperture

5. Conclusions and Recommendations

This study has characterized correlation trackers in three distinct ways. Chapter 2 gives an extensive, qualitative discussion of the utility, design principles, key parameters, and error sources of correlation trackers as applied to pseudo-random images in general and the solar granulation in particular. Three specific tracker concepts are analyzed quatitatively in Chapter 3, using observational data on the solar granulation to calculate expected tracking errors in various potential applications. Finally, chapter 4 sketches the ability of a correlation tracker to perform a second independent task, the direct measurement of image quality at the focal plane.

In general, a correlation tracker is appropriate for image motion compensation when the images are random, only their statistical properties being known in advance. The solar granulation is a random, low contrast image with typical correlation lengths and times of one arc second (725 km on the sun) and six minutes, respectively. Its temporal statistics are not well known, and so analyses of the time-dependence of tracker errors are necessarily tentative. Nevertheless, a well-designed correlation tracker can perform acceptable image motion compensation on a meter-class solar telescope in three possible configurations:

- Use within the loop of a limb guider; the tracker stores images whenever the guider error signal is small and performs active tracking only for the short time intervals when the guider error signal exceeds a threshold.
- Alignment of identical images fed to two different instruments;
- Tracking in absolute coordinates with respect to the limb; although a CCD tracker can have errors comparable to telescope resolution for tens of minutes, it should not be used as the only pointing system. It cannot acquire a target initially, reacquire after a displacements greater than one arcsecond, or remove the effect of solar rotation.

Three sources of correlation tracking error have been identified and studied. Errors caused by detector noise can be minimized by proper choice of the tracker algorithm, number of quantization levels, detector sensitivity, and number of detector elements. Systematic errors are image displacements which occur when aligning two identical, noise-free scenes;

they can be eliminated by choosing a proper algorithm or minimized by increasing the number of elements. Tracker drift, caused by the motion of granules in the FOV, can only be minimized by increasing the FOV and choosing a proper scan pattern.

The numerical simulations of chapter 3 are summarized in Figures 3-5, 3-17, and 3-26 for tracking fixed, time-independent scenes; the growth in time of tracker errors is summarized in Figure 3-32. The present Marshall Tracker (MT) does fairly well on fixed-scenes but drifts very rapidly because it only sees one granule in its FOV. If the MT is modified to use the least-squares residual algorithm, its fixed scene performance improves significantly. Additional inclusion of a variable image scale can easily cut the drift rate by a factor of three. Finally, the standard CCD tracker shows very small errors for all applications listed above.

Chapter 4 shows that a correlation tracker can be used to measure the focus quality of the image, if Fourier transform capability is added and if the tracker scan pattern includes a uniformly sampled linear array. The Marshall Tracker is of doubtful utility for this purpose because of its low detector sensitivity and three-bit quantization. A CCD tracker can measure focus quality very accurately, as shown in Figures 4-4 through 4-6. However, the following reservations must be noted:

- the tracker cannot tell which degree-of-freedom of the optical system is causing the defocus;
- the tracker cannot always distinguish between image scale changes and defocus;
- the tracker's image quality indicator is scene-dependent, and so frequent updating may be needed during refocussing; the interaction of refocussing and simultaneous tracking deserves more study.

There are several areas of investigation which merit further study. First, since CCD trackers exhibit the greatest promise in all performance areas except scan pattern versatility and low light level tracking, a detailed design of a CCD tracker should be undertaken, and a tracker constructed. Such a tracker should also be designed to serve as a focus monitor.

Second, since the detailed characteristics of the time varying granulation patterns are at present unknown, this study has left rather wide error bars in the errors expected as a function of time. Results recently obtained by Dr. P. Mehltretter could be used to vastly improve these results, and could be incorporated in a follow-on study.

It is perhaps worth pointing out that an engineering design of a correlation tracker specifically for use with the SOT would be useful for producing heat source, weight, and size numbers for SOT engineering definition studies, even if a tracker is not actually constructed. Also the characteristics of the tracker as a servo component would be better defined.

A study is also needed on interactions between the limb tracker and correlation tracker, although this will probably have to wait until the telescope structure is better defined. A part of this problem which could be immediately attacked is the question of techniques for compensating for solar rotation.

We recommend that development of image dissector trackers proceed. We do not believe, however, that the specific configuration of the Marshall tracker studied represents an immediately useful configuration for SOT.

Appendix A. Tracker Noise Errors

1. Introduction

This Appendix gives brief derivations of the formulas used in Chapter 3 for the noise sensitivity of the three tracker algorithms. The important quantities are the variances due to noise of the correlation function C(y) and the residual function R(y), with either quantized or unquantized intensities. Detector noise level is assumed to be constant, with standard deviation I_{av}/SN; although shot noise may be dominant for some detectors, it is negligibly different for a low contrast target like the solar granulation. Throughout this Appendix, all averages are taken over the possible values of the noise, and <u>not</u> over an ensemble of scenes I_i.

2. Noisy Correlation Functions

The detector outputs are two sets of intensities with noise, $I_i + n_i$ and $I_i' + n'_i$; these are quantized to eight levels after I_{av} subtraction. The variance $\sigma^2(C)$ is needed, where

$$C = \sum_i (I_i + n_i)(I_i' + n_i') \tag{A1}$$

and

$$\sigma^2(C) = \langle C^2 \rangle - \langle C \rangle^2. \tag{A2}$$

The noises n_i and n_i' are independent and have zero mean, and so

$$\langle C \rangle = \sum_i I_i I_i'. \tag{A3}$$

After some algebra, one obtains

$$\langle C^2 \rangle = \sum_{i,j} I_i I_j I_i' I_j' \tag{A4}$$

$$+ \langle \sum_i n_i^2 I_i'^2 + n_i'^2 I_i^2 + n_i^2 n_i'^2 \rangle.$$

PRECEDING PAGE BLANK NOT FILMED

When the intensities are quantized into intervals ΔI much larger than the detector noise I_{av}/SN, a good approximation is

$$< n_i^2 > = p\,\Delta I^2 = \left(\frac{\beta\, I_{av}}{SN\,\Delta I} \right) \Delta I^2. \qquad (A5)$$

p is the probability that the measurement I_i was mis-quantized because of the noise n_i, and β is a numerical constant of order unity. Assuming the intensities are uniformly distributed across each quantization interval, a simple calculation using the properties of the normal error function yields the value 0.698 for β.

Assembling all of these equations, the variance becomes

$$\sigma^2 (C) = p\,\Delta I^2 \sum_i (I_i^2 + I_i'^2 + p\,\Delta I^2), \qquad (A6)$$

which is essentially the same as eqn. (3-13). The degree of correlation between I_i and I_i' is clearly irrelevant, and so this result is not limited to fixed scenes. When the scenes decorrelate in time, the change in $\sigma_n(t)$ is caused by the exponential decrease in correlation peak slope, and so

$$\sigma_n(t) = \sigma_n (o)\ e^{t/\tau o}. \qquad (A7)$$

3. Noisy Residual Functions

Using the same notation as above, the residual function R is given by

$$R \equiv \sum_i (I_i + n_i - I_i' - n_i')^2. \qquad (A8)$$

Again, n_i and n_i' are assumed to be independent with zero mean. I_i and I_i' may be identical (in the CCD algorithm with fixed scenes), or they may be only partly correlated. In general, let ρ be defined by the relation

$$\sum_i (I_i - I_i')^2 = 2\rho \sum_i I_i^2. \qquad (A9)$$

Then the general expression for the variance of R can be found by tedious algebra:

$$\sigma^2 (R) = \sum_i 8\rho\, I_i^2 < (n_i - n_i')^2 > + < (n_i - n_i')^4 > - < (n_i - n_i')^2 >^2. \tag{A10}$$

In the MMT algorithm, all intensities are quantized; therefore, the noise averages are evaluated using eqn. (A5) and

$$< n_i^4 > = p\, \Delta I^4. \tag{A11}$$

These lead to the result

$$\sigma^2 (R) = 2\, N_{el}\, p\, \Delta I^4 + 2\, p\, \Delta I^4 + 16\, \rho\, p\, \Delta I^2 \sum_i I_i^2. \tag{A12}$$

When the MMT operates on fixed scenes, $\rho \sim 0.02$, and the first term of eqn. (A12) is dominant. The second term is always negligible, but the third grows rapidly because, from eqn. (3-3),

$$\rho \approx 1 - e^{-t/\tau_o}. \tag{A13}$$

Using the rule-of-thumb that the rms fluctuation is approximately one-fifth of the peak-to-peak, it follows that

$$\sum_i I_i^2 \cong \left(\frac{8}{5} \right)^2 N_{el}\, \Delta I^2. \tag{A14}$$

Assembling eqns. (A12) - (A14), the final result is

$$\sigma^2 (R) = 2\, N_{el}\, p\, \Delta I^4 [\, 1 + 20.5\, (1 - e^{-t/\tau_o}) \,]. \tag{A15}$$

This accounts for eqns. (3-19) and (3-20).

Quantization effects are ignored for the CCD tracker, and normal distributions are assumed for the noise. In this case,

$$< n_i^4 > = 3 < n_i^2 >^2 = 3 \left(\frac{I_{av}}{SN} \right)^4. \tag{A16}$$

Combining this with eqns. (A10) and (A13), the variance can be written as

C-2

$$\sigma^2 (R) = 8 \left(\frac{I_{av}}{SN} \right)^2 \left[N_{el} \left(\frac{I_{av}}{SN} \right)^2 + 2 \left(1 - e^{-t/\tau_o} \right) \sum_i I_i^2 \right], \qquad \text{(A17)}$$

which justifies the treatment of Section 3.6 (a).

References

Chapter 2:

1. I.T.T. Electro-optical Products Division Technical Note 112.

2. I.T.T. Electro-optical Products Division Applications Note E12.

3. I.T.T. Electro-optical Products Division F4012/F4012 RP data sheet.

4. Bendix Corporation Aerospace Systems Division RASD-M06441 Final Summary Report for Breadboard Model Solar Correlation Tracker and Simulator, Contract NAS8-29037, 28 January 1973.

5. C. W. Allen, Astrophysical Quantities, 3rd edition, Athlone Press 1973.

Chapter 3:

1. Bahng, J. D. R., and M. Schwarzschild, Astrophys. J. 134, 312 (1961).

2. Kinahan, B. F., Astrophys. J. 209, 282 (1976).

3. Deubner, F. L., and W. Mattig, Astron. & Astrophys. 45, 167 (1975).

4. Karpinsky, V. N., and L. M. Pravdjuk, Sol. Dan. 10, 79 (1972).

5. Gibson, E. G., The Quiet Sun, NASA SP-303, U.S. Gov't Printing Office, 1973.

6. Reference 4, Chapter 2.